# AD-A235 599

WRDC-TR-90-4137

CARBON FIBER MORPHOLOGY, II: EXPANDED
WIDE-ANGLE X-RAY DIFFRACTION STUDIES
OF CARBON FIBERS

Dr. David P. Anderson

University of Dayton Research Institute
300 College Park Avenue
Dayton, OH 45469-0168

FEBRUARY 1991

Interim Report for Period December 1988 - April 1990

DTIC
S ELECTE D
MAY 23 1991
B

Approved for public release; distribution unlimited.

MATERIALS LABORATORY
WRIGHT LABORATORY
AIR FORCE SYSTEMS COMMAND
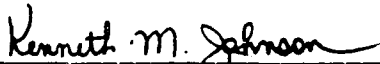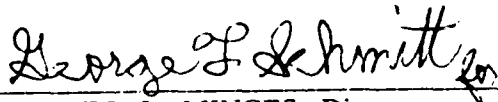WRIGHT-PATTERSON AIR FORCE BASE, OH 45433-6533

91-00245

91 5 22 089

# NOTICE

KENNETH M. JOHNSON, Mat'ls Engineer
Composites Group
Structural Materials Branch

CHARLES E. BROWNING, Chief
Structural Materials Branch
Nonmetallic Materials Division

FOR THE COMMANDER

MERRILL L. MINGES, Director
Nonmetallic Materials Division
Materials Laboratory

# REPORT DOCUMENTATION PAGE

Public reporting burden for this collection of information is estimated to average 1 hour per response, including the time for reviewing instructions, searching existing data sources, gathering and maintaining the data needed, and completing and reviewing the collection of information. Send comments regarding this burden estimate or any other aspect of this collection of information, including suggestions for reducing this burden, to Washington Headquarters Services, Directorate for Information Operations and Reports, 1215 Jefferson Davis Highway, Suite 1204, Arlington, VA 22202-4302, and to the Office of Management and Budget, Paperwork Reduction Project (0704-0188), Washington, DC 20503

| 1. AGENCY USE ONLY (Leave blank) | 2. REPORT DATE | 3. REPORT TYPE AND DATES COVERED |
|---|---|---|
| | February 1991 | Interim Report- December 88-April 90 |

| 4. TITLE AND SUBTITLE | 5. FUNDING NUMBERS |
|---|---|
| CARBON FIBER MORPHOLOGY, II: EXPANDED WIDE-ANGLE X-RAY DIFFRACTION STUDIES OF CARBON FIBERS | F33615-87-C-5239 Program Element 62102F Project No. 2419 Task No. 02 Work Unit Accession #25 |
| 6. AUTHOR(S) Dr. David P. Anderson | |

| 7. PERFORMING ORGANIZATION NAME(S) AND ADDRESS(ES) | 8. PERFORMING ORGANIZATION REPORT NUMBER |
|---|---|
| University of Dayton Research Institute 300 College Park Avenue Dayton, OH 45469-0168 | |

| 9. SPONSORING/MONITORING AGENCY NAME(S) AND ADDRESS(ES) | 10. SPONSORING/MONITORING AGENCY REPORT NUMBER |
|---|---|
| Materials Laboratory (WL/MLBC) (Kenneth Johnson,255-9073) Wright Research and Development Center Air Force Systems Command Wright-Patterson AFB, OH 45433-6533 | WRDC-TR-90-4137 |

**11. SUPPLEMENTARY NOTES**

| 12a. DISTRIBUTION/AVAILABILITY STATEMENT | 12b. DISTRIBUTION CODE |
|---|---|
| Approved for public release; distribution unlimited. | |

**13. ABSTRACT (Maximum 200 words)**

This report, the second in a series, describes the wide-angle x-ray diffraction studies and results on carbon and graphite fibers. Commercial PAN- and pitch-based carbon fibers spanning the generally available modulus range were examined. Crystal perfection, size, orientation, and degree of graphitization and calculated void content are correlated with tensile modulus, tensile strength, and compression strength. These same parameters are examined as a function of heat treatment of several fibers as well.

| 14. SUBJECT TERMS | | | 15. NUMBER OF PAGES |
|---|---|---|---|
| carbon fiber | graphite fiber | x-ray diffraction | 115 |
| crystals | graphitization | | **16. PRICE CODE** |
| crystallite size | orientation | | |

| 17. SECURITY CLASSIFICATION OF REPORT | 18. SECURITY CLASSIFICATION OF THIS PAGE | 19. SECURITY CLASSIFICATION OF ABSTRACT | 20. LIMITATION OF ABSTRACT |
|---|---|---|---|
| Unclassified | Unclassified | Unclassified | UL |

# FOREWORD

This Interim Technical Report was prepared by the University of Dayton Research Institute under Air Force Contract No. F33615-87-C-5239. It was administered under the direction of the Materials Laboratory, Wright Research and Development Center, Air Force Systems Command, Wright-Patterson Air Force Base, OH, with Mr. Kenneth Johnson (WL/MLBC) as Project Engineer.

The use of commercial names of materials in this report is included for completeness and ease of scientific comparison only. It in no way constitutes an endorsement of these materials or manufacturers.

This report covers work conducted from December 1988 through April 1990.

# ACKNOWLEDGEMENTS

# TABLE OF CONTENTS

# LIST OF ILLUSTRATIONS

# LIST OF ILLUSTRATIONS (Continued)

LIST OF ILLUSTRATIONS (Concluded)

# LIST OF TABLES

# 1. INTRODUCTION

This report is intended to update members of the Air Force composites community of the wide-angle x-ray diffraction work being conducted on carbon fibers. Since the issuance of the first technical report on this work [1], several additional means of analyzing the data have been uncovered which are applied to the fiber results as well as data collected on several more fiber samples. Questions of nomenclature and general fiber morphology are addressed in the first report; only the relevant procedures and analyses are presented in this report.

To date only partial reporting of these results has been done in the open literature [2-4]. Additional reports will be issued when the x-ray diffraction and compression strength becomes available.

The commercially-available carbon fibers examined in this study and reported on here are listed in Table 1. Also listed are the available fiber mechanical properties (this is an updated version of Table 1 of reference 1). The mechanical data include some compression strength values; these values were calculated from compression strengths of unidirectional composites since other types of tests give significantly different values for fiber compressive strengths for the same fibers (see for example [5]). It is also known that the compressive strengths of composites made with low or intermediate modulus carbon fibers are not limited by the inherent fiber compression strengths [3,6-8].

In addition several fibers were heat treated, some commercially available and some experimental vapor grown carbon fibers (VGCF, also called CVD for chemically vapor deposited) from Applied Sciences Inc. of Yellow Springs, OH.

Attempts to correlate the mechanical properties listed in Table 1 were generally unsuccessful. A plotting of tensile strength (TS) versus tensile modulus (TM) produced the scattergram in Figure 1. One correlation visible is that the pitch-based fibers tend to have lower tensile strengths than the PAN-based fibers. Also for pitch-based fibers and within one production series, the TS increases with increased TM (Figure 2). A reverse trend of lower TS at higher TM can be seen in two series of PAN-based fibers (Figure 3) with the Toray fibers (M40J and M60J) along with the Celion Apollo fibers (G40-700 and G45-700) and Hercules (IM6 and IM8) forming the higher TS curve and the others (except the PRChina T-2 fiber) forming the lower curve. This last correlation is somewhat suspect since there were too

1

# TABLE 1

## CARBON FIBER MECHANICAL PROPERTIES [1,3,5,6,7,9-13]

| Fiber | Manufacturer | Tensile Modulus (GPa) | (Msi) | Tensile Strength (GPa) | (ksi) | Compressive Strength (GPa) | (ksi) | Density (g/cm$^3$) |
|---|---|---|---|---|---|---|---|---|
| **Pitch-Based** | | | | | | | | |
| P-25 | Amoco | 159 | 23 | 1.38 | 200 | 1.15 | 167 | 1.90 |
| P-55 | Amoco | 379 | 55 | 1.72 | 250 | 0.85 | 123 | 2.00 |
| P-75 | Amoco | 517 | 75 | 2.07 | 300 | 0.69 | 100 | 2.04 |
| P-100 | Amoco | 724 | 105 | 2.24 | 325 | 0.48 | 70 | 2.15 |
| P-120 | Amoco | 827 | 120 | 2.24 | 325 | 0.45 | 65 | 2.18 |
| E-35 | DuPont | 241 | 35 | 2.33 | 410 | 1.26 | 183 | 2.10 |
| E-75 | DuPont | 517 | 75 | 3.10 | 450 | 0.81 | 117 | 2.16 |
| E-105 | DuPont | 724 | 105 | 3.31 | 480 | 0.74 | 107 | 2.17 |
| Dialead K-135 | Mitsubishi Kasei | 510 | 74 | 2.30 | 334 | 0.82 | 119 | 2.11 |
| **PAN-Based** | | | | | | | | |
| T-2 | PRChina | 172 | 25 | 2.24 | 325 | na | na | na |
| T-300 | Amoco | 231 | 34 | 3.24 | 470 | 2.88 | 417 | 1.79 |
| AS-4 | Hercules | 231 | 34 | 3.64 | 528 | 2.69 | 390 | 1.80 |
| T-40 | Amoco | 290 | 42 | 3.45 | 500 | 2.76 | 400 | 1.78 |
| G40-700 | BASF/Celion | 303 | 44 | 4.96 | 720 | na | na | 1.77 |
| IM6 | Hercules | 308 | 45 | 4.28 | 620 | na | na | 1.73 |
| G45-700 | BASF/Celion | 310 | 45 | 4.83 | 700 | na | na | na |
| IM8 | Hercules | 310 | 45 | 5.17 | 750 | 3.22 | 467 | 1.80 |
| HMS | Hercules | 345 | 50 | 2.21 | 320 | na | na | 1.83 |
| M40J | Toray | 390 | 56 | 4.40 | 638 | 2.33 | 338 | 1.77 |
| T-50 | Amoco | 393 | 57 | 2.41 | 350 | 1.61 | 233 | 1.81 |
| GY-70 | BA3F/Celion | 517 | 75 | 1.86 | 270 | 1.06 | 153 | 1.96 |
| M60J | Toray | 590 | 85 | 3.80 | 551 | 1.67 | 242 | 1.94 |
| **Rayon-Based** | | | | | | | | |
| WCA | Amoco | 69 | 10 | na | na | na | na | na |
| T-75 | Union Carbide | 538 | 78 | 2.62 | 380 | 1.03 | 149 | 1.80 |

na = value not available

2
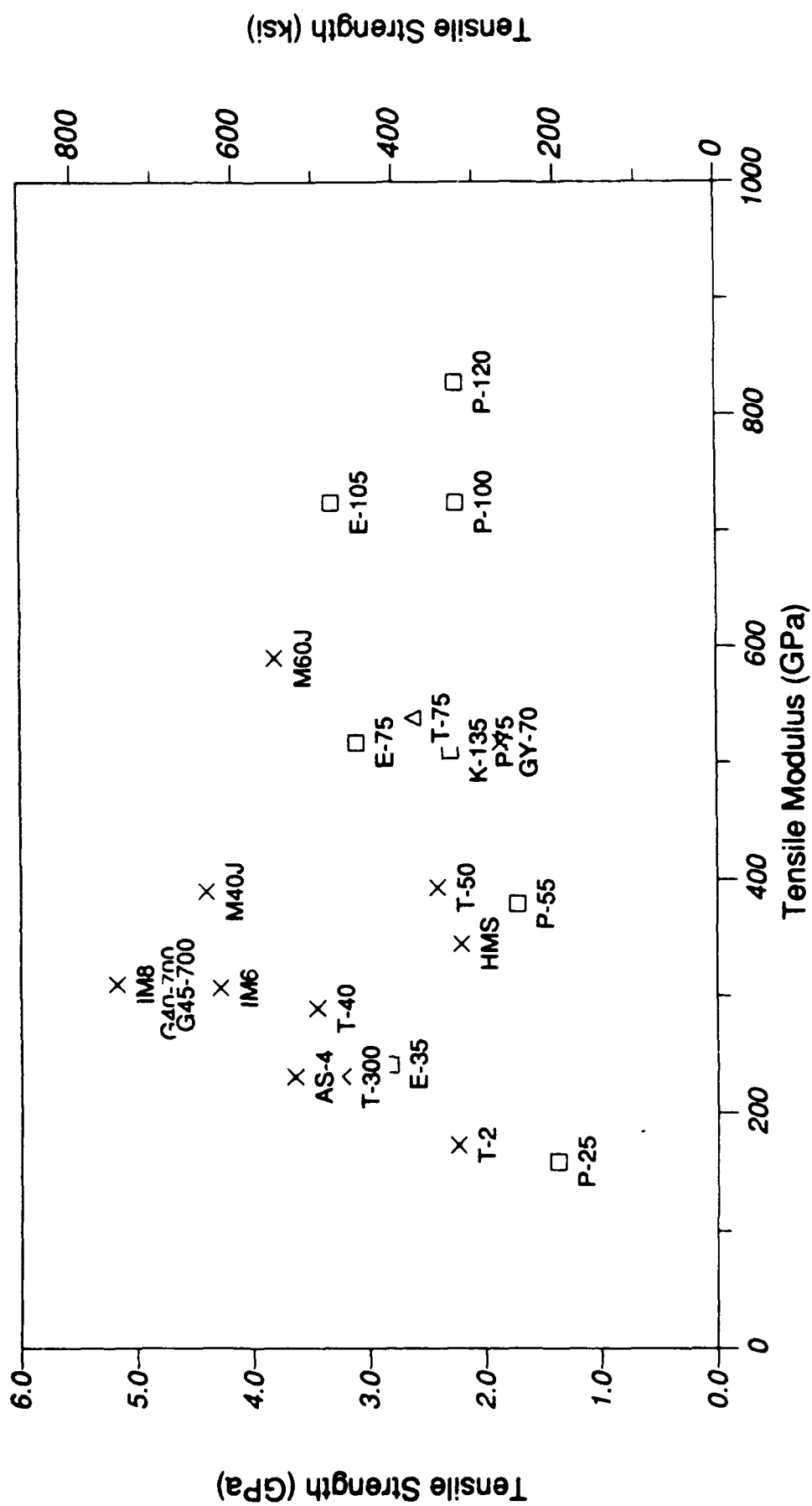
Figure 1. Tensile Strength versus Tensile Modulus for Carbon Fibers.
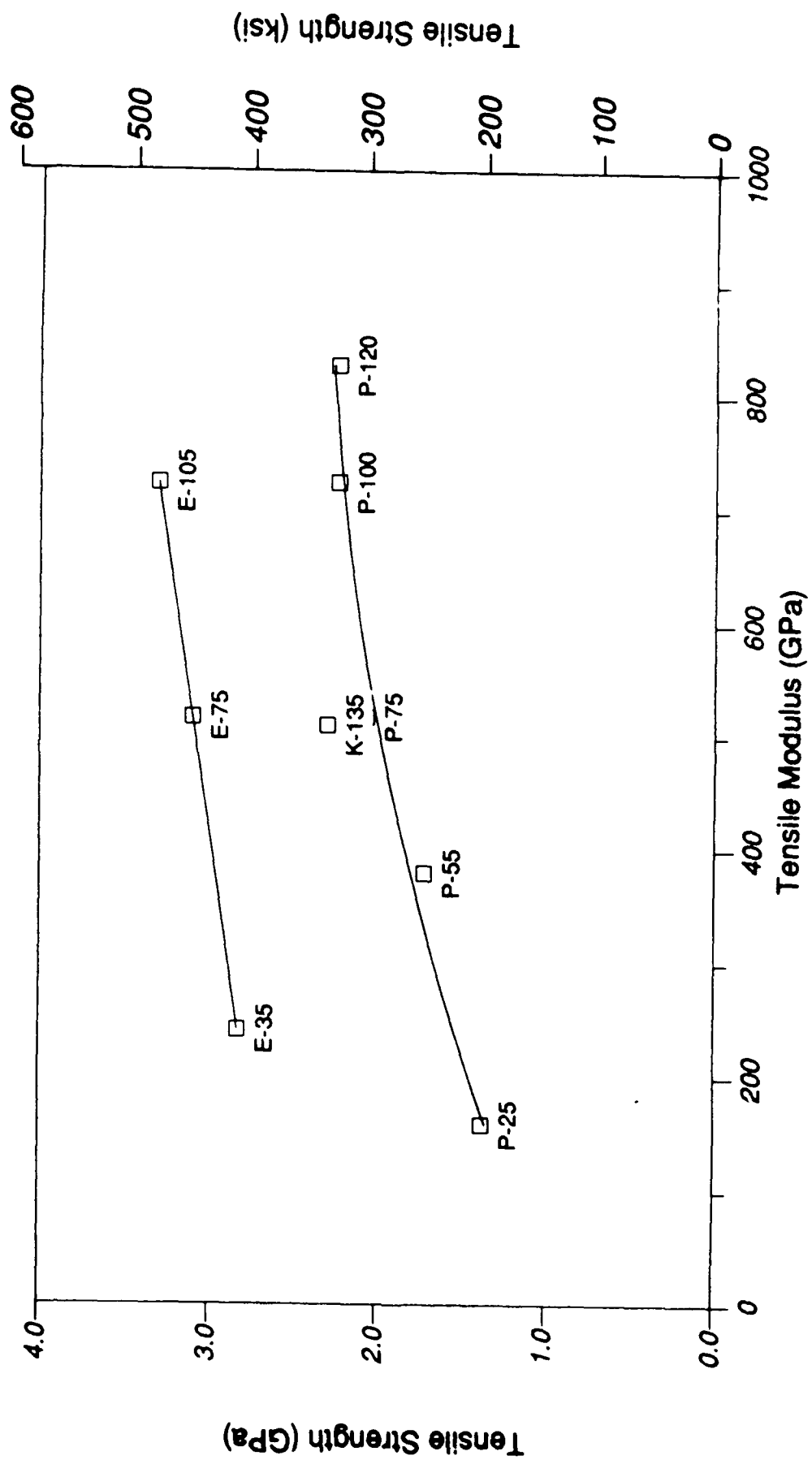
Figure 2. Tensile Strength versus Tensile Modulus for Pitch-Based Carbon Fiber.

4
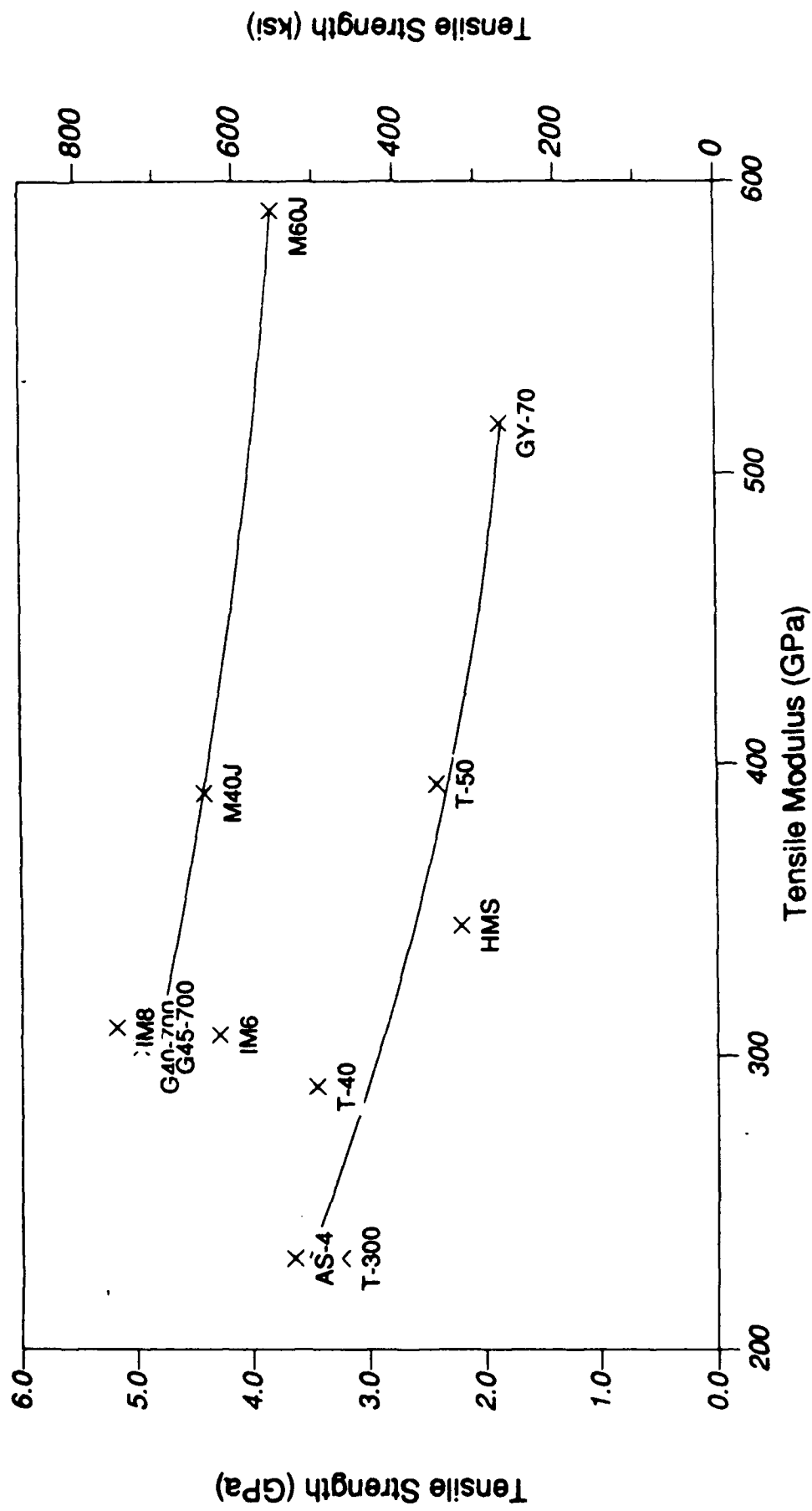
Figure 3. Tensile Strength versus Tensile Modulus for PAN-Based Carbon Fiber.

5

few fiber grades in any one series of PAN-based fibers to make a direct comparison; however, it is one of the same correlations found by Sumida et al. [5].

Plotting TM versus strain to failure (TS/TM) in Figure 4 shows the well-known general trend of low failure strain for higher TM. Figure 5 shows this plot for the pitch-based fibers which shows the newer DuPont E-series having greater failure strain for a given TM than the Amoco P-series. The PAN-based fibers of Figure 6 show the same trend, with the newer Toray fibers, etc. having higher failure strains for a given TM than the other fibers.

For the same tensile modulus, pitch- and PAN-based carbon fibers show an even greater difference in compressive strength (CS) as seen in Figure 7, while both precursor types show an apparent inverse correlation between compressive strength and tensile modulus. It should be remembered that the reported compression strength of the low and intermediate modulus PAN-based fibers are not from true fiber compression failure. The drop in compressive strength with increasing tensile modulus is steeper for the PAN-based fibers. It has been reported [5] that morphological changes in the PAN-based fibers can result in higher compressive strengths for the same tensile modulus. As a result two curves exist for these fibers: a lower one for older fibers and an upper one for the newer Toray and Hercules IM fibers. This can be seen in Figure 8 which is an expanded view of Figure 7 for PAN-based fibers. A similar plot can also be constructed for the pitch-based fibers (Figure 9) [4] showing two separate curves: the lower one for the older Amoco P-series and the upper one for the newer DuPont E-series and Dialead K-135 fibers.

A plot of strengths (CS versus TS) in Figure 10 surprisingly only shows a very weak correlation. For pitch-based fibers (Figure 11) CS decreases as TS increases within any production series (Amoco P- or DuPont E-series). The PAN-based fibers show the reverse trend of increased CS as TS increases (Figure 12), again with the Toray fibers at greater CS and TS for any given TM. The reasons for the differences in trends between the pitch- and PAN-based fibers are not known at this time.

Any correlation of these mechanical properties with fiber density is also fairly limited. Figure 13 is shown as an example (with TM vs. density) which mostly shows that for a given TM the pitch-based fibers are more dense than the PAN- and rayon-based fibers. The plot also shows that within a series, TM increases as the density increases; the DuPont fiber series having greater densities than corresponding Amoco fibers.

6
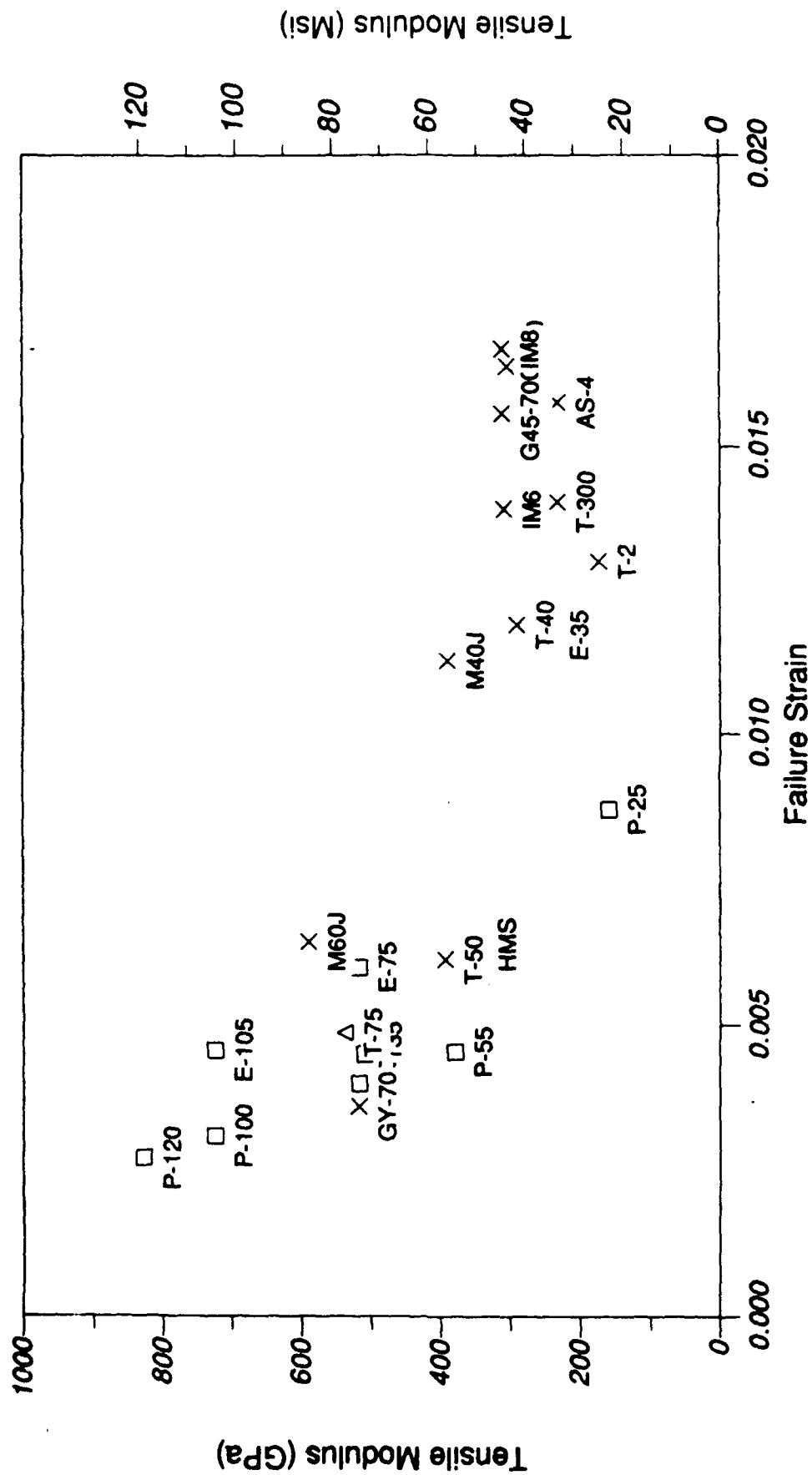
Figure 4. Tensile Modulus versus Tensile Failure Strain for Carbon Fibers.

7
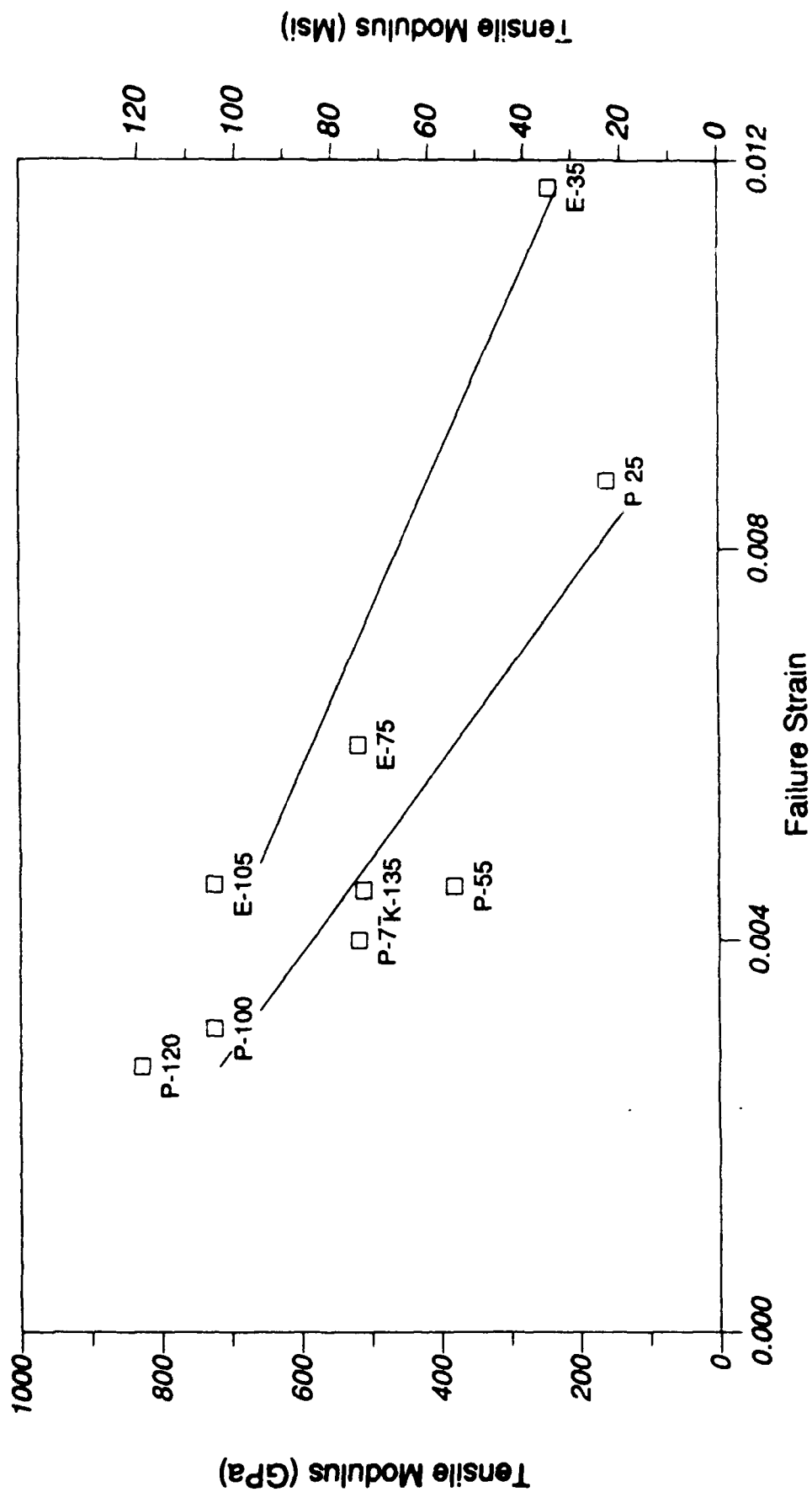
Figure 5. Tensile Modulus versus Tensile Failure Strain for Pitch-Based Carbon Fibers.
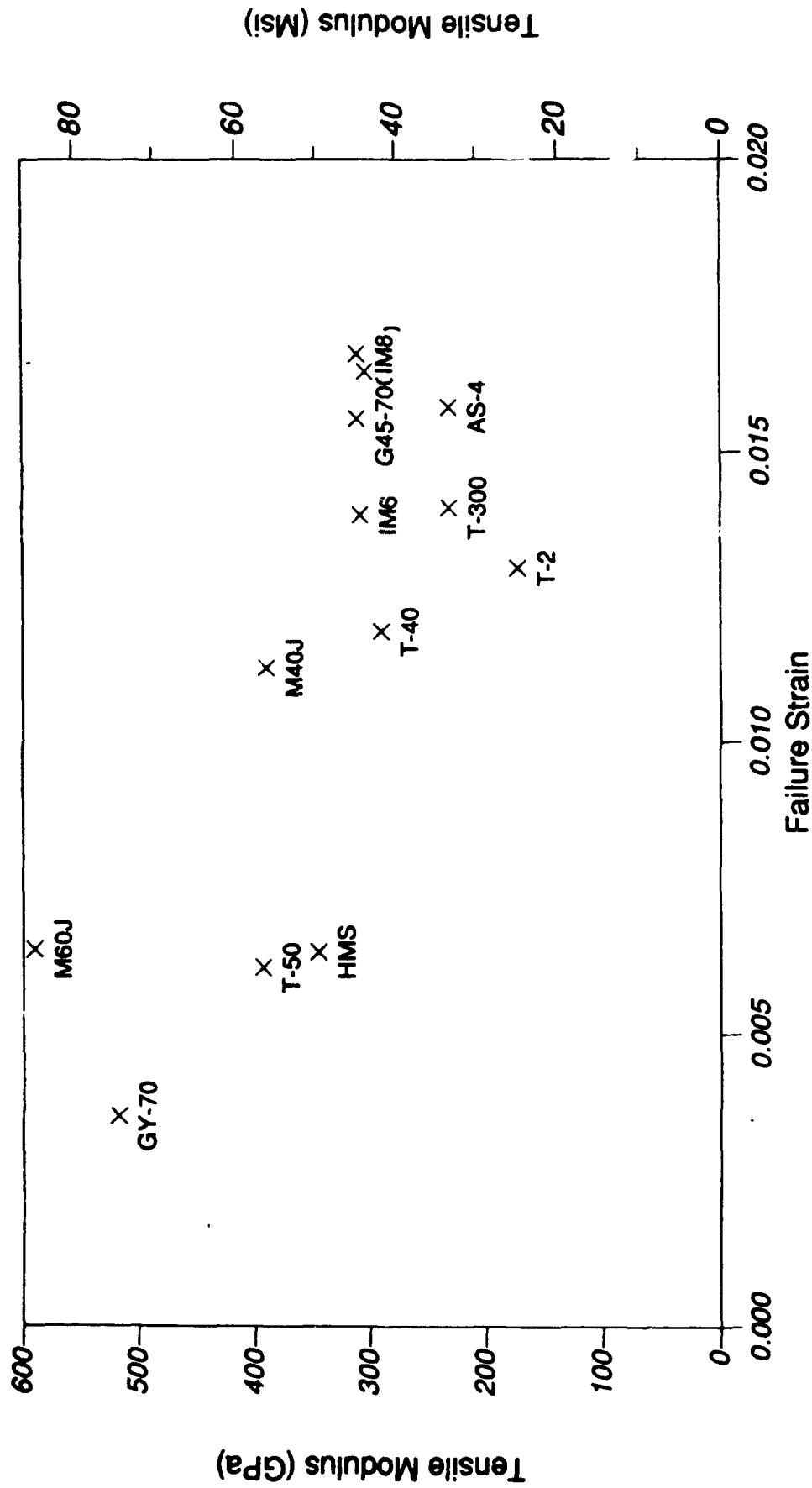
Figure 6. Tensile Modulus versus Tensile Failure Strain for PAN-Based Carbon Fibers.

9
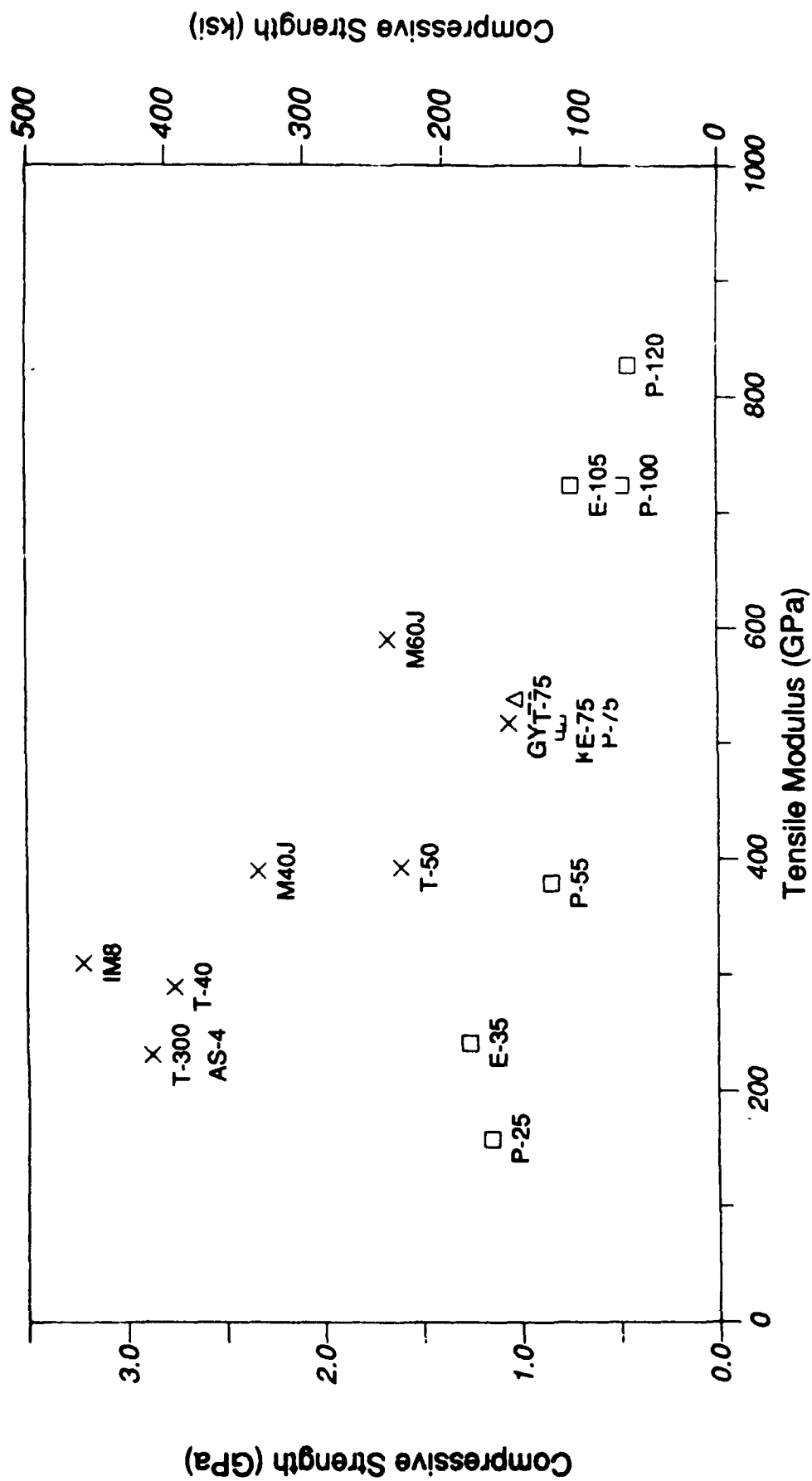
Figure 7. Compressive Strength versus Tensile Modulus for Carbon Fibers.

10
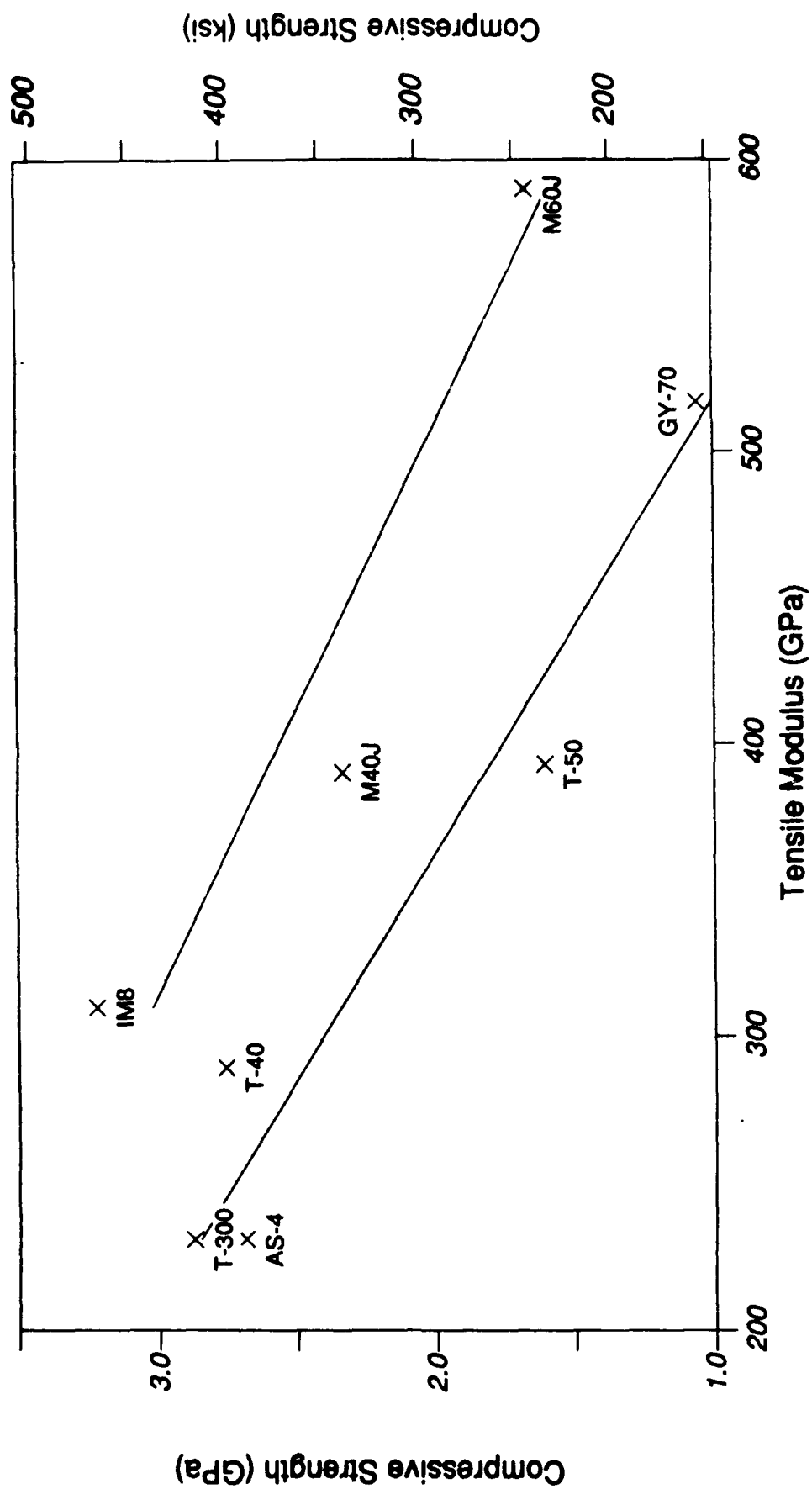
Figure 8.  Compressive Strength versus Tensile Modulus for PAN-Based Carbon Fibers.
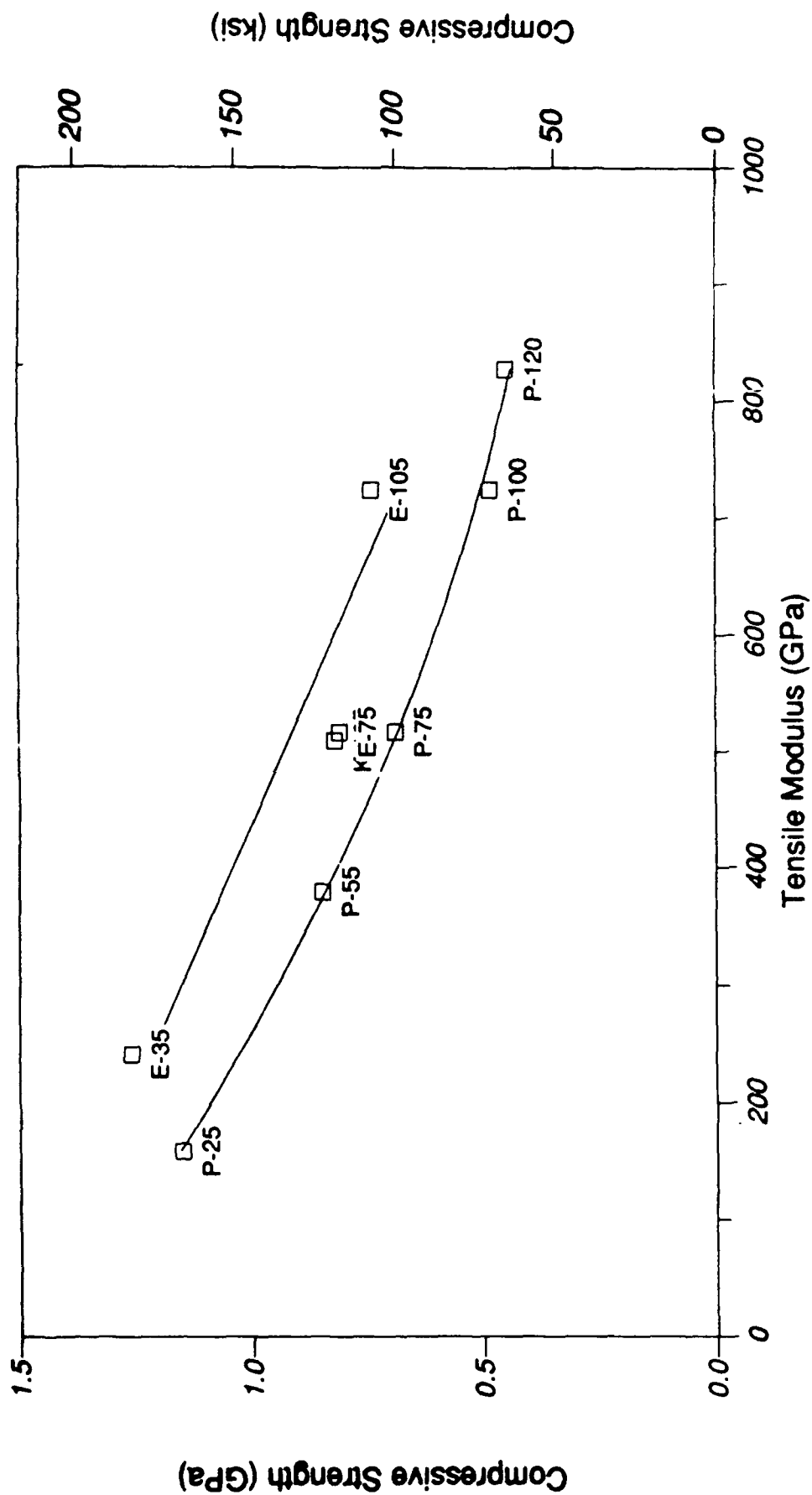
Figure 9.  Compressive Strength versus Tensile Modulus for Pitch-Based Carbon Fibers.
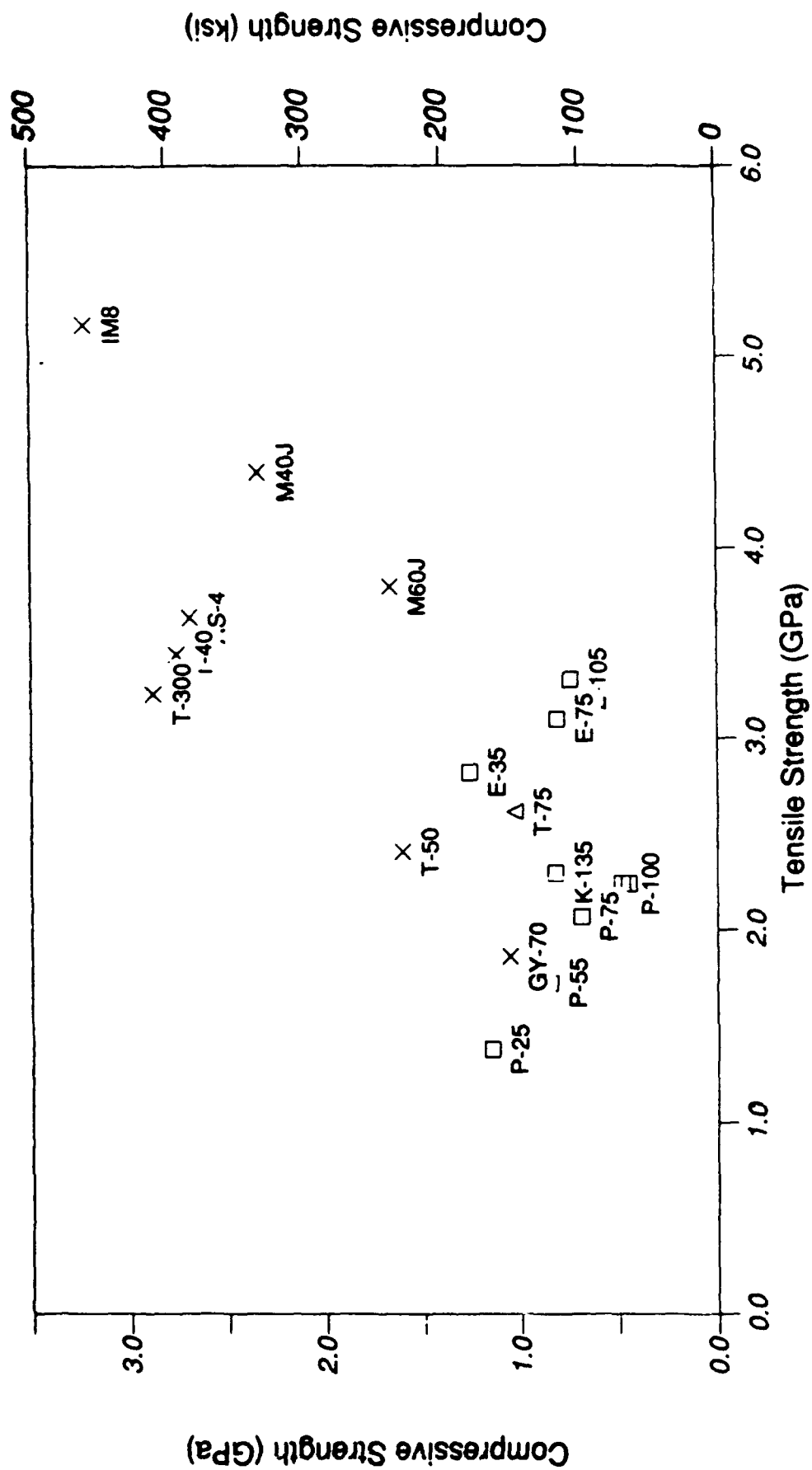
Figure 10.   Compressive Strength versus Tensile Strength for Carbon Fibers.
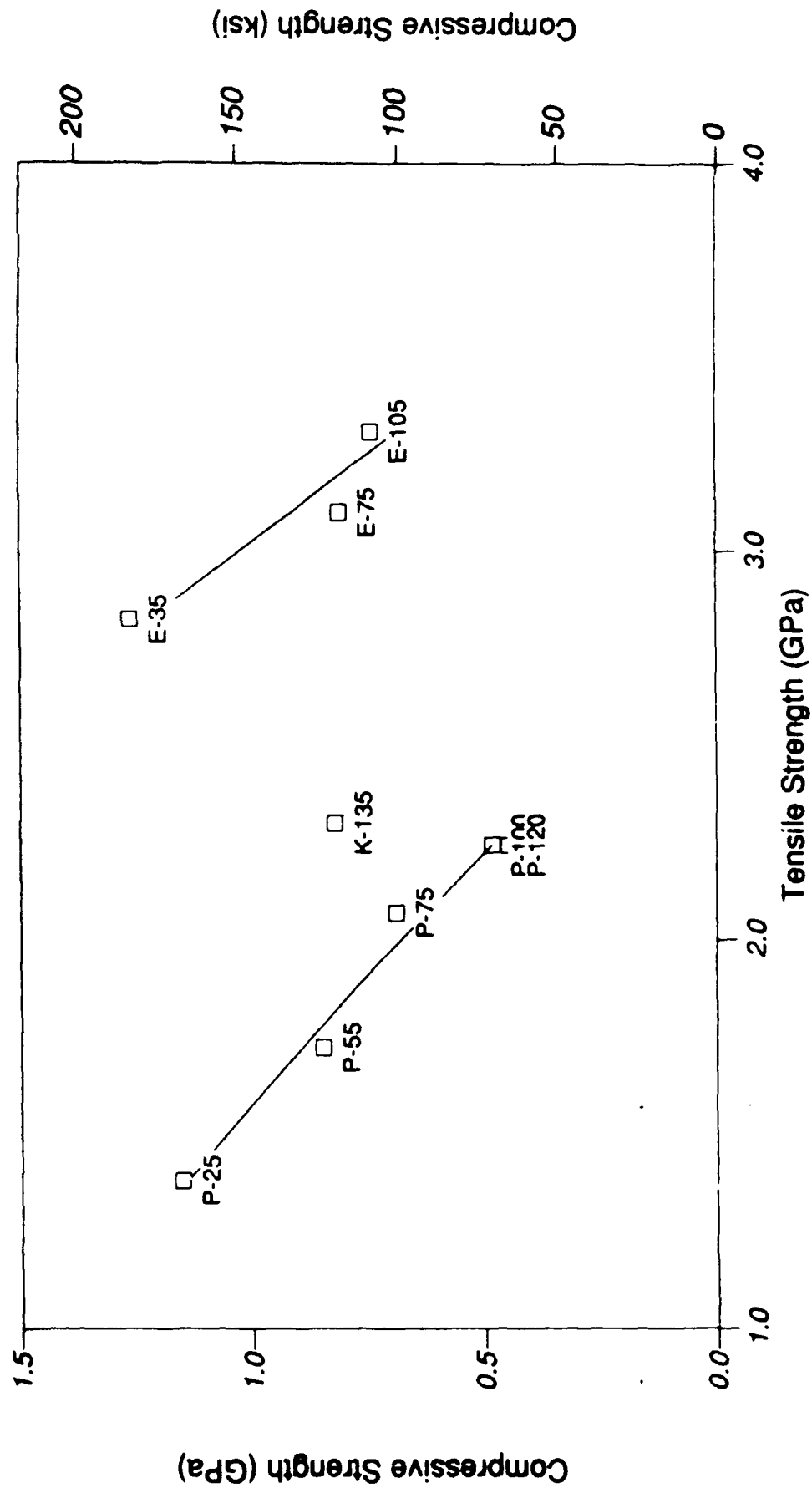
Figure 11. Compressive Strength versus Tensile Strength for Pitch-Based Carbon Fibers.
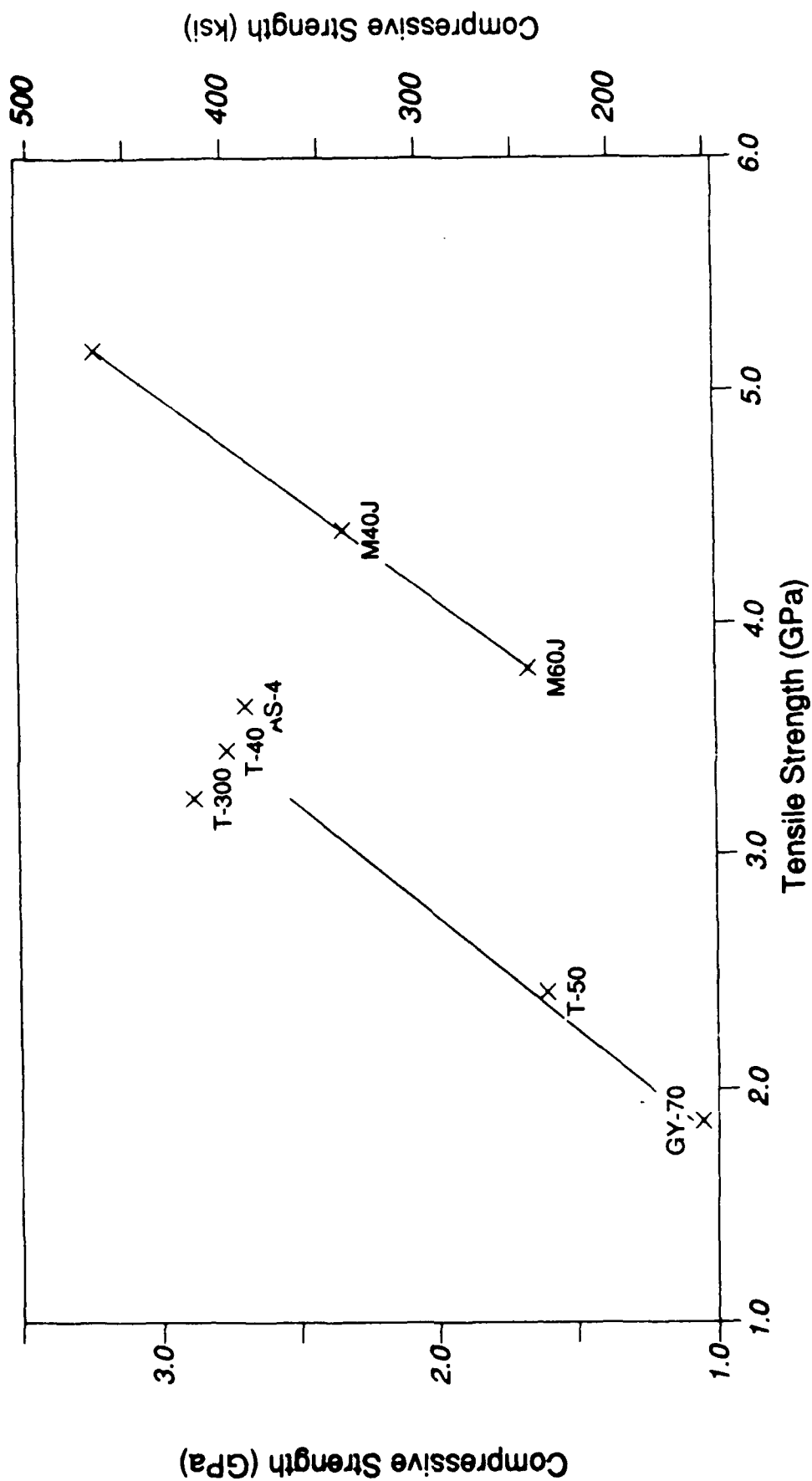
Figure 12. Compressive Strength versus Tensile Strength for PAN-Based Carbon Fibers.
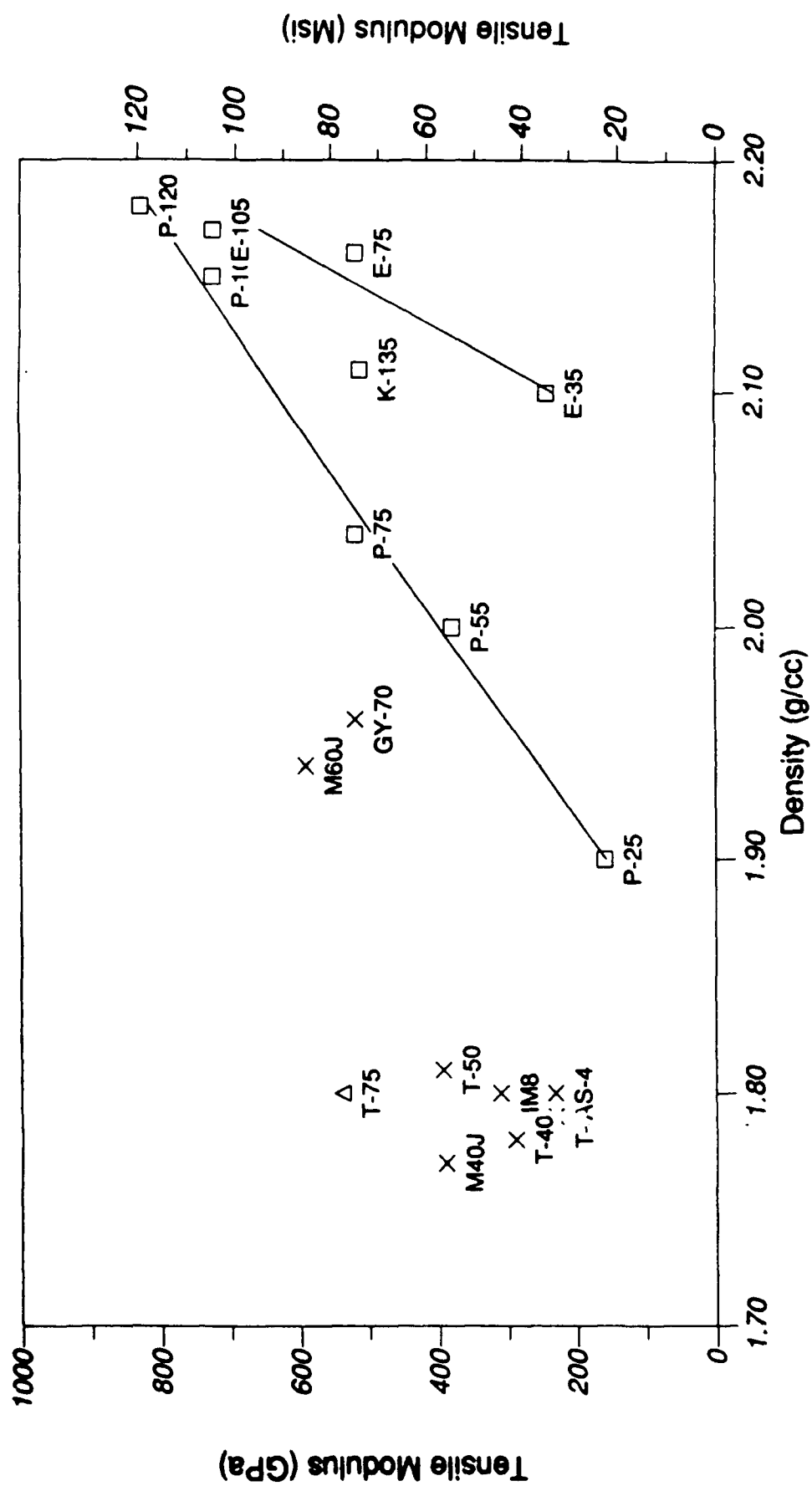
Figure 13. Tensile Strength versus Fiber Density for Carbon Fibers.

16

# 2. COLLECTION AND ANALYSIS OF DATA

## 2.1 EXPERIMENTAL PROCEDURE

Fiber bundles were mounted on cardboard holders using a few drops of Loctite M-Bond 200 methyl-2-cyanoacrylate glue. The glue wicked the fibers together into tight parallel bundles and did not contribute to the x-ray scattering in any of the regions of interest. These samples were mounted with the fiber bundle direction vertical ($\chi=0°$) in a 4-circle x-ray diffractometer. CuK$\alpha$ radiation ($\lambda=0.15418$ nm) from a Rigaku RU-200 rotating anode generator at a power of 45 kV and 70 mA was the x-ray source. Equatorial, meridional, and off-axis Bragg scans were obtained by tilting the fibers at $\chi=0$, 90, and 70, respectively.

Precise positions of the $(00,\ell)$ peaks were obtained by curve fitting with Pearson Type VII profiles [14] after the samples' misalignment was corrected for by averaging selected peak positions from positive and negative Bragg angle scans. Detection of 3-dimensional crystallinity in fibers was achieved by observing the $(10,1)$ and $(11,2)$ peaks in the off-axis Bragg scans. Because these off-axis plane normals are tilted approximately 20° to the fiber axis [1,15], these reflections are not observable in equatorial or meridional Bragg scans but can be observed at $\chi=70°$.

## 2.2 CRYSTALLITE SIZE CORRECTIONS TO INTENSITY

In the first technical report [1], the data was curve fit after standard intensity corrections for absorption, polarization, and air scatter [14]. Corrections for the Lorentz factor and structure factors had not been made. Northolt and Stuut [16] described this method as a means of correcting the intensity for crystal size effects, although these corrections had been generally mentioned much earlier by Franklin [17,18]. Jain and Abhiraman [19] demonstrated that these corrections can make significant differences in the calculated d-spacings because of their angular dependence. The values of these factors are plotted in Figure 14 as a function of Bragg angle in the (00,2) region. Figures 15 and 16 show the changes in carbon fiber normalized equatorial Bragg scans when these corrections are made for P-25 and P-100, respectively. The lower modulus P-25 was affected more than the higher modulus fibers, as its smaller crystallite sizes produce broader peaks. This results in the additional corrections being spread over a larger angular region which causes the peak maximum to shift to higher angles.

17
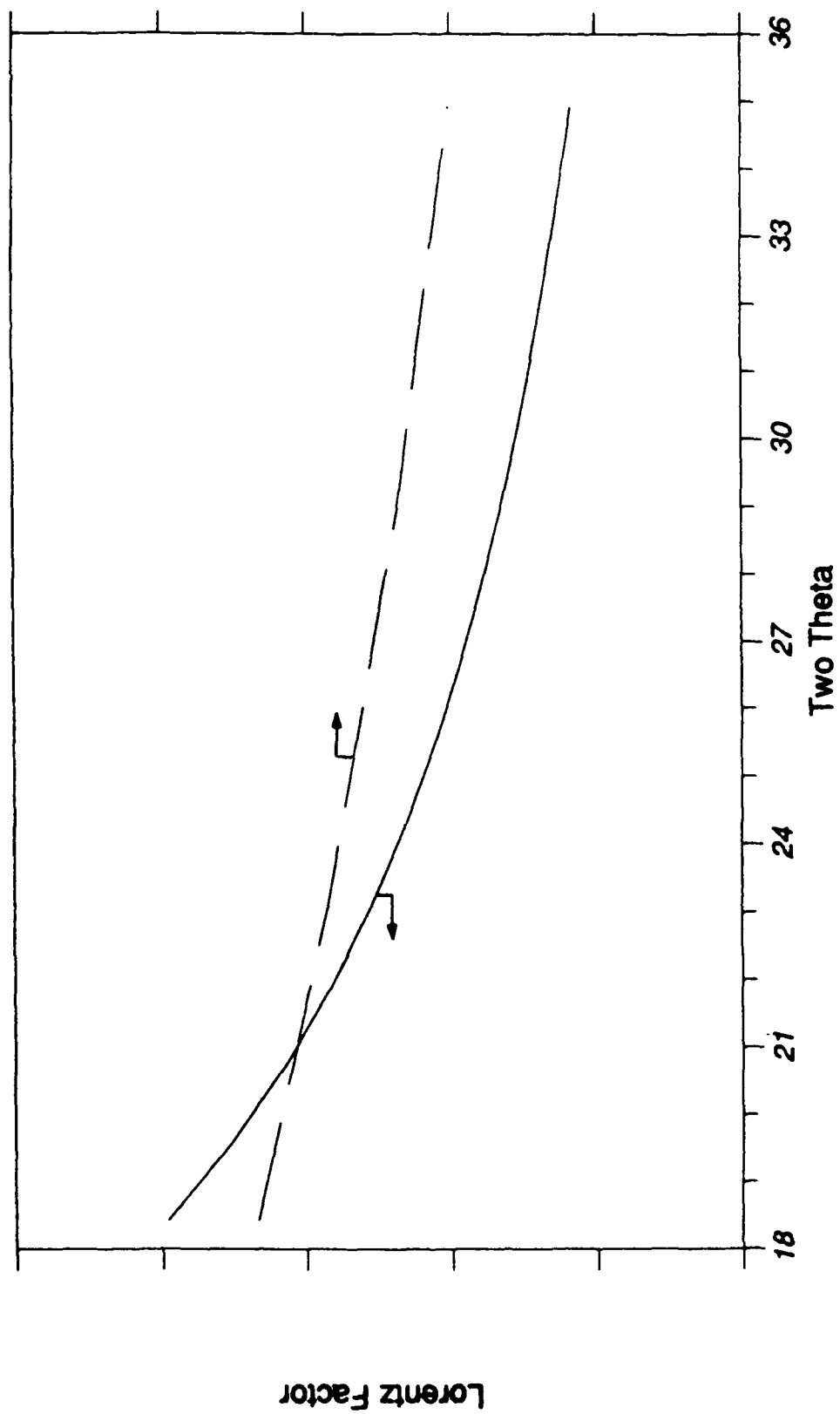
Figure 14.  Lorentz (Solid Line) and Structure (Dashed Line) Factors (Arbitrary Units in the Ordinate Axis) Plotted versus Bragg Angle for CuKα Radiation.

18
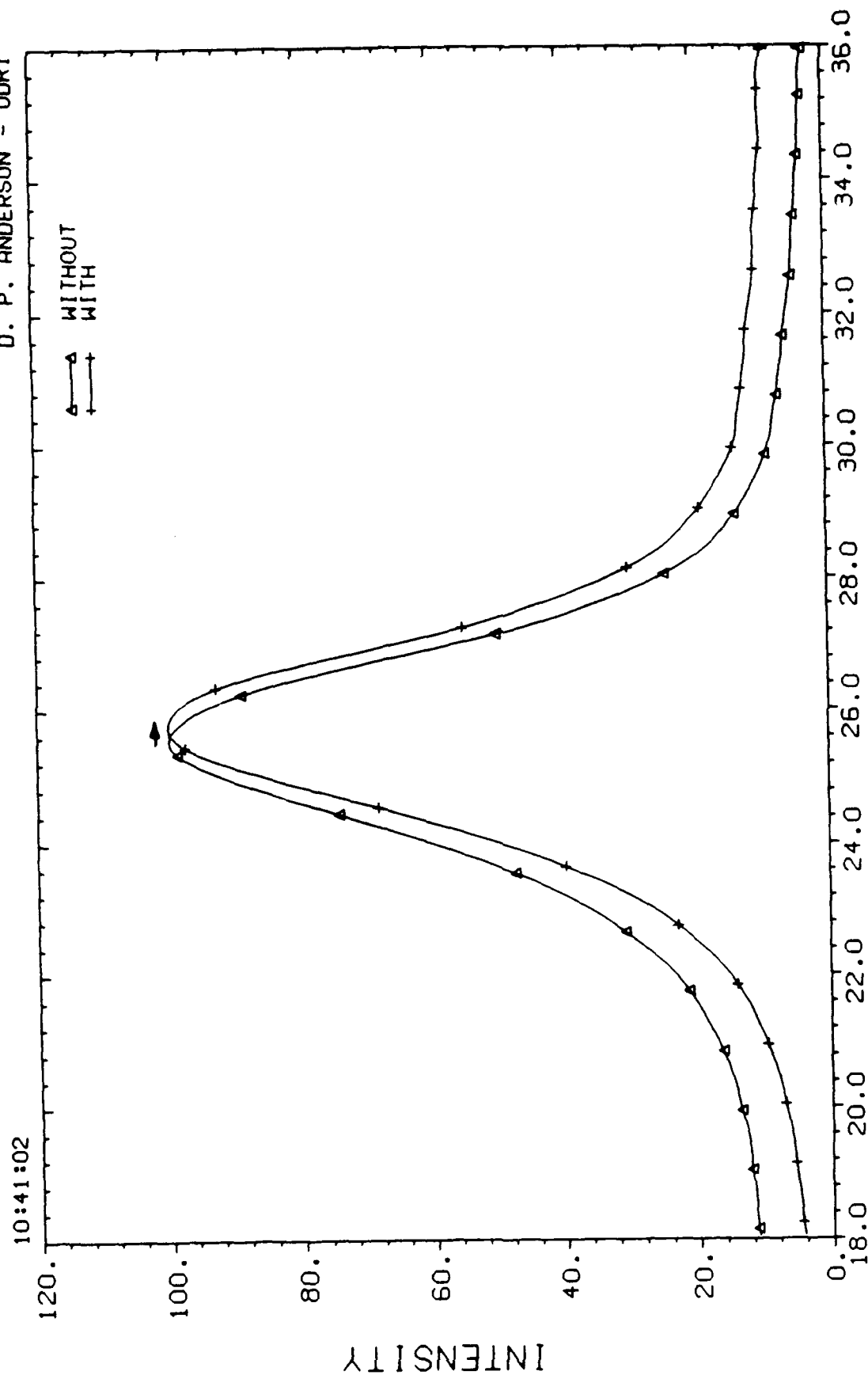
Figure 15.  Bragg Scan of P-25 With and Without the Lorentz and Structure Factor Corrections.

19
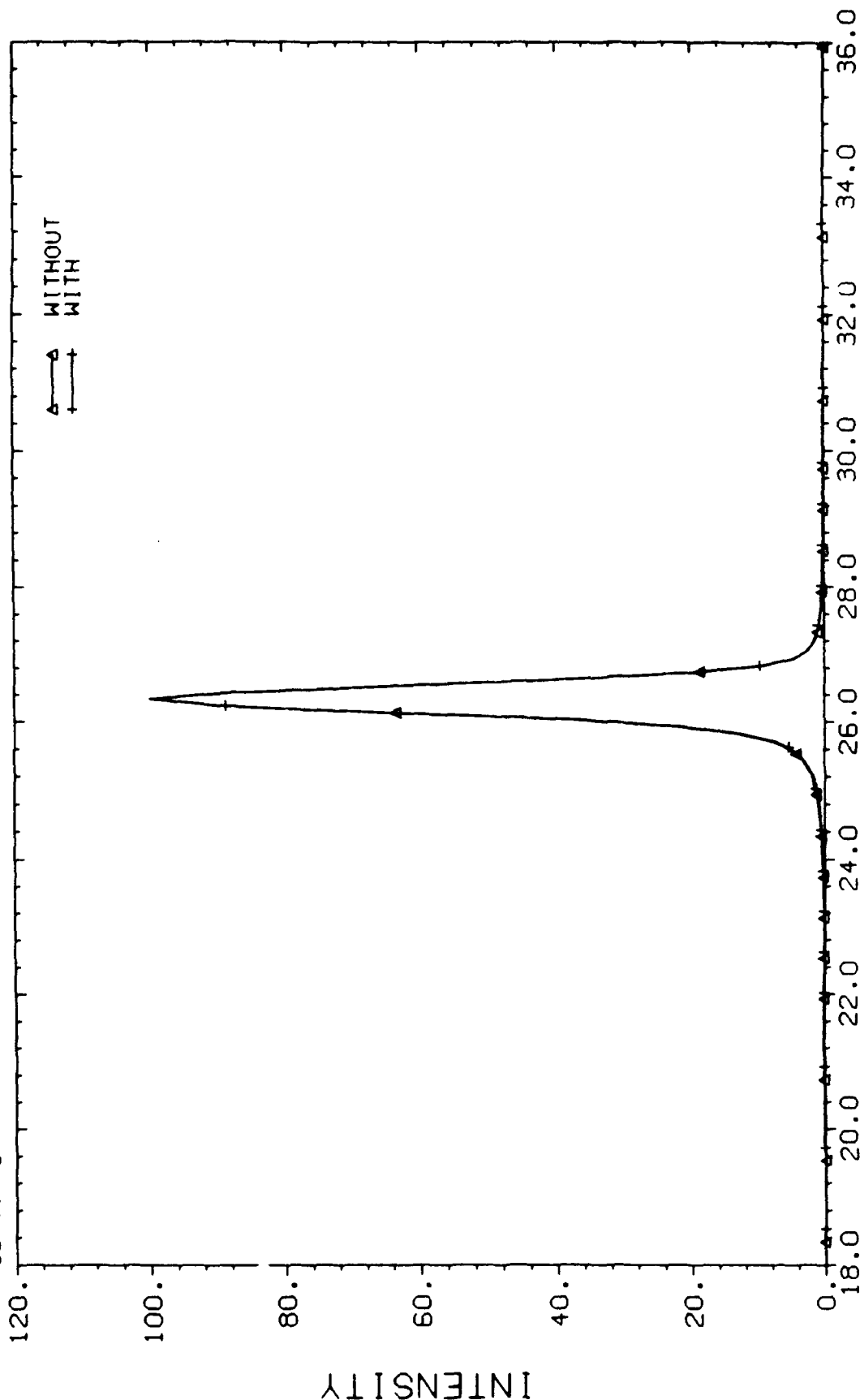
Figure 16.   Bragg Scan of P-100 With and Without the Lorentz and Structure Factor Corrections.

The difficulty in this technique results from these corrections changing with material and crystalline reflection. Both the Lorentz and structure factors are a function of scattering angle and diffracting plane.

The Lorentz factor changes for different reflections, since it is basically a means to account for crystal planes whose diffraction is not measured at all possible angles of sample to diffractometer. The axial orientation of the fibers allows simpler data collection as long as the Lorentz factor (L) is used to calculate the true intensities. General equations by de Wolff [20] can be used for fibers:

Equatorial reflections:

$$L_{(00,\ell)} = (\sin^2\theta \, \cos\theta)^{-1} \tag{1}$$

Meridional reflections:

$$L_{(hk,0)} = (\sin^2\theta \, \cos\theta \, t)^{-1} \tag{2}$$

General reflections:

$$L_{(hk,\ell)} = (\sin^2\theta \quad \cos\theta \, \sin\phi_{hk\ell,z})^{-1} \tag{3}$$

where $\phi_{hk\ell,z}$ is the angle between the fiber axis and the diffracting plane's normal, and t can be approximated by:

$$t = 0.815 \, \beta_{1/2} \text{ (radians)} \tag{4}$$

where $\beta_{1/2}$ is the azimuthal half-width at half-height.

While the Lorentz factor for equatorial reflections is easily calculated, for other scans this calculation is more complex. In the meridional scans the value of $\beta_{1/2}$ is not usually available and is not measurable in these systems which include 2-D reflections [i.e. (11) reflection]. While the $\phi_{hk\ell,z}$ is available for the 3-D reflections [i.e. (11,2)] in the off-axis scans, the presence of overlapping 2-D and 3-D meridional [i.e. (11,0)] reflections prevents any accurate calculation of a Lorentz factor.

21

The structure factor (F) is also dependent on the crystalline reflection whose intensity one wishes to correct. For a crystal whose unit cell contains n atoms, the structure factor for the $(hk, \ell)$ reflection is:

$$F(hk, \ell) = \sum_n \{f_n \exp[2 \pi i(h x_n + k y_n + \ell z_n)]\} \quad (5)$$

where $f_n$ is the atomic scattering factor for the nth atom, and $x_n$, $y_n$, and $z_n$ represent the position of that atom in the unit cell in fractional units.

For equatorial reflections, $(00, \ell)$, in carbon fibers, the structure factor, $F_{(00, \ell)}$, is simply a constant times the atomic scattering factor of carbon; the constant for the (00,4) and (00,6) reflections are twice and three times, respectively, that of the (00,2) reflection. Since these reflections are well separated and analyzed independently, the constant is dropped. The same is true for the meridional scans.

The off-axis scans, on the other hand, are more difficult to correct, since the (11), (11,0), and (11,2) reflections [or the (10), (10,0), and (10,1)] often overlap as three dimensionality becomes apparent in the crystals, and these reflections have slightly different structure factors.

The net result of these difficulties is that the Lorentz factor and structure factor corrections were only applied to the equatorial scans which affected d-spacings and crystallite size measurements in the c-direction.

## 2.3    EQUATORIAL BRAGG SCAN ANALYSIS

After all the data corrections discussed above have been applied, the $(00, \ell)$ reflections are curve fit to a Pearson Type VII profile. The interplane graphitic spacing, $d_{(00,2)}$, is calculated from the peak positions from Braggs' law:

$$d_{(hk, \ell)} = \lambda/(2 \sin\theta) \quad (6)$$

where $\lambda$ is the wavelength of x-rays, for $CuK\alpha$, $\lambda = 0.15418$ nm, and $\theta$ is one-half the scattering angle ($2\theta$ is the scattering or Bragg angle).

The results reported in this report are averages of the available $(00,\ell)$ results. A weighted average was used where the $(00,2)$ results had a weighting of unity, the $(00,4)$ a weighting of one-half, and the $(00,6)$ (if present) one-third.

A degree of graphitization $(g_p)$ can be calculated from this d-spacing [21]:

$$g_p = (0.344 - d_{(00,2)})/(0.344 - 0.3354) \tag{7}$$

where 0.344 nm is the interplane spacing in turbostratic carbon, and 0.3354 nm is the interplane spacing in fully graphitic carbon.

Equation 7 also points to the precision problem in carbon fiber d-spacings, i.e. at low degrees of graphitization it is more difficult to measure the d-spacings, and hence only three significant figures can be reported. Some of the d-spacings are reported to three significant figures and others to four significant figures indicating the confidence of the reported values.

It has been reported [22] that the fiber density can be used with the measured d-spacing $(00,2)$ to calculate the void content of the fibers:

$$\text{Void Content (\%)} = \left(1 - \frac{\rho_{fiber} d_{(hk,\ell) fiber}}{\rho_{graphite} d_{(hk,\ell) graphite}}\right) \times 100 \tag{8}$$

where $\rho_{graphite}$ = 2.26 g/cm , and $d_{(hk,\ell) graphite}$ = 0.3354 nm. This parameter, void content, was calculated for fibers whose densities were known.

The crystallite size $(L_c)$ can be calculated from the Scherrer equation [23] from the peak integral breadth once the instrumental breadth is subtracted:

Scherrer:

$$L_{hk,\ell} = L_c = \lambda/(\beta_s \cos\theta) \tag{9}$$

and

$$(\beta_s)^2 = (\beta_0)^2 - (\beta_i)^2 \tag{10}$$

where $\beta$ is the integral breadth in $2\theta$ radians, "s" the sample caused broadening, "i" indicates the instrumental contribution, and "o" indicates the experimentally observed broadening.

The instrumental line broadening was determined using hexamethylene tetramine crystals which were so large that essentially all the observed broadening in their scans can be assumed due to instrumental effects. Equation 10 also assumes that both the instrumental and samples profiles are of a Gaussian nature. The instrumental broadening profiles were in fact Gaussian, although the sample profiles were not always so. The sample profiles approached Gaussian shape as the breadth narrowed, where the corrections are most critical. Where the sample profiles deviated significantly from Gaussian, their breadth made the correction difference between the Gaussian used and some other correction such as Cauchy, insignificant; the Gaussian was used throughout for consistency.

The Scherrer analysis was chosen over more sophisticated analyses such as the Hosemann analysis [24,25] or the method of Buchanan and Miller [26] because such analyses involve significantly more work without resulting in any greater useful knowledge.


## 2.4   AZIMUTHAL SCAN ANALYSIS

Of the many measurements of graphene plane orientations, the simplest to measure is "Z." This is simply the full-width at half-maximum of the azimuthal scans of the (00,2) reflection.

A more precise measure which can be applied is the calculation of the Hermans' orientation function, $f_{hk\ell}$, from the azimuthal intensity scans:

$$f_{hk\ell} = (3 <\cos^2 \phi> - 1)/2 \qquad (11)$$

where $<\cos \phi>$ is the average cosine squared of the intensity as a function of azimuthal angle, $\phi$. This angle $\phi$ is the complement of the measured $\chi$ angle.

$$\langle \cos^2 \phi \rangle = \frac{\int_o^{\pi/2} I(\phi)\cos^2 \phi \sin \phi \, d\phi}{\int_o^{\pi/2} I(\phi) \sin \phi \, d\phi} \qquad (12)$$

24

This method, in fact, calculates the first Legendre polynomial coefficient of the spherical harmonics describing the overall orientation distribution for the crystals in a sample.

While this calculation can be easily performed during the computer analysis of the data, it suffers from a baseline problem. Figure 17 is a typical azimuthal scan which shows a small but significant baseline. This small intensity contributes significantly to the average cosine squared but is not really a part of the scan. Subtraction of the proper baseline is difficult particularly when the baseline is not flat.

In addition, instrumental broadening and fiber misalignment in the fiber bundle reduce the accuracy of any orientation measurement. The instrumental contribution is estimated (from other work [27]) to change the Z only a few tenths of a degree for the most narrow distributions. The fiber misalignment is considered minimal but finite and unmeasurable at this time. Since the orientation of the graphene planes is only used as a semi-quantitative parameter, the $Z_{(00,2)}$ value was considered sufficiently accurate.

One other problem is the use of a simple azimuthal scan versus the integrated intensity as a function of azimuthal angle. The considerable breadth of the (00,2) peak in the Bragg direction is significantly greater than the instrumental resolution and would require the use of an integrated intensity for the Hermans' orientation function calculation which greatly increases the experimental difficulties without increasing the useful data significantly.

If needed or desired the Hermans' orientation function can also be estimated from the value of Z and a knowledge of the profile shape. This estimation technique does eliminate the baseline problem but does not remove the other difficulties. Appendix A shows how this type of estimation can be performed.

## 2.5    $L_a$ MEASUREMENTS

The asymmetry of the (10) and (11) reflections at $\chi = 70°$ can be seen in Figures 18 and 19, respectively. This typical 2-dimensional crystalline behavior complicates the analysis of carbon fiber crystallite sizes. The values of $L_a$ reported here were calculated from the asymmetric (11) reflection of the fibers taken at a tilt angle ($\chi$) of 70° using Ruland's equation [28,29]:

$$L_a = L_{hk} = 1.84 \, \lambda / B_{(1/2,2\theta)} \cos\theta \qquad (13)$$

25
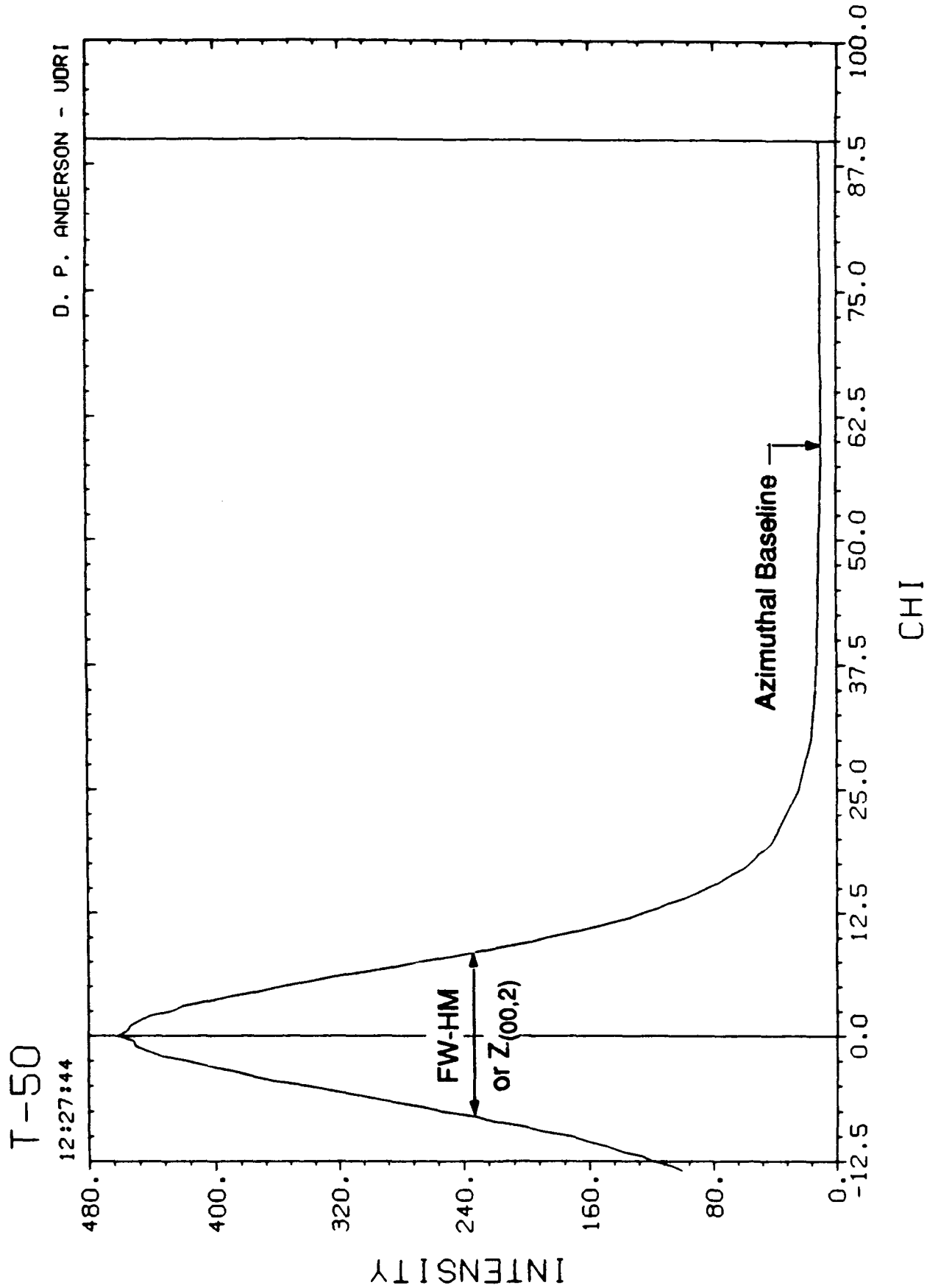
Figure 17. Typical Azimuthal Scan of Intensity versus χ Angle (T-50 Fiber).
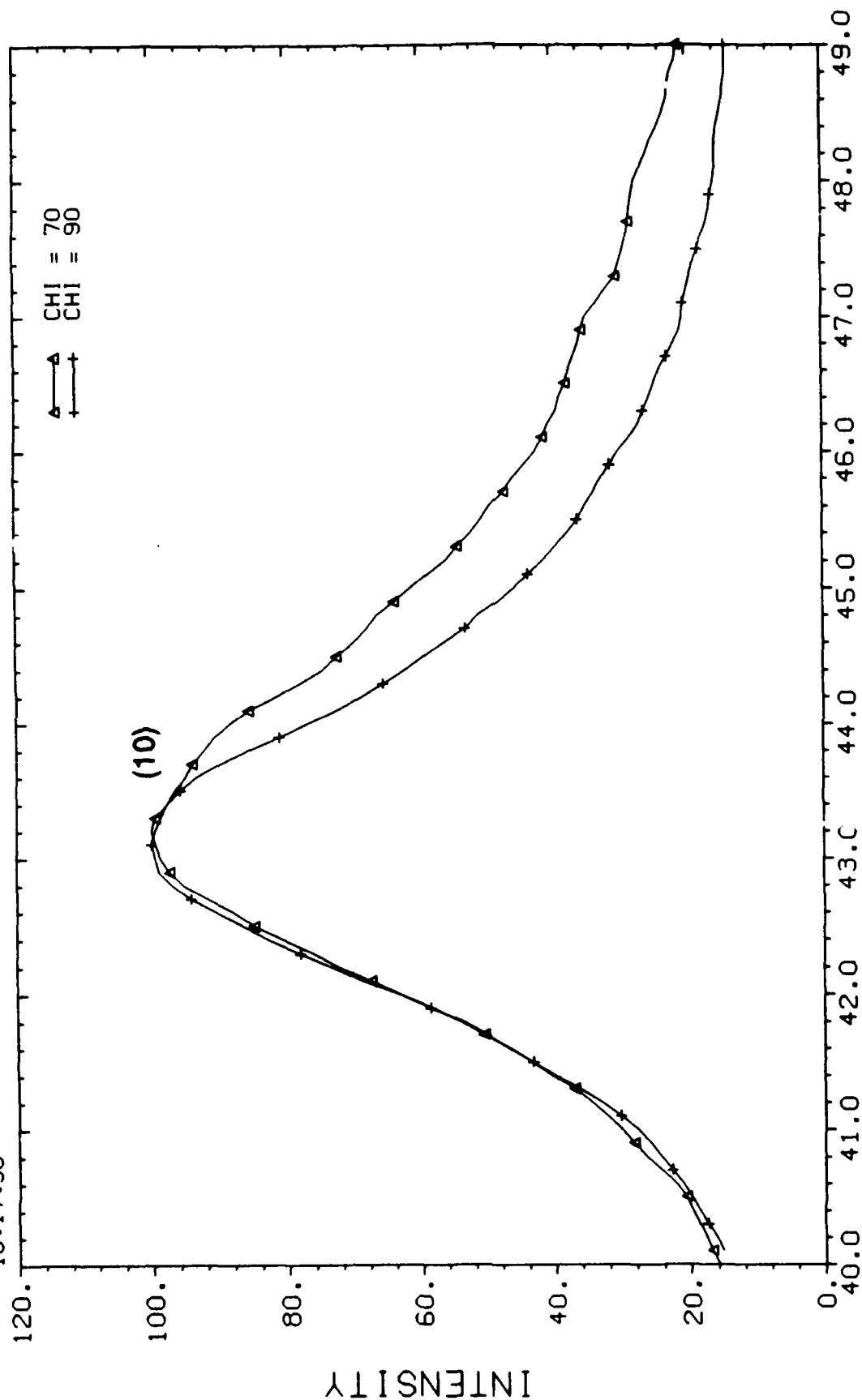
Figure 18. Bragg Scans of P-25 Fiber Bundle at χ=70° and χ=90° [(10) Region].

27
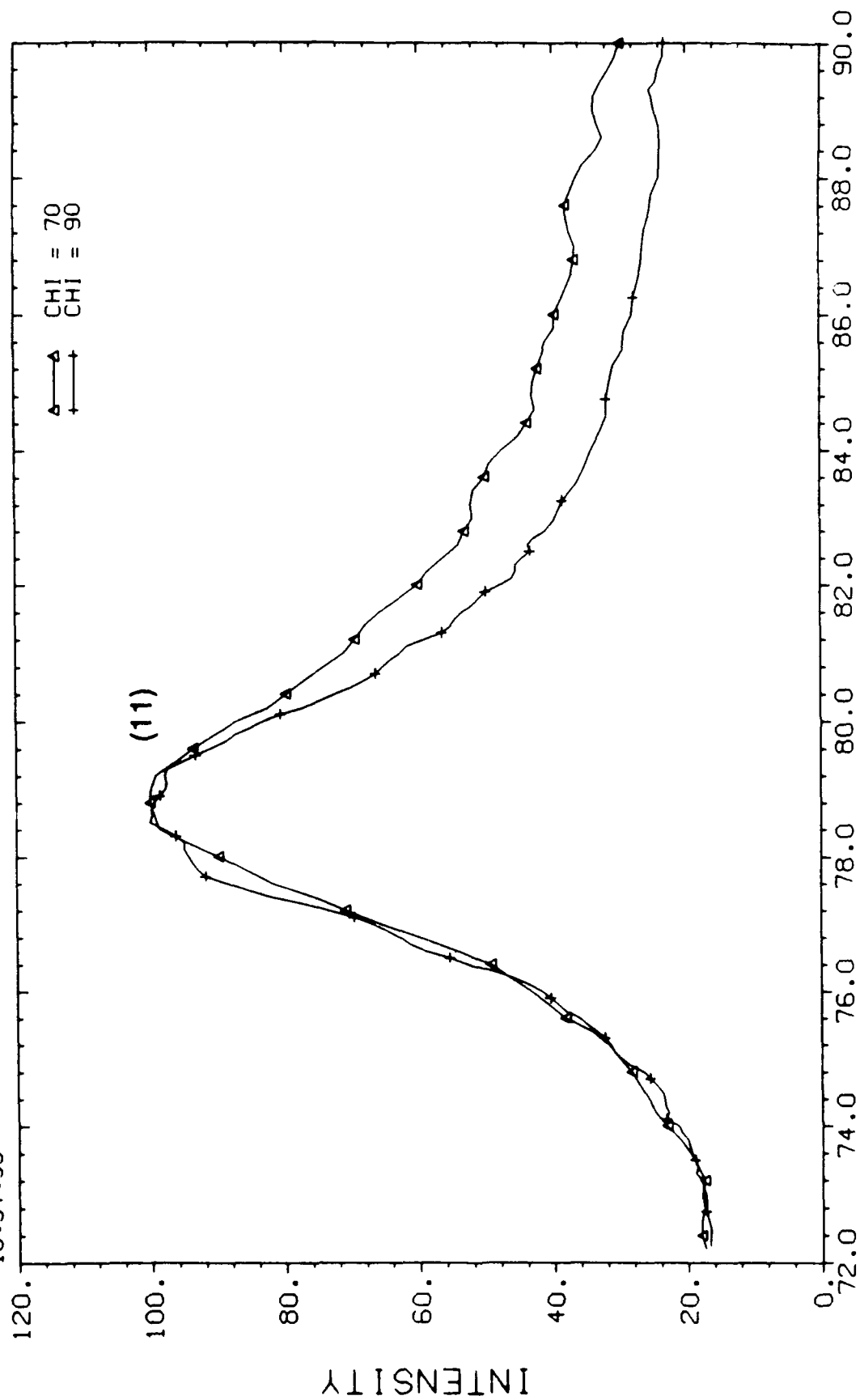
Figure 19. Bragg Scans of P-25 Fiber Bundle at $\chi=70°$ and $\chi=90°$ [(11) Region].

where $B_{(1/2,2\theta)}$ is the measured full-width at half-maximum (in radians) of the asymmetric profiles.

Alternatively:

$$L_a = L_{hk} = 1.84/B_{(1/2,s)} \qquad (14)$$

where $B_{(1/2,s)}$ is the measured full-width at half-maximum of the profiles plotted in s-space.

This analysis was originally developed by Warren and Bodenstein [29,30] and others [31] for a different crystallite size distribution which resulted in a constant of 1.77 in the above equations. The difference between these equations and the Scherrer equation is the 1.84 constant and the use of the full-width at half-maximum instead of the integral breadth. Both $L_{hk}$ equations are equivalent, but Equation 14 is used because it is a simpler calculation.

The $\chi = 70°$ scan was used because of the Bragg scan's truncation [32] in oriented systems at $\chi = 90°$, and because at this tilt any three-dimensional crystalline peaks can also be observed. The (11) reflection, near $78°$ $2\theta$, was chosen over the (10) reflection, near $42.5°$ $2\theta$, because any interference from the three-dimensional reflections of (11,2) or (10,1), respectively, is more easily separated in the (11) reflection case.

Figure 20 shows a Bragg scan of P-100 fiber in the (10,0) and (10,1) region for $\chi = 70°$ and $\chi = 90°$ which clearly shows the absence of the 3-D reflection in the meridional scan while being clearly visible in the off-axis scan. Figure 21 of the (11,0) and (11,2) region for P-100 shows the same results. One can see that resolving the two peaks is easier in the latter scan which is why the (11) reflection was chosen for the $L_a$ calculations.

Several difficulties still exist for using the values of $L_a$ calculated in this manner. Firstly, the fiber tilt away from $\chi = 90°$ means that the crystal size being measured is not parallel to the fiber axis but at an angle of 20° to it. However the truncation of the intensity at higher $2\theta$ (as the tilt angle approaches $\chi = 90°$) would invalidate the Ruland equation for the estimation of crystallite sizes.

Secondly, the presence of three-dimensional crystals [as evidenced by (hk,$\ell$) reflections] observed as the fiber modulus increases should change the size analysis from the Ruland
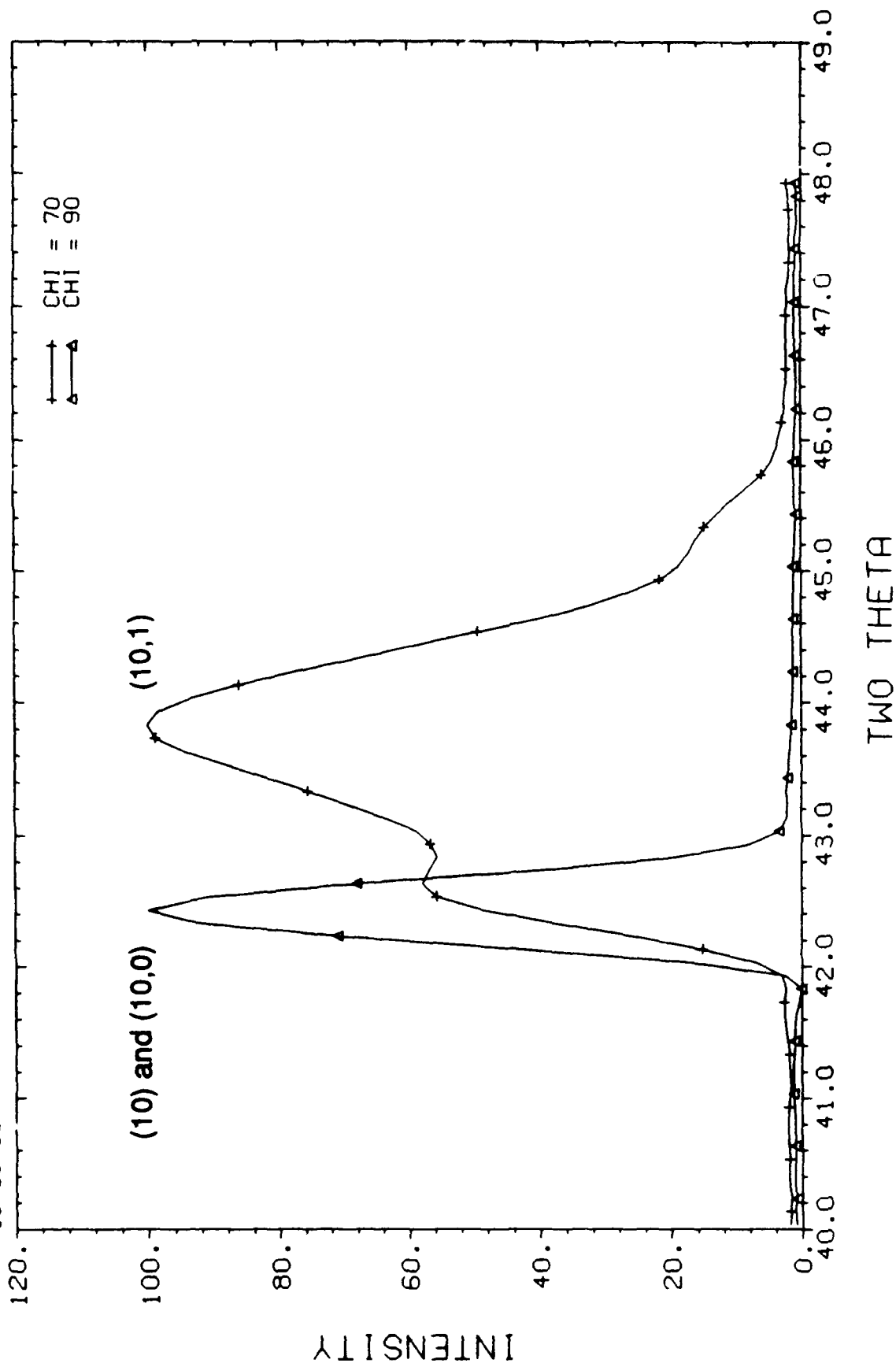
Figure 20. Bragg Scans of P-100 Fiber Bundle at $\chi=70°$ and $\chi=90°$ [(10,0) and (10,1) Region].
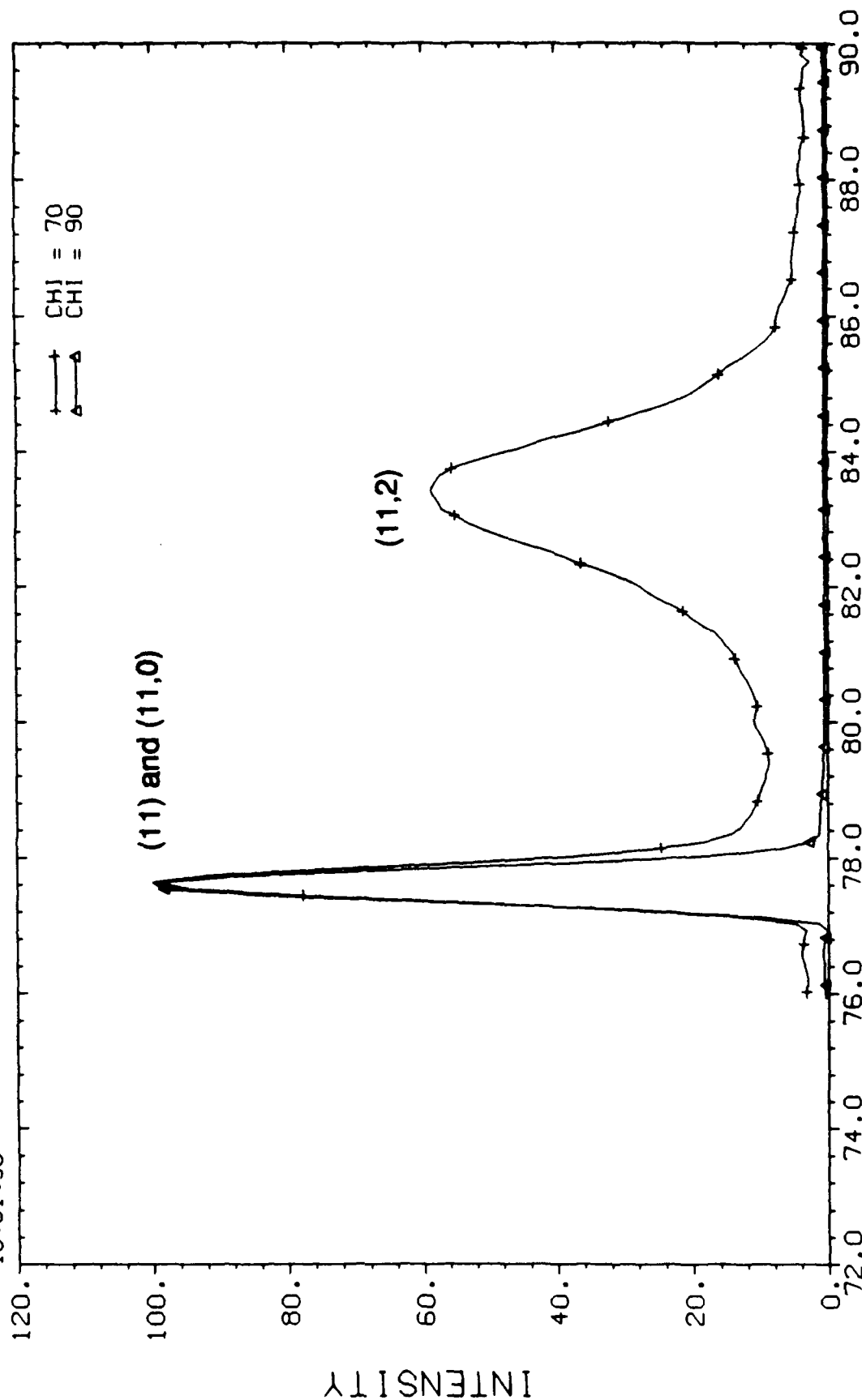
Figure 21.  Bragg Scans of P-100 Fiber Bundle at χ=70° and χ=90° [(11,0) and (11,2) Region].

equation to the standard Scherrer equation [23]. Even in the highest modulus fibers, the typical asymmetric two-dimensional nature of the reflections observed indicates a mixture of 2-D and 3-D crystals contributing to the intensity. Since there is no way the author or others [33] are aware of estimating the relative fraction of 2-D and 3-D crystals or how that knowledge could be used to produce a better equation for the crystallite size, the Ruland equation has been used on all samples to produce $L_a$ size estimates. The absolute values of these $L_a$ estimates are probably incorrect, but the size trends probably are correct.

Appendix B has a complete list of the calculated $L_a$ values for all of the azimuthal angles and reflections for which the Bragg scans were obtained. The trends of sizes are all the same regardless of the method used to calculate the $L_a$ values.

Another possible avenue for obtaining a weighted average of the $L_a$ in fibers is to use fibers which have been ground up such that all possible orientations of the fiber are examined in the x-ray experiment at the same time. As can be seen from the data in Appendix B, the breadths of the reflections in ground fibers tend to be dominated by the smallest crystals (broadest reflections). Figures 22 and 23 include the same plots as Figures 20 and 21 with the addition of scans taken of P-100 which had been ground into a powder. The ground fiber scans are clearly more difficult to analyze, being broader than the fiber bundle scans.

This method does solve the problem of fiber orientation except that now it is an average $L_a$ and not the value parallel to the fiber. It also does not change the second problem above of mixed 2-D and 3-D crystals. In addition the problem of equatorial reflections interfering with the profiles of the (hk) reflections becomes a real and unwanted burden (see Figure 23). While many researchers use ground fiber scans to estimate $L_a$, this method was not considered viable for our work.

## 2.6    THREE-DIMENSIONAL CRYSTALLINITY

The appearance of the 3-D crystalline reflections (10,1) and (11,2) is considered proof of the existence of 3-D graphite crystals. As mentioned in section 2.4, these reflections are not visible in meridional Bragg scans but are visible in scans at $\chi = 70°$. Comparing the $\chi = 70°$ regions of Figures 19 and 21 shows the difference between a fiber with only 2-D crystals (P-25) and one with significant 3-D crystals (P-100). The appearance of the (11,2) reflection and

32
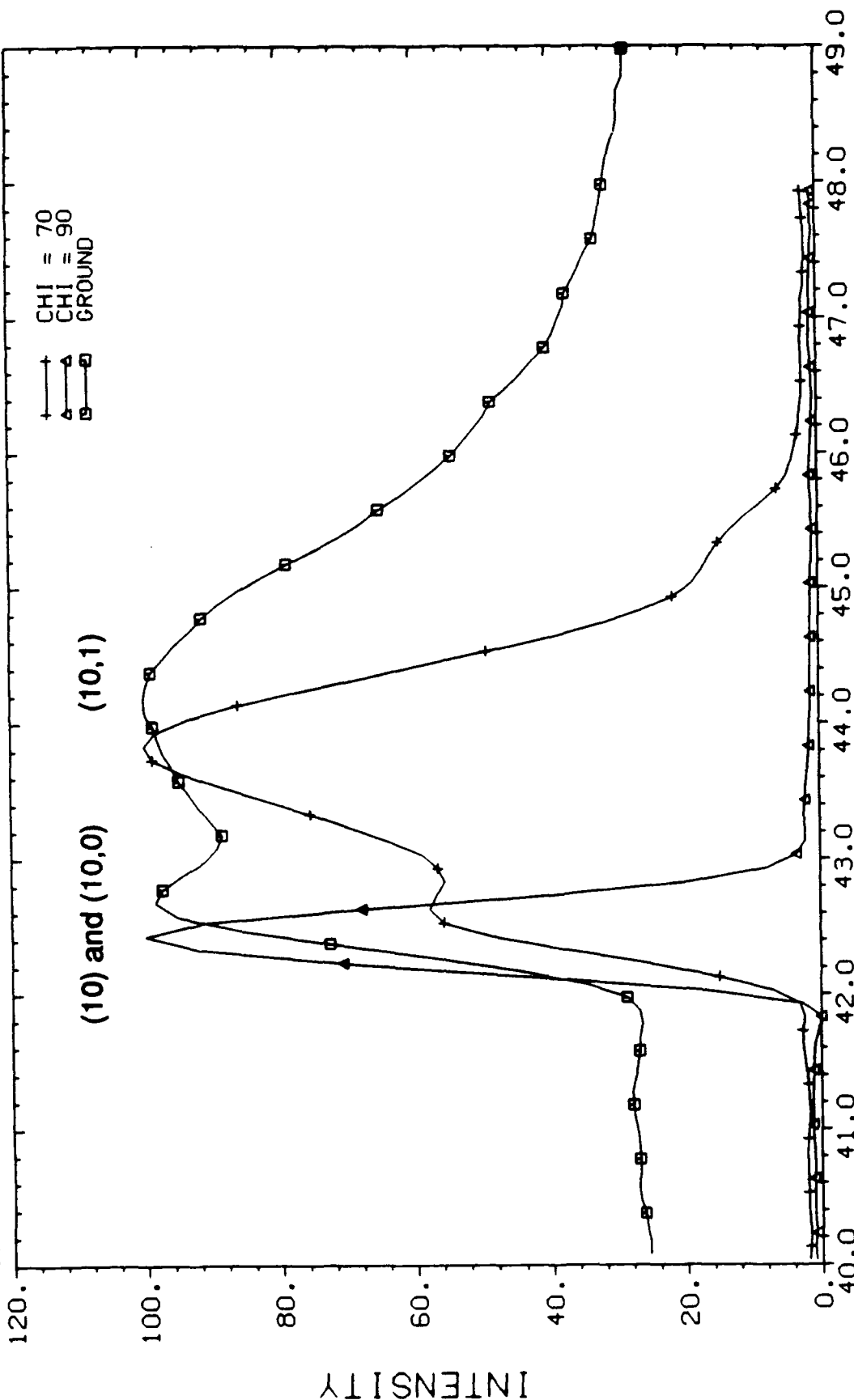
Figure 22.  Bragg Scans of P-100 Fiber; Ground Fiber and Fiber Bundle at $\chi=70°$ and $\chi=90°$ [(10,0) and (10,1) Region].
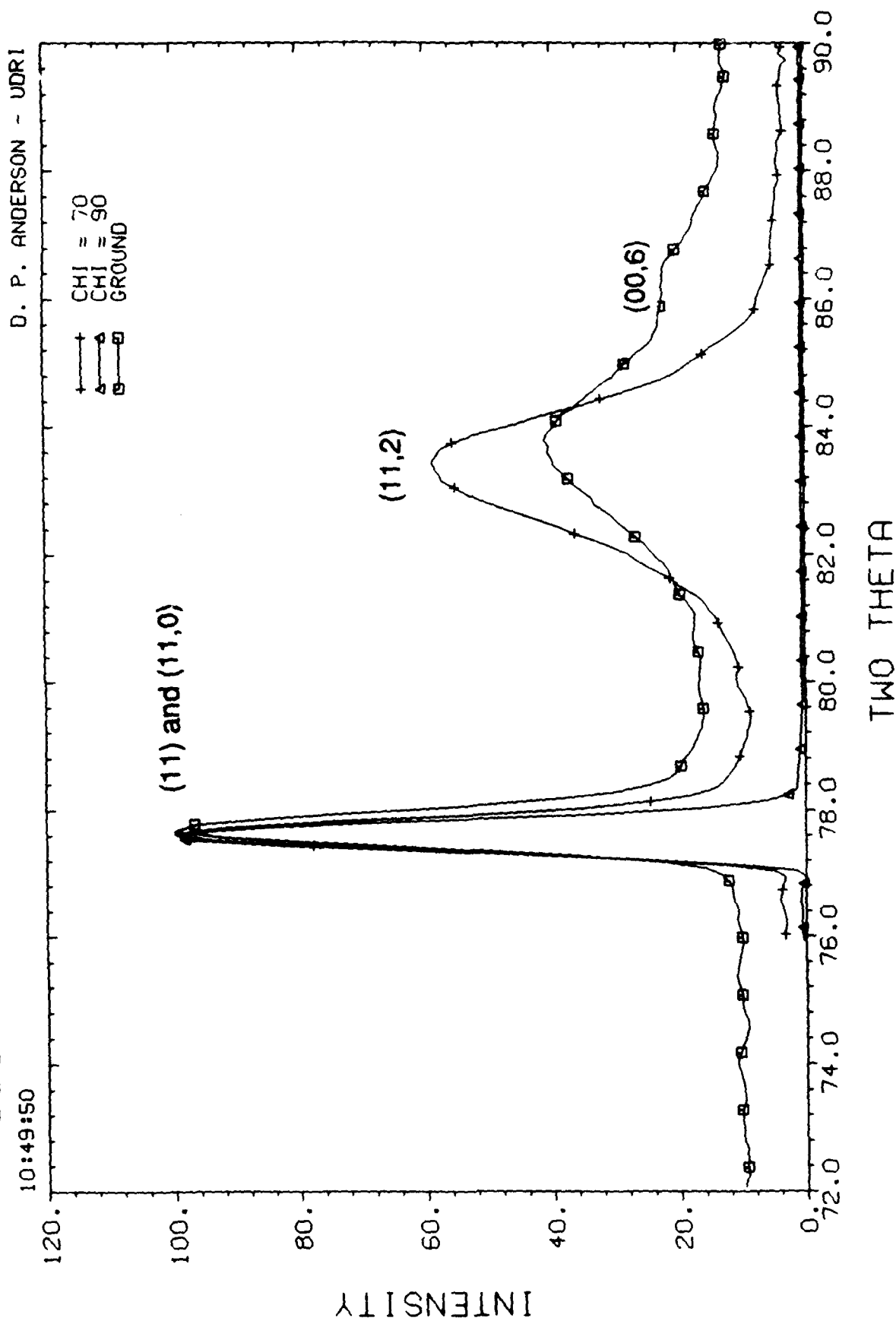
Figure 23. Bragg Scans of P-100 Fiber; Ground Fiber and Fiber Bundle at χ=70° and χ=90° [(11,0) and (11,2) Region].

34

decrease in the peak's asymmetry both are indicative of 3-D crystals in the P-100 fiber. The (11,2) reflection cannot be seen in the meridional scans ($\chi=90°$) in these figures.

Figure 24 shows this same region for the fiber P-75. The presence of 3-D crystals is much less obvious but nonetheless visible. Figure 25 shows the scan for P-55 fiber which only hints at a 3-D peak.
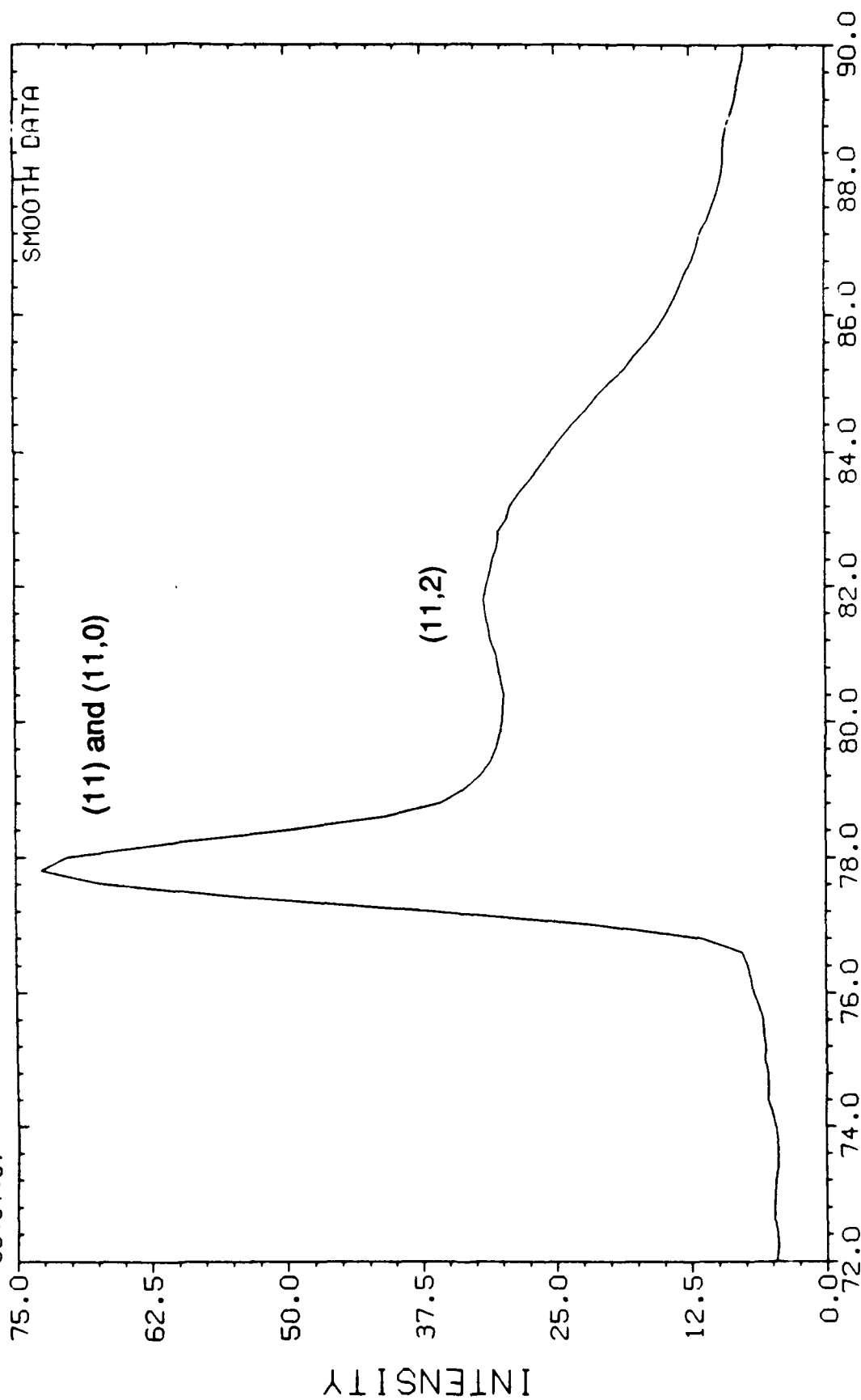
Figure 24. Bragg Scans of P-75 Fiber Bundle at χ=70° [(11), (11,0), and (11,2) Region].

Figure 25.  Bragg Scans of P-55 Fiber Bundle at $\chi=70°$ [(11), (11,0), and (11,2) Region].

# 3. RESULTS AND DISCUSSION

## 3.1 FIBER WAXD RESULTS

The results of the equatorial and azimuthal $(00,\ell)$ analyses are given in Table 2. Also listed in that table are the $L_a$ results as discussed in section 2.5. Table 3 gives the qualitative evaluations of the presence of 2-D and 3-D crystals in the fibers.

Many plots of the x-ray results and mechanical data can be made. The focus of this study is on the compressive strength of carbon fibers, but other properties are plotted as well for comparison and illustrative purposes.

One universal correlation clearly visible is in the plot of tensile modulus versus Z (with variation between precursor groups) with increased orientation of the (00,2) reflection (decreased Z) corresponding to an increased TM, a well-known observation (see Figure 26).

A general increase in graphitization and crystallite sizes is also associated with an increase in TM but with more scatter than the orientation as seen in Figure 27. Closer examination of the pitch-based fibers (Figure 28) shows that this general trend is true within a production series, but that significant differences exist in the degree of graphitization for fibers with the same TM. The same correlations can be made for crystallite size as seen for $L_c$ in Figures 29 and 30.

Figure 31 shows very little correlation between TM and void content, although within a production series (see Figure 32) lowering the void content increases the TM.

These results indicate that orientation is the primary structural parameter that governs tensile modulus. Other general and series specific correlations with TM are probably a result of structural changes that occur during similar processing but do not contribute directly to the TM.

Tensile strength correlates less well with the x-ray results than TM. No structural parameter produced a good universal curve or even a good curve for any precursor with TS; however, some correlations within production series can be made. Compare the general plots and pitch-based fiber plots, respectively, for d-spacing (Figures 33 and 34), $Z_{(00,2)}$ (Figures 35 and 36), void content (Figures 37 and 38), and $L_c$ (Figures 39 and 40).

## TABLE 2

### SUMMARY OF X-RAY DIFFRACTION RESULTS

| Fiber | d-spacing (00,2) (nm) | Degree of Graphite $g_p$ | Void Content (%) | Z FW-HM (°) | $L_c$ (00,2) (nm) | $L_a$ (11) (nm) |
|---|---|---|---|---|---|---|
| Pitch-Based | | | | | | |
| P-25 | 0.344 | 0.02 | 13.8 | 31.9 | 2.6 | 4.0 |
| P-55 | 0.342 | 0.20 | 9.7 | 14.1 | 12.4 | 16.4 |
| P-75 | 0.3410 | 0.34 | 8.2 | 11.0 | 14.6 | 17.3 |
| P-100 | 0.3382 | 0.68 | 4.1 | 5.6 | 22.7 | 56.1 |
| P-120 | 0.3376 | 0.74 | 2.9 | 5.6 | 25.1 | 69.8 |
| E-35 | 0.344 | -0.03 | 4.6 | 21.6 | 3.2 | 4.4 |
| E-75 | 0.3424 | 0.19 | 2.4 | 10.9 | 10.3 | 9.9 |
| E-105 | 0.3420 | 0.23 | 2.1 | 7.2 | 13.8 | 14.3 |
| K-135 | 0.3422 | 0.20 | 4.7 | 10.4 | 11.9 | 12.3 |
| Gr P-55 | 0.3423 | 0.20 | 9.7 | NA | 10.7 | NA |
| Gr P-75 | 0.3412 | 0.33 | 8.2 | NA | 11.9 | NA |
| Gr P-100 | 0.3377 | 0.74 | 4.2 | NA | 16.5 | NA |
| PAN-Based | | | | | | |
| T-2    P | 0.344 | 0.02 | na | 35.5 | 1.4 | na |
| T-300 | 0.342 | 0.23 | 19.3 | 35.1 | 1.5 | 3.7 |
| AS-4 | 0.342 | 0.24 | 18.8 | 36.8 | 1.8 | 3.5 |
| T-40 | 0.343 | 0.08 | 19.4 | 30.2 | 1.8 | 3.4 |
| G40-700 | 0.343 | 0.08 | 19.8 | 29.1 | 2.4 | 4.9 |
| IM6    P | 0.344 | 0.05 | 21.6 | 33.7 | 1.8 | na |
| G45-700 | 0.344 | -0.01 | na | 26.7 | 2.3 | 4.5 |
| IM8 | 0.3431 | 0.11 | 18.5 | na | 1.9 | 4.1 |
| HMS    P | 0.3422 | 0.20 | 17.4 | 19.7 | 5.6 | na |
| M40J | 0.3427 | 0.15 | 20.0 | 21.4 | 3.6 | 7.0 |
| T-50   P | 0.3423 | 0.20 | 18.3 | 16.4 | 5.3 | 8.9 |
| GY-70 | 0.3396 | 0.51 | 12.2 | 9.6 | 14.1 | 25.2 |
| M60J | 0.3411 | 0.34 | 12.7 | 9.9 | 7.8 | 13.5 |
| Rayon-Based | | | | | | |
| WCA | 0.343 | 0.14 | na | na | 2.4 | 6.1 |
| T-75 | 0.3403 | 0.44 | 19.2 | 8.7 | 8.4 | 17.2 |

P    - indicates measurements taken with the Picker diffractometer
(all other measurements used the Huber diffractometer)
Gr    - indicates ground fibers samples
na    - values not available
NA    - values not applicable or valid

TABLE 3

SUMMARY OF CARBON FIBER 2-D AND 3-D CRYSTAL CONTENT

| Fiber | 2-D Crystals Only | 3-D Crystals | |
|---|---|---|---|
| | | Suspected | Definite |
| **Pitch-Based** | | | |
| P-25 | X | - | - |
| P-55 | - | X | - |
| P-75 | - | - | X |
| P-100 | - | - | X |
| P-120 | - | - | X |
| E-35 | X | - | - |
| E-75 | - | - | X |
| E-105 | - | - | X |
| K-135 | - | - | X |
| **PAN-Based** | | | |
| T-2 | X | - | - |
| T-300 | X | - | - |
| AS-4 | X | - | - |
| T-40 | X | - | - |
| G40-700 | X | - | - |
| IM6 | X | - | - |
| G45-700 | X | - | - |
| IM8 | X | - | - |
| HMS | X | - | - |
| M40J | X | - | - |
| T-50 | - | X | - |
| GY-70 | - | - | X |
| M60J | - | - | X |
| **Rayon-Based** | | | |
| WCA | X | - | - |
| T-75 | - | - | X |

40
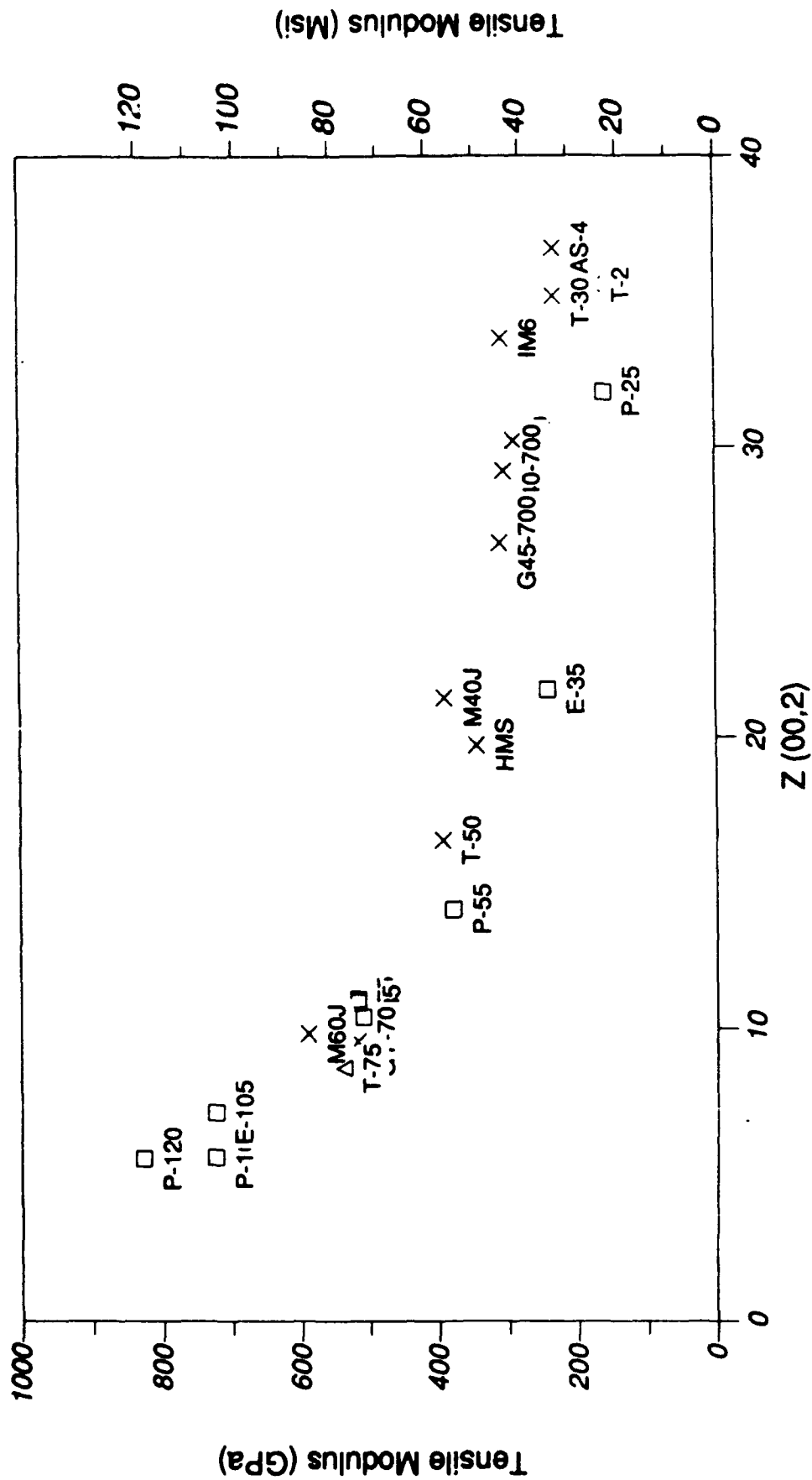
Figure 26. Tensile Modulus versus Z(00,2) for Carbon Fibers.
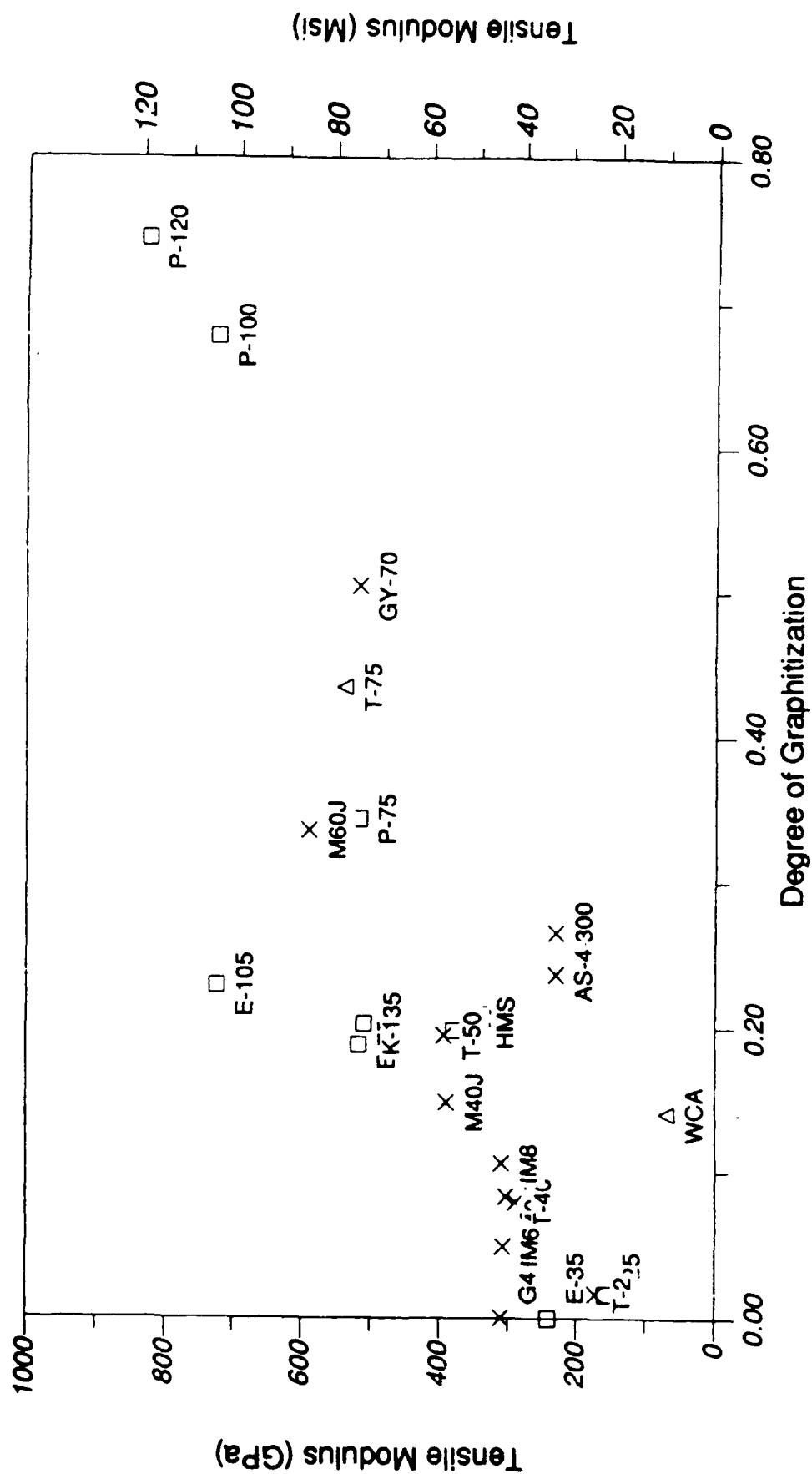
Figure 27. Tensile Modulus versus Degree of Graphitization for Carbon Fibers.
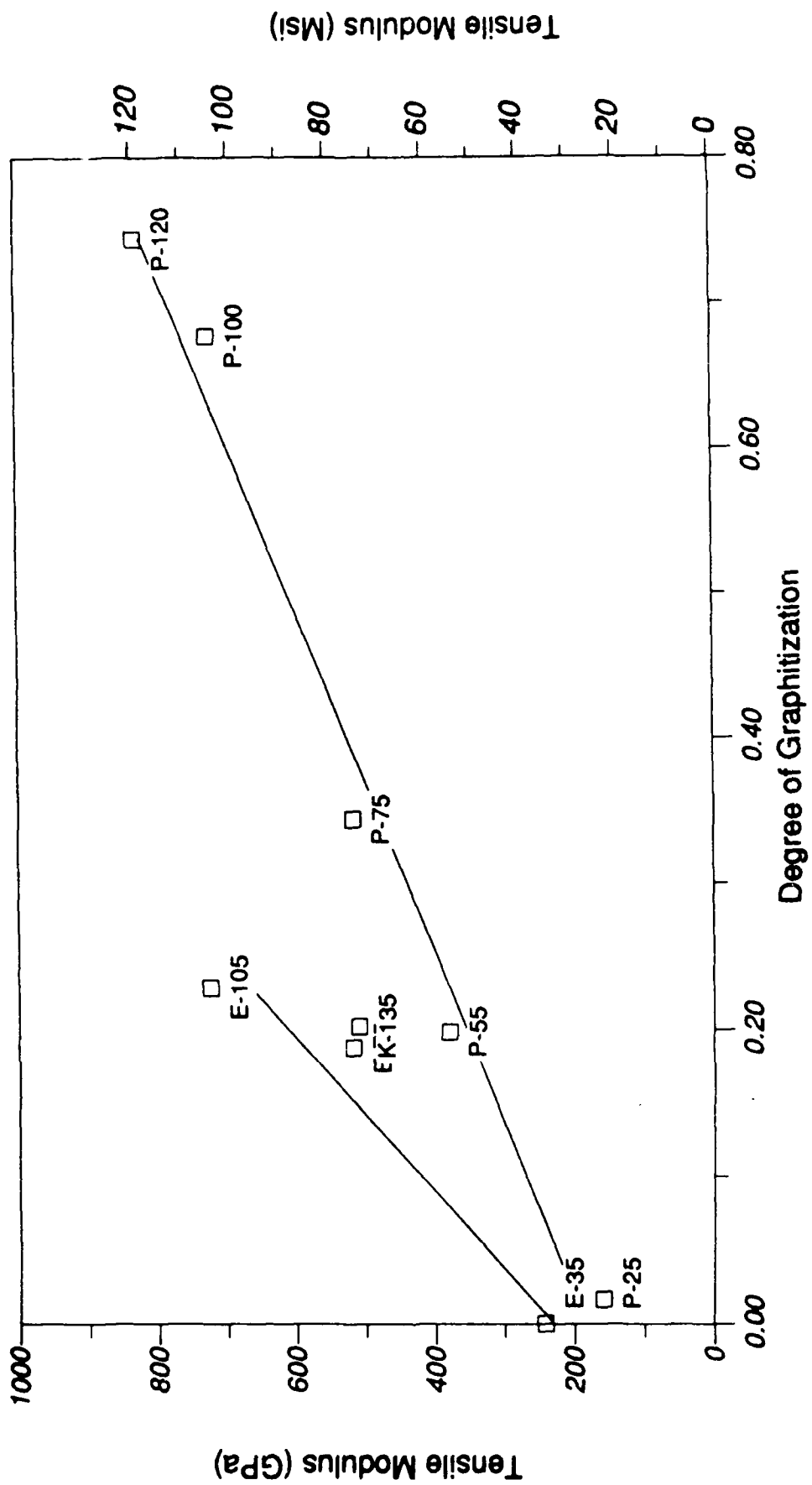
Figure 28. Tensile Modulus versus Degree of Graphitization for Pitch-Based Carbon Fibers.

43
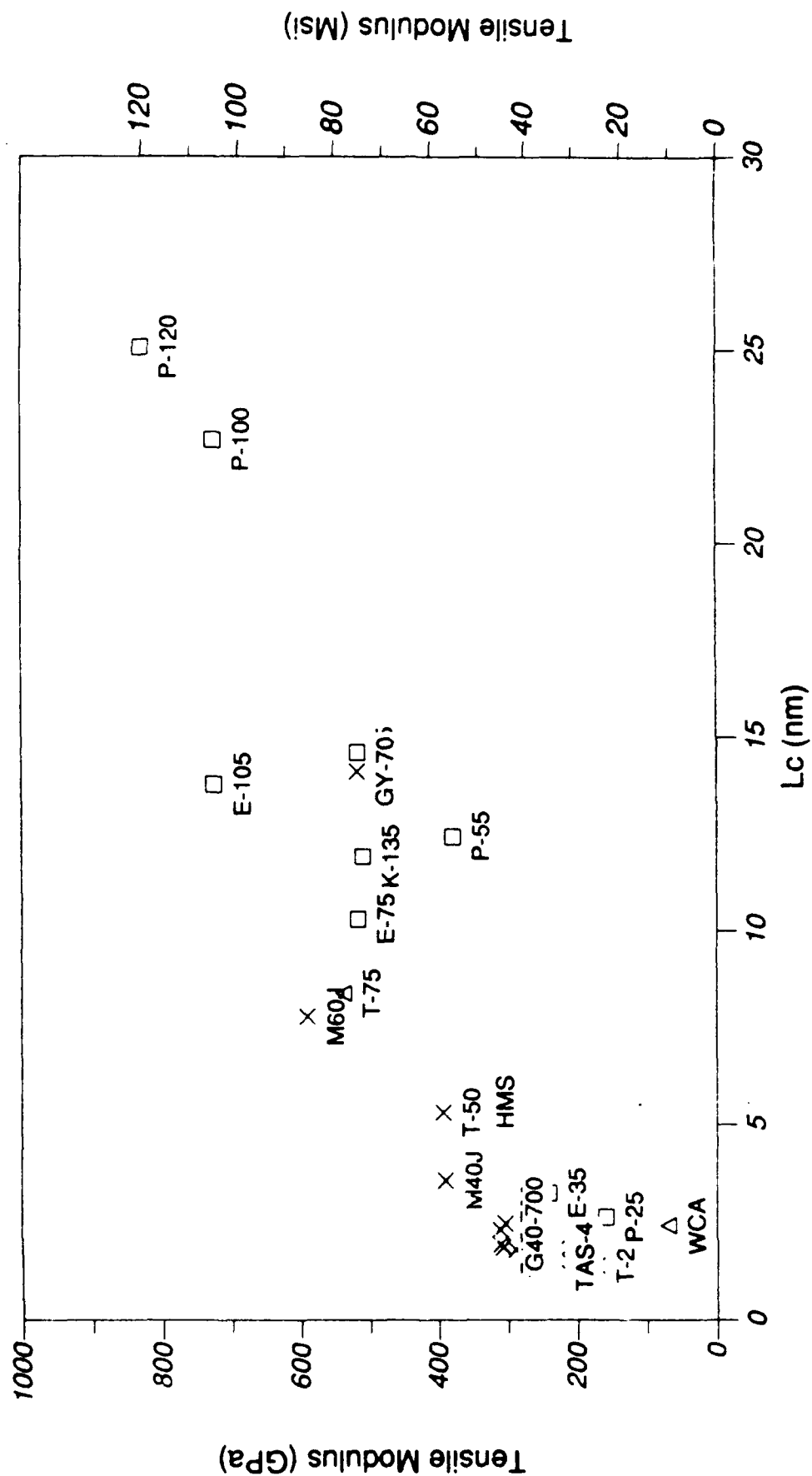
Figure 29. Tensile Modulus versus $L_c$ for Carbon Fibers.
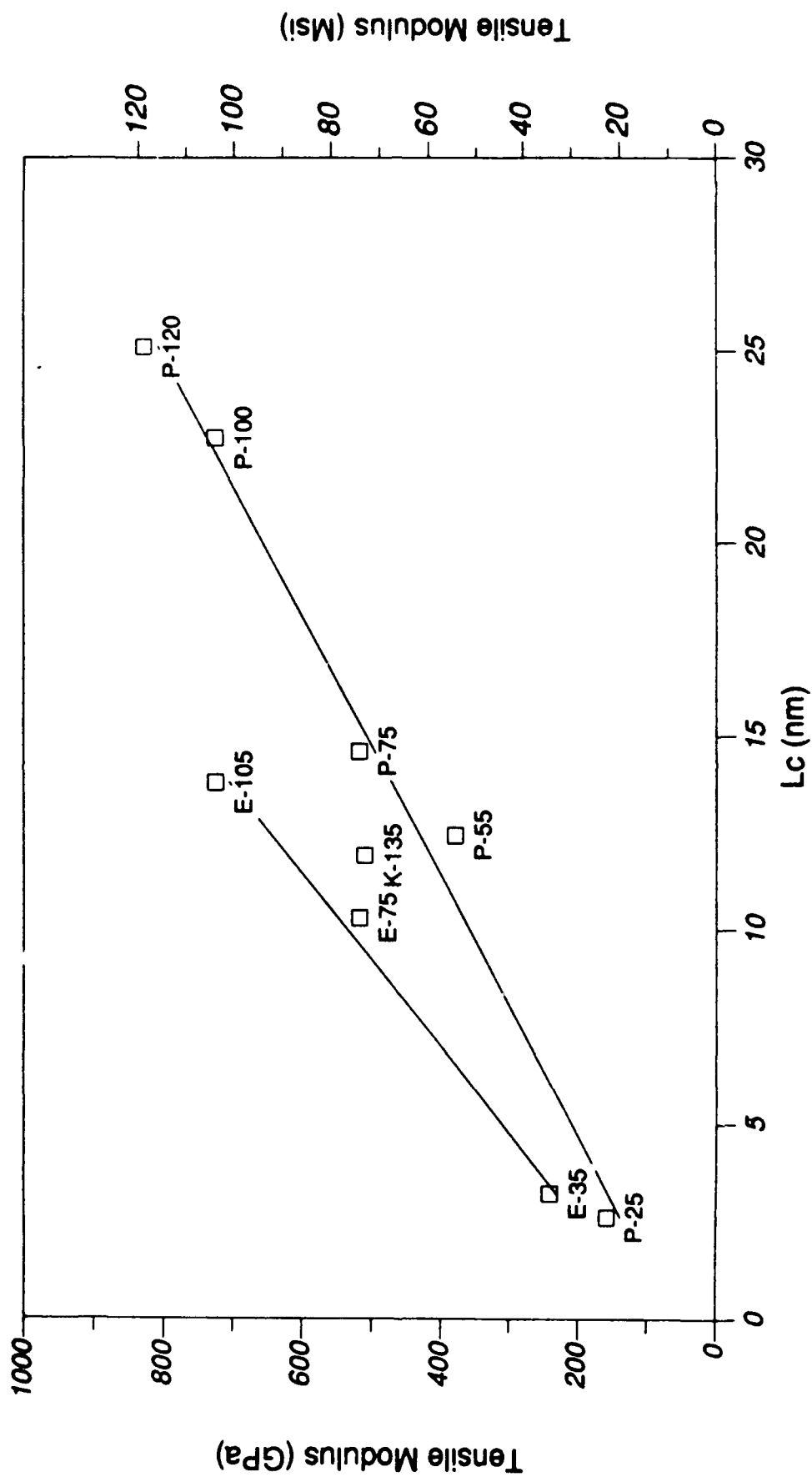
Figure 30. Tensile Modulus versus L$_C$ for Pitch-Based Carbon Fibers.
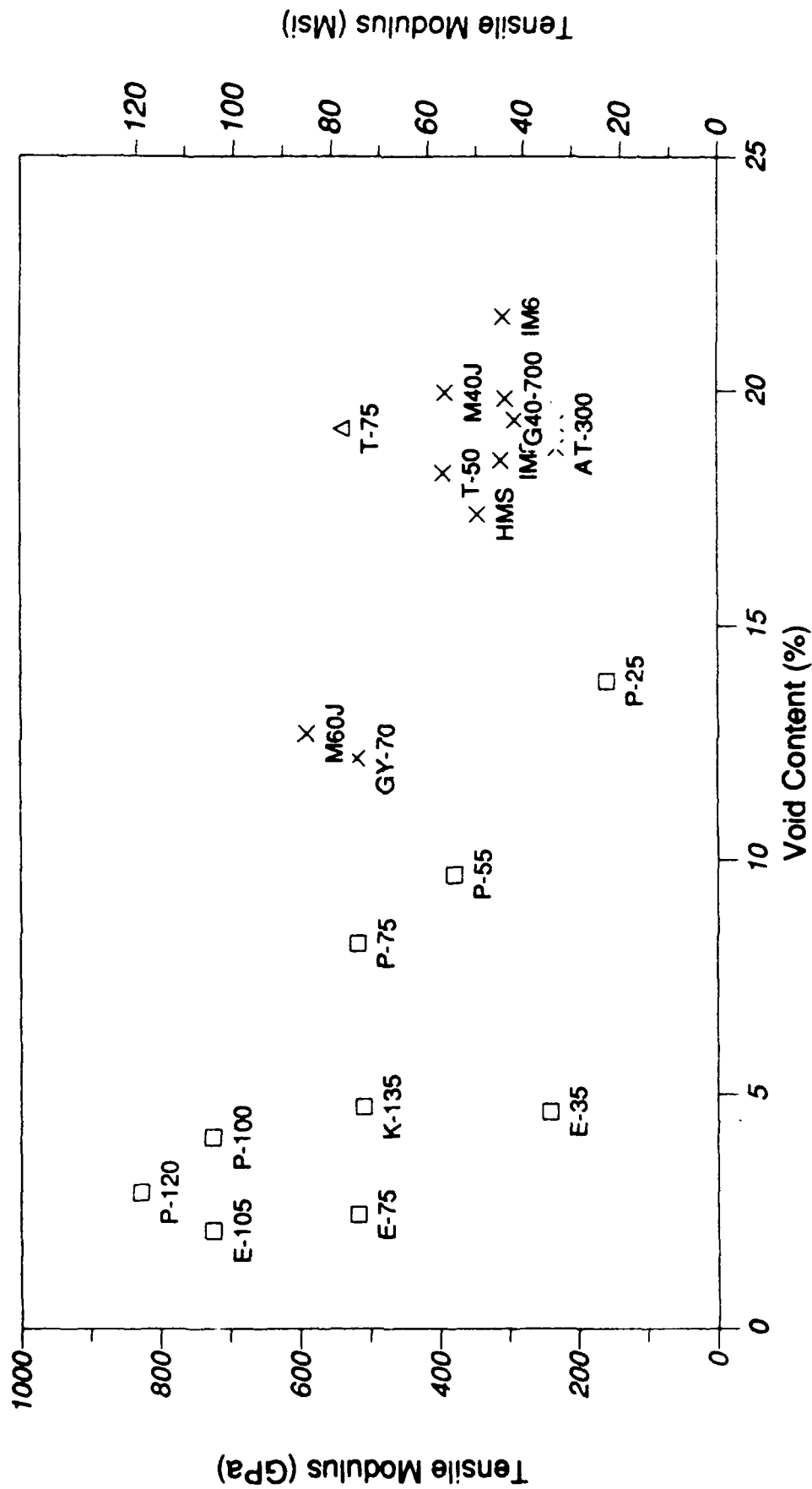
Figure 31. Tensile Modulus versus Calculated Void Content for Carbon Fibers.

46
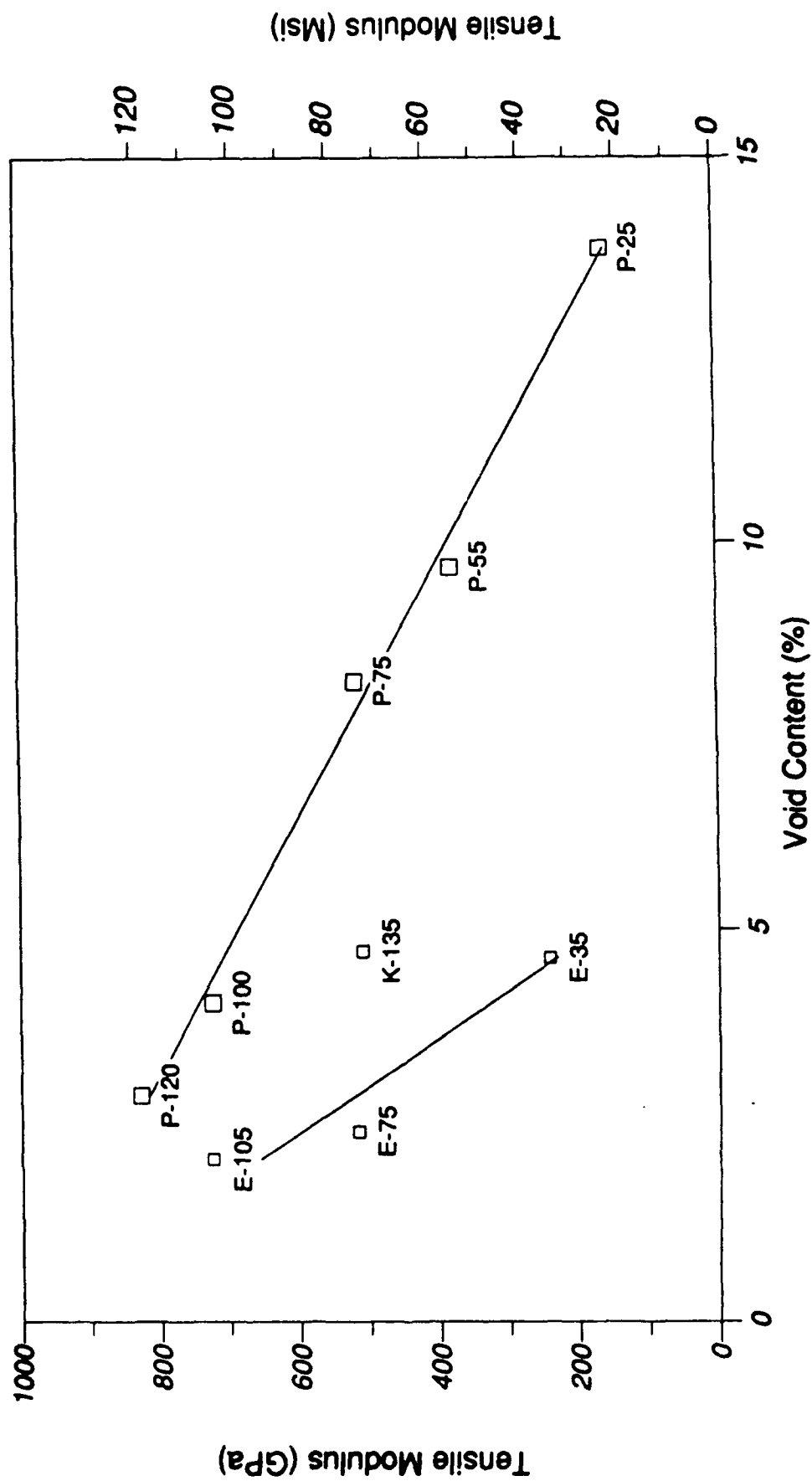
Figure 32. Tensile Modulus versus Calculated Void Content for Pitch-Based Carbon Fibers.
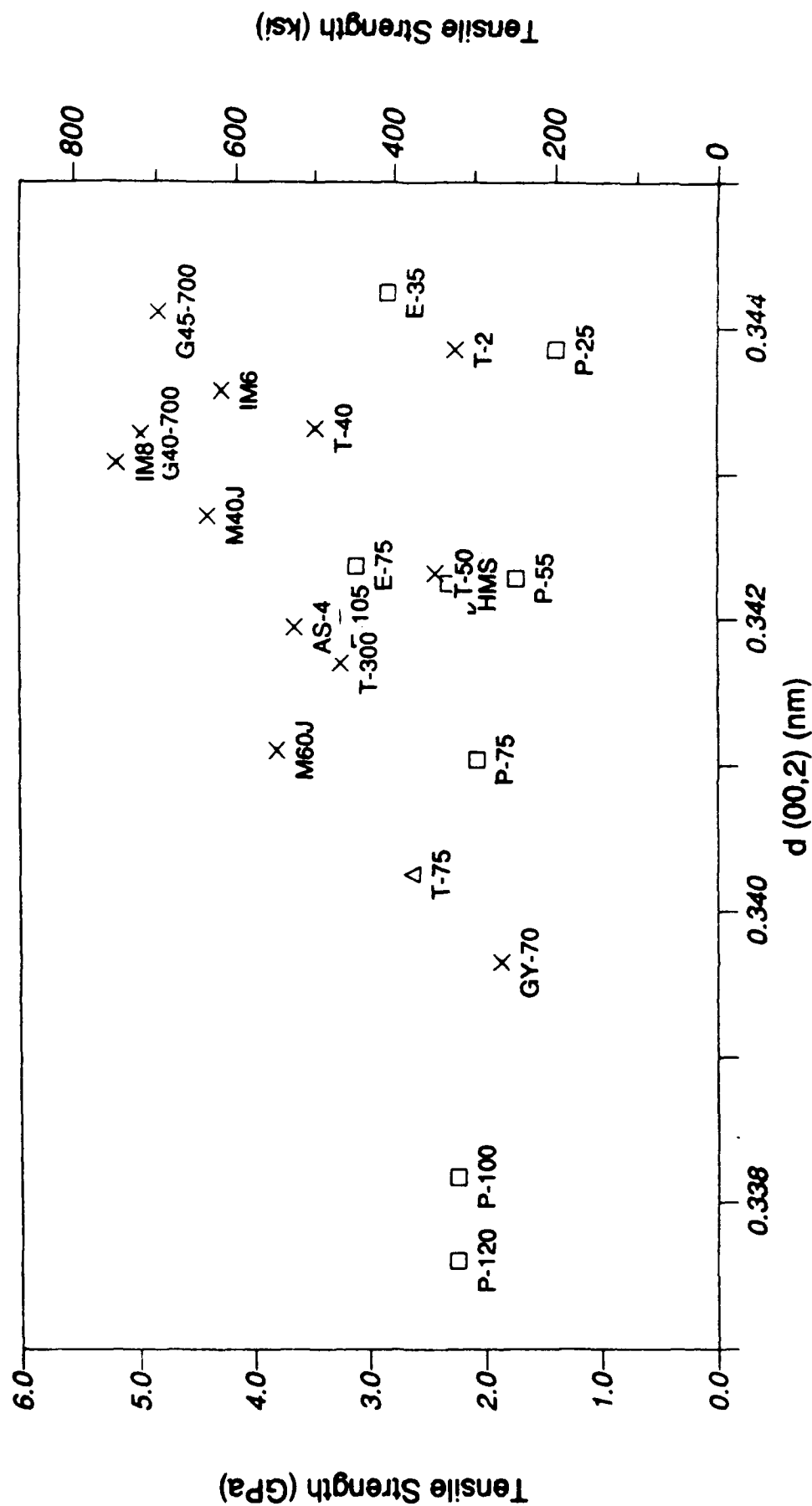
Figure 33. Tensile Strength versus $d_{(00,2)}$ Spacing for Carbon Fibers.
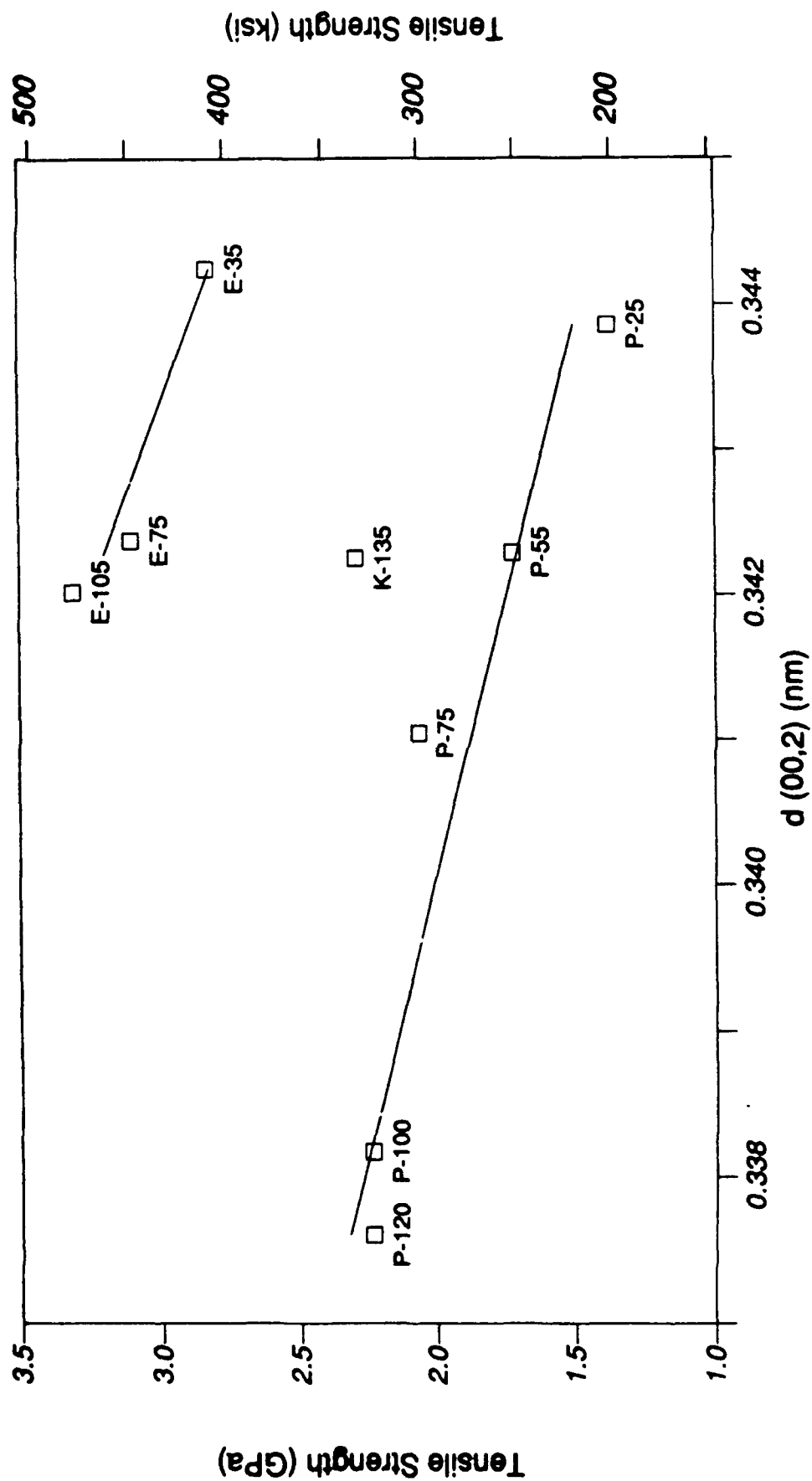
Figure 34. Tensile Strength versus d$_{(00,2)}$ Spacing for Pitch-Based Carbon Fibers.
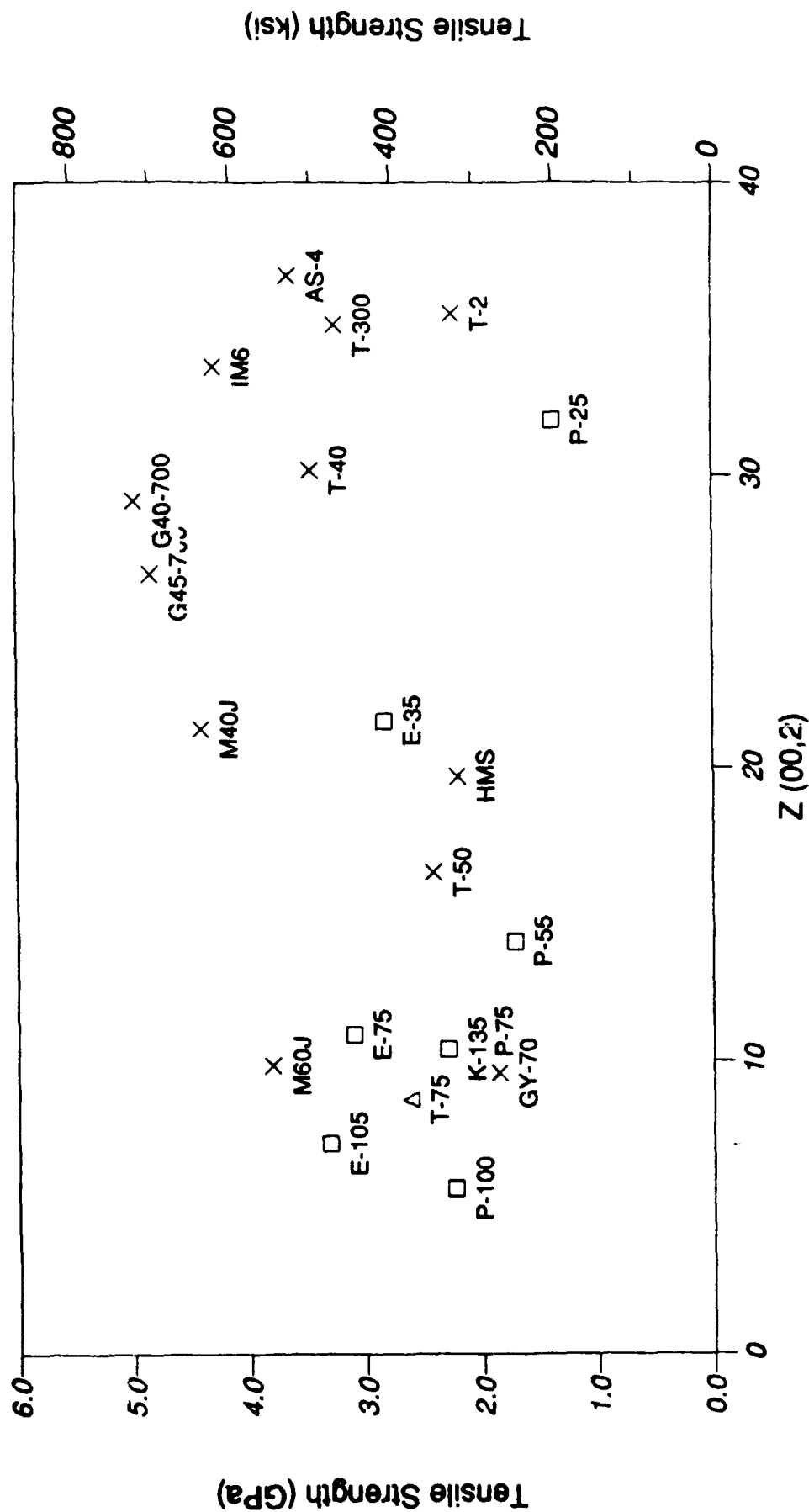
Figure 35. Tensile Strength versus $Z_{(00,2)}$ for Carbon Fibers.
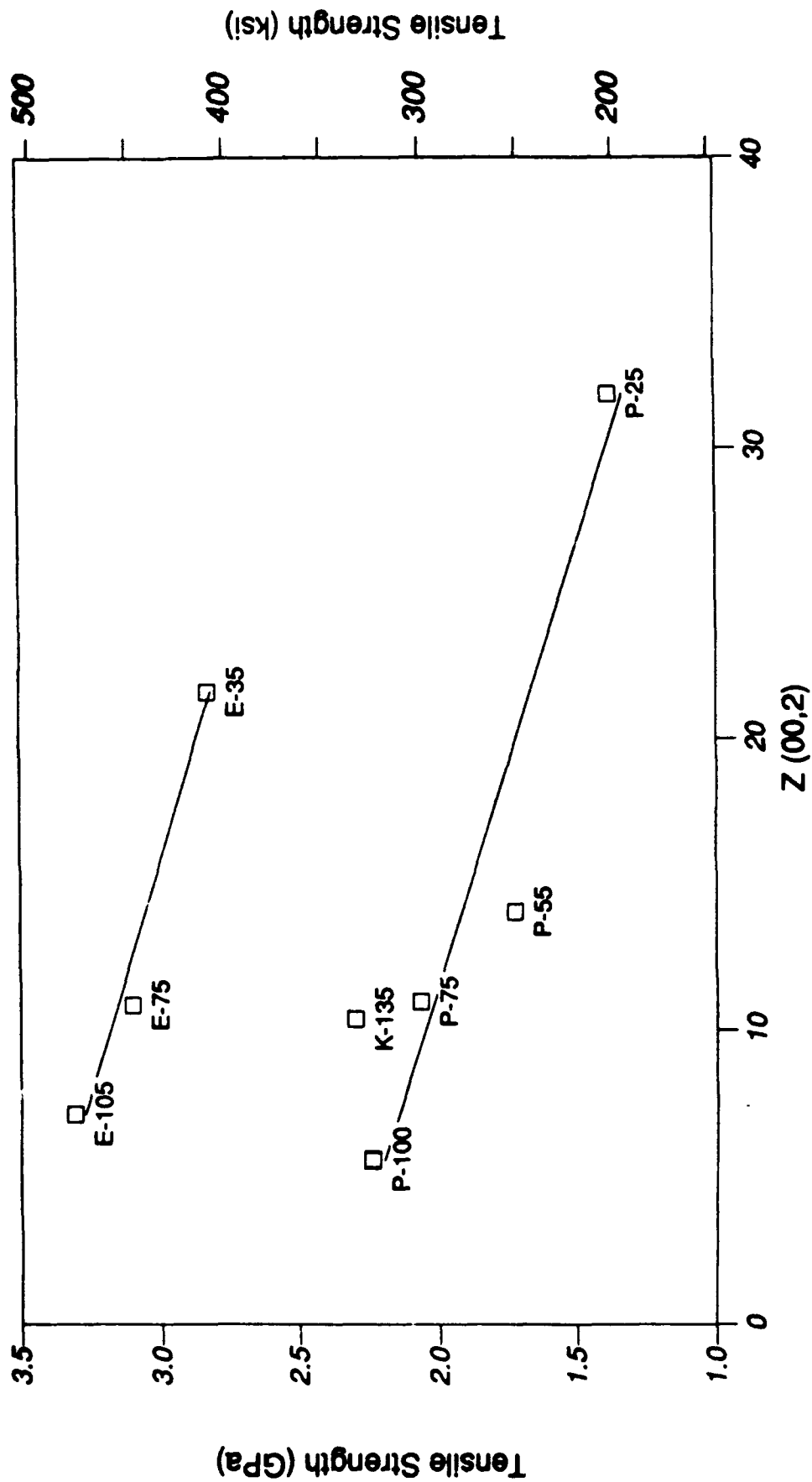
Figure 36.  Tensile Strength versus $Z_{(00,2)}$ for Pitch-Based Carbon Fibers.
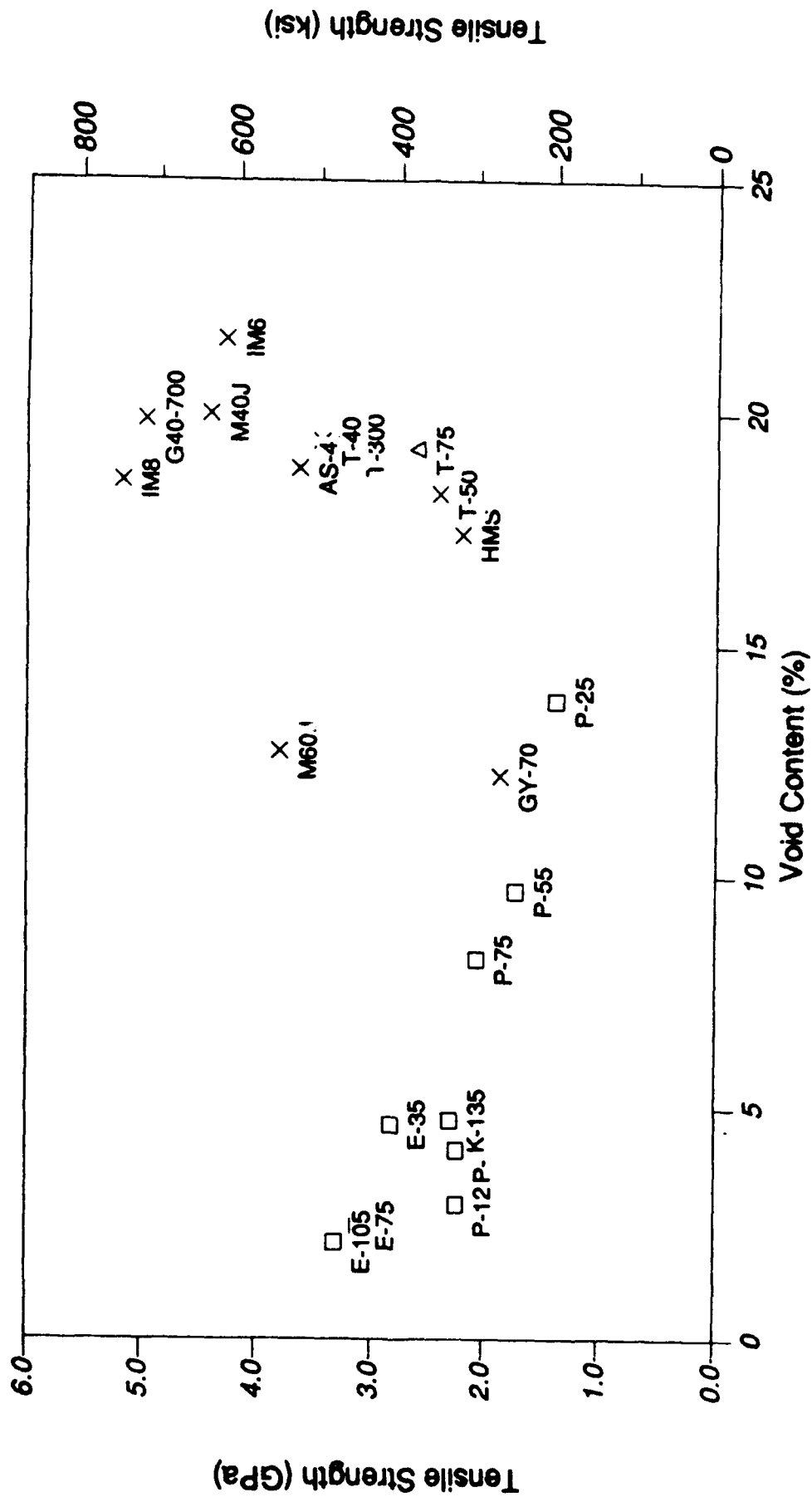
Figure 37. Tensile Strength versus Calculated Void Content for Carbon Fibers.
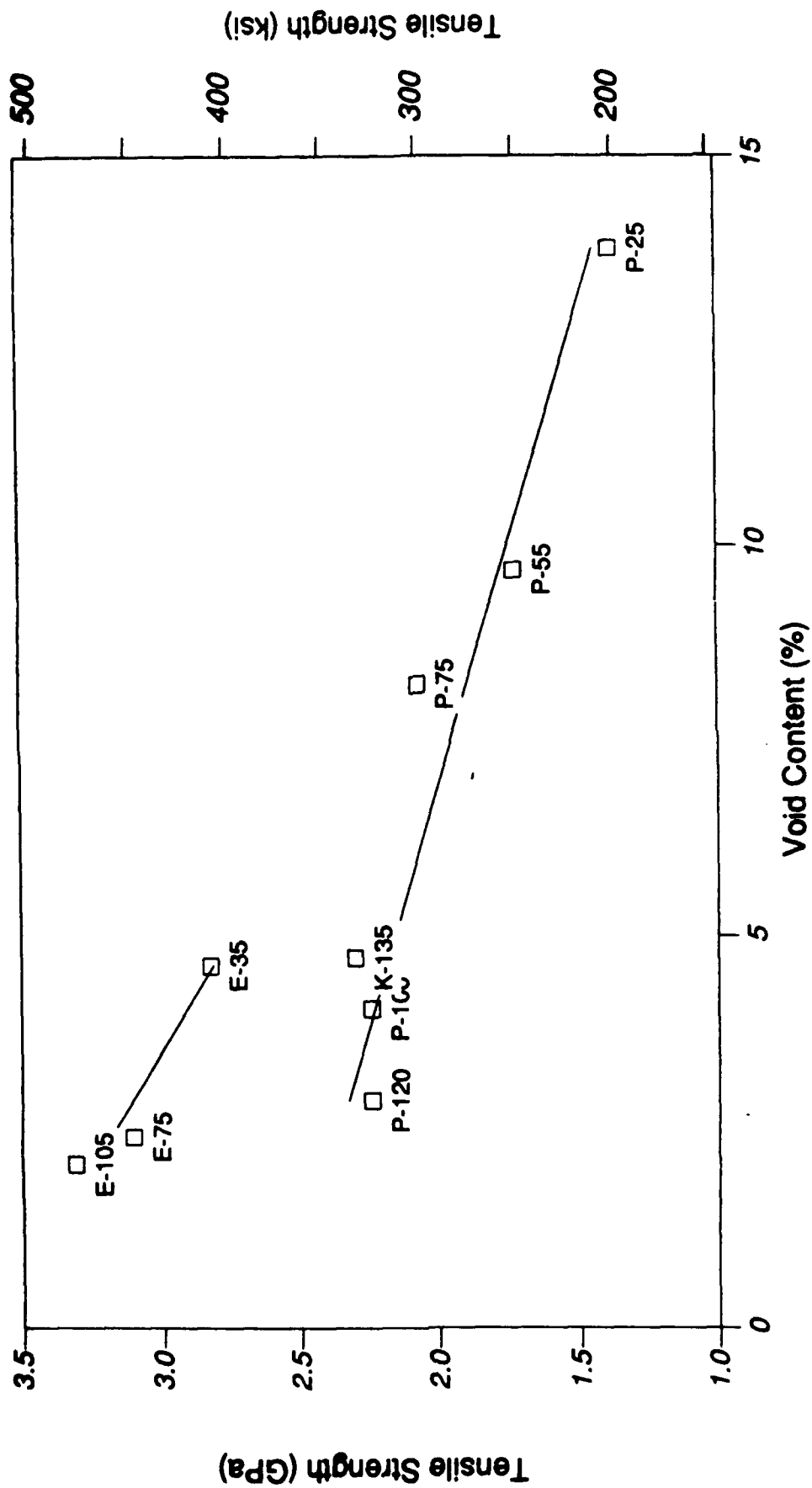
Figure 38. Tensile Strength versus Calculated Void Content for Pitch-Based Carbon Fibers.
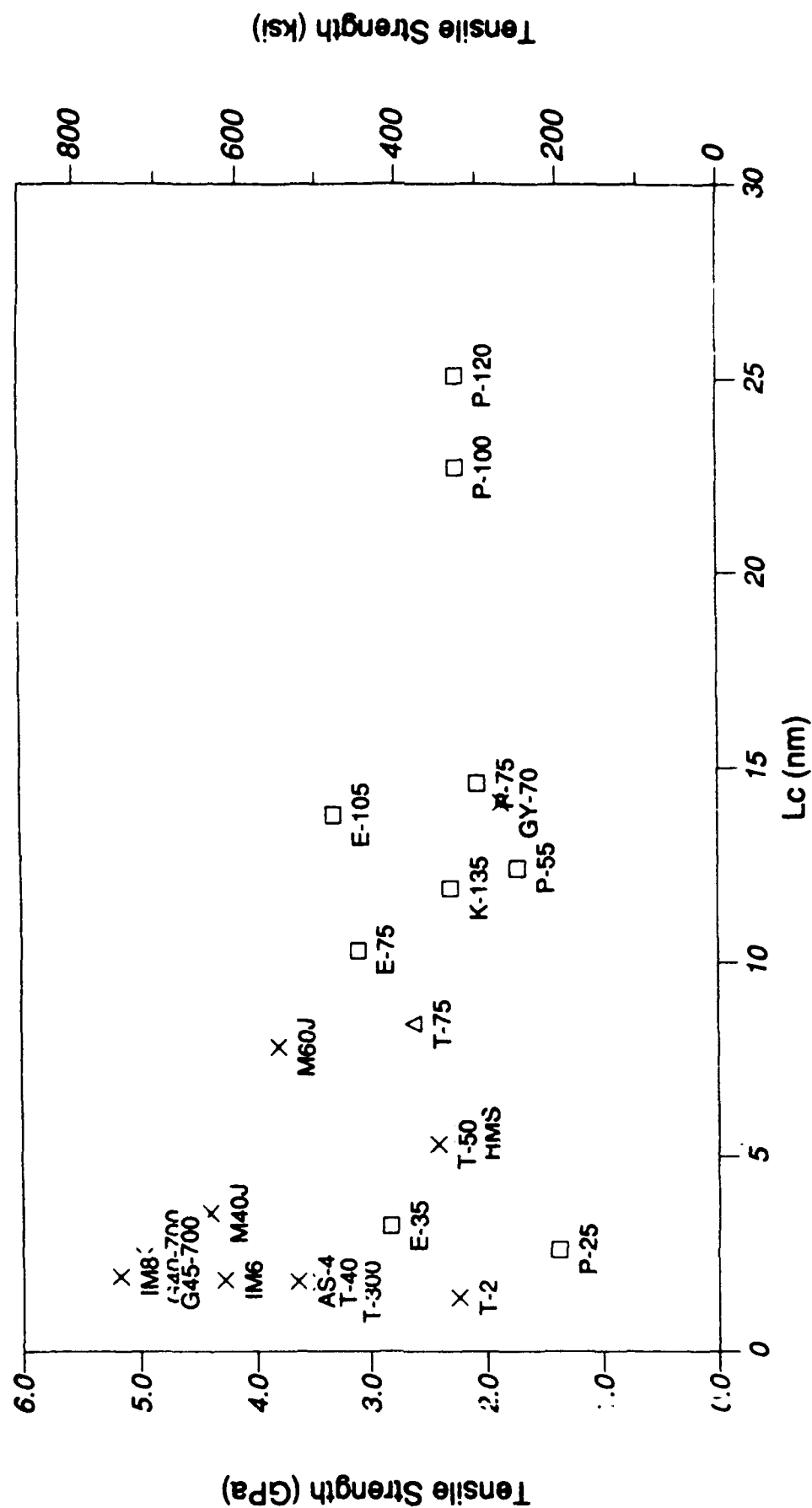
Figure 39. Tensile Strength versus $L_c$ for Carbon Fibers.

54
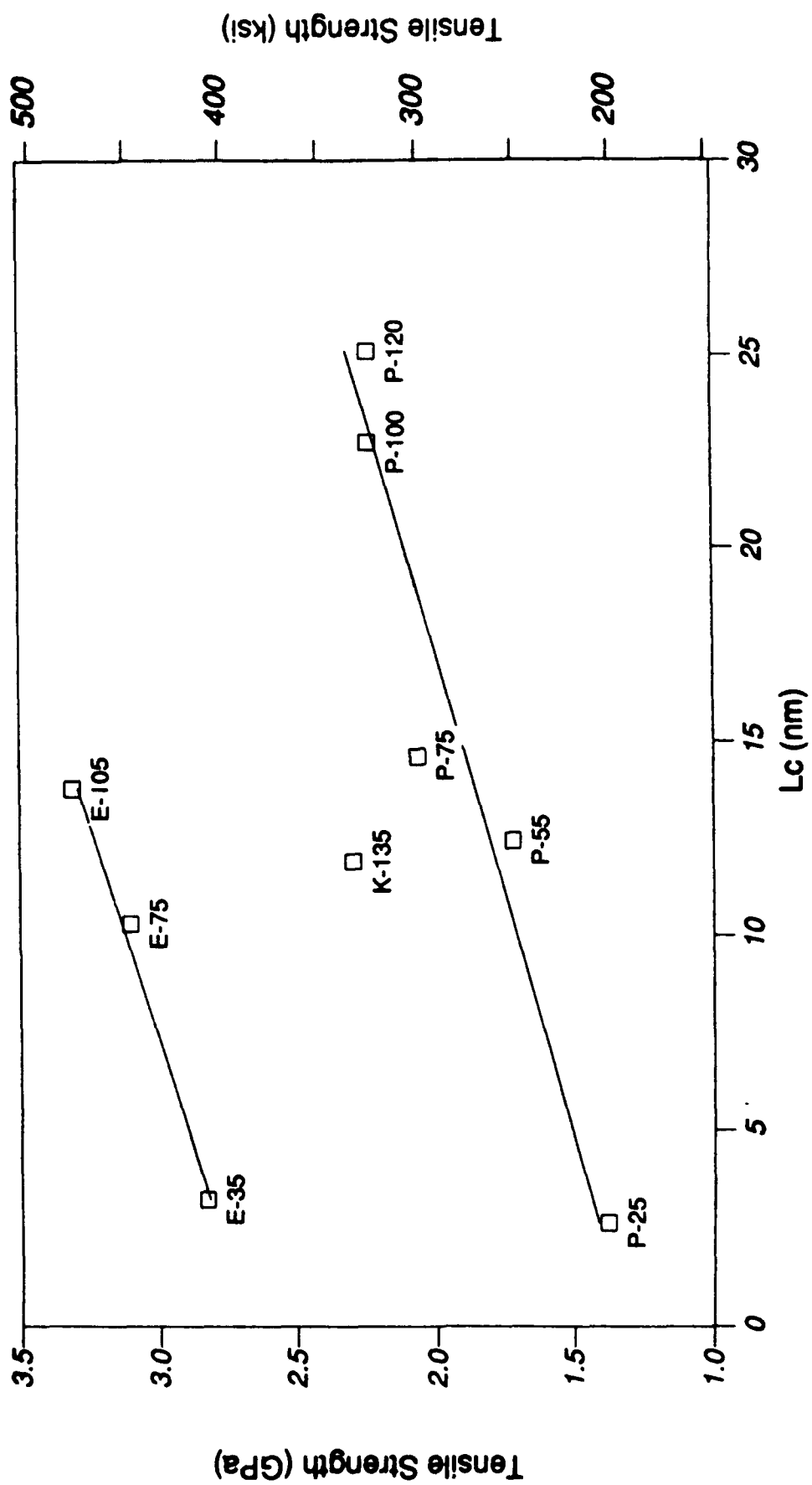
Figure 40. Tensile Strength versus $L_c$ for Pitch-Based Carbon Fibers.

The CS decreases as the degree of graphitization increases (or $d_{(00,2)}$ decreases; see Figure 41) in pitch-based carbon fibers, but for PAN-based fibers there is significantly greater scatter.

The void content of fibers when calculated from the d-spacing and fiber density had shown [3] a universal curve of decreasing CS with decreasing void content. The current data (see Figure 42) is not as uniform; additional fibers fall above and below the original curve. The DuPont E-series, Dialead K-135, and Toray M60J which fall above the old curve all represent more recently developed fibers. The rayon-based T-75 which falls below this curve is an older fiber and probably represents much older manufacturing technology as well as a different precursor material.

Examining the pitch-based fibers more closely (see Figure 43), the fibers in each series fall near a straight line of lower CS as the TM increases in the series. The line of each series also has a different slope. The lower void content of the newer E-series fibers for the same TM correspond to a greater CS. Also discernible from this figure is the trend of CS versus void content for fibers with nearly the same tensile modulus. At low TM (E-35 and P-25) and 75 Msi TM (E-75, K-135, and P-75), there appears a slight increase in CS as the void content is decreased; at higher TM (E-105 and P-100) this trend is even more pronounced. This would suggest, contrary to the general correlation, that the compressive strength can be improved by decreasing the void content as the modulus of a fiber was increased by orientation, etc.

A limited study of measured void content by small-angle x-ray scattering [35] found an increase in void content with higher tensile modulus in PAN-based fibers. This contradicts the trends observed in each of the pitch-based fibers series, but the small number of samples and different precursor of that study limit the comparability of results. It may also be that the actual void content contains more factors than those used to calculate the void content in this study.

Compressive strength also appears to correlate well with crystallite size, both $L_c$ and $L_a$ (see Figures 44 and 45). These plots show a gradual decrease in CS with increased crystallite sizes for pitch-based fibers with a much more rapid decrease for the PAN-based fibers. If the pitch-based fibers are examined separately (see Figures 46 and 47), then for the same TM, fibers with smaller crystals have a higher CS.
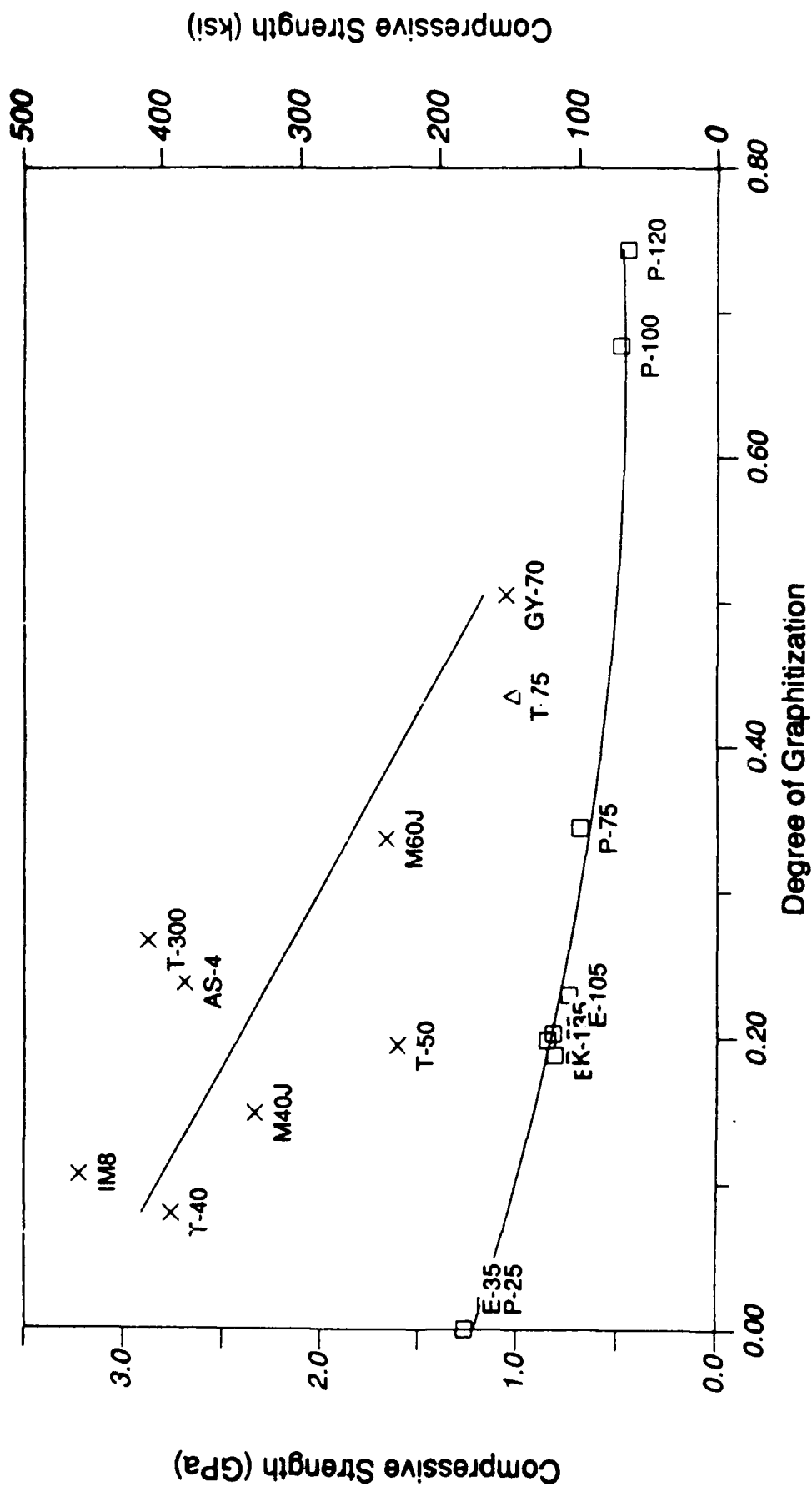
Figure 41. Compressive Strength versus Degree of Graphitization for Carbon Fibers.
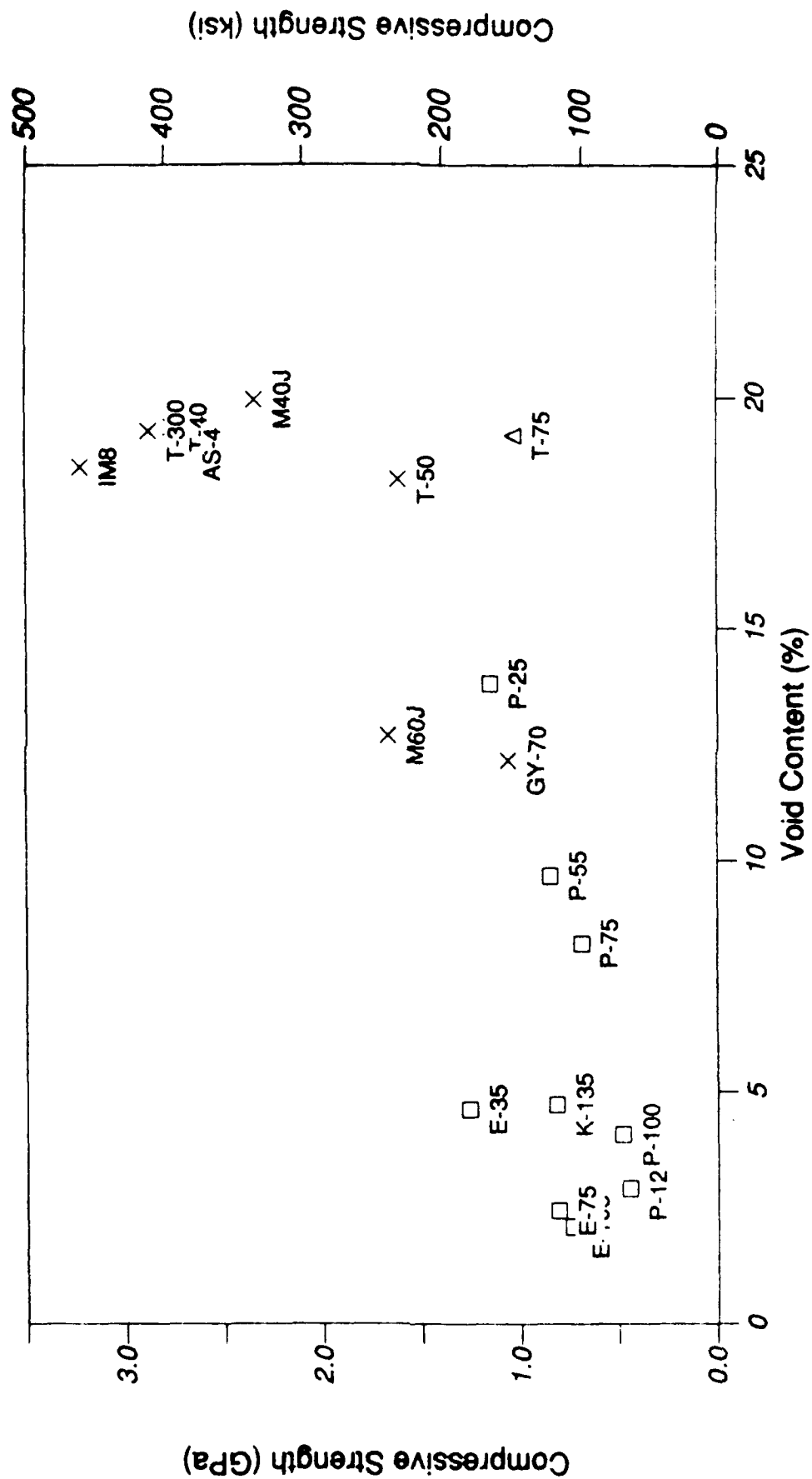
Figure 42.  Compressive Strength versus Calculated Void Content for Carbon Fibers.
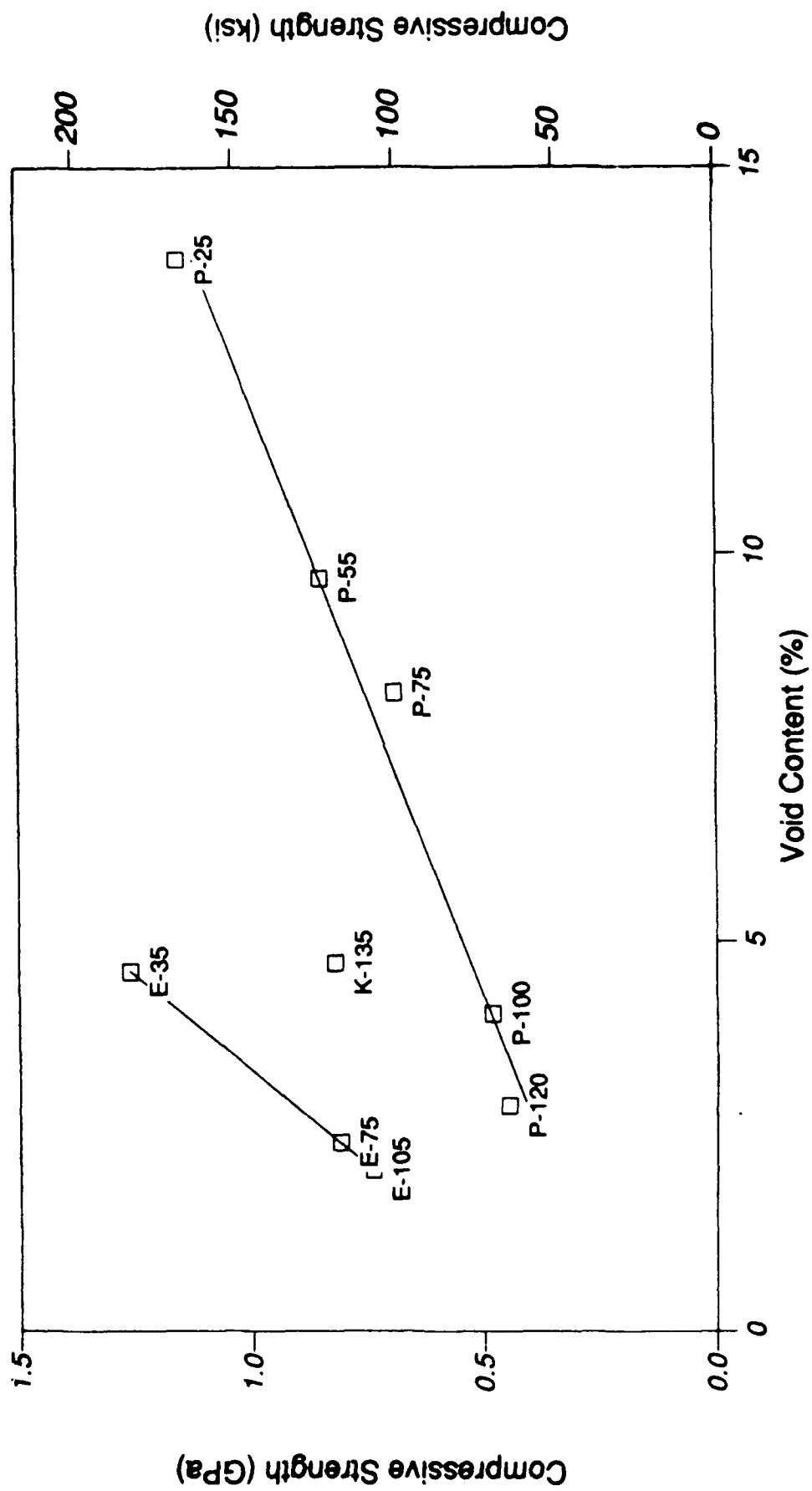
Figure 43. Compressive Strength versus Calculated Void Content for Pitch-Based Carbon Fibers.
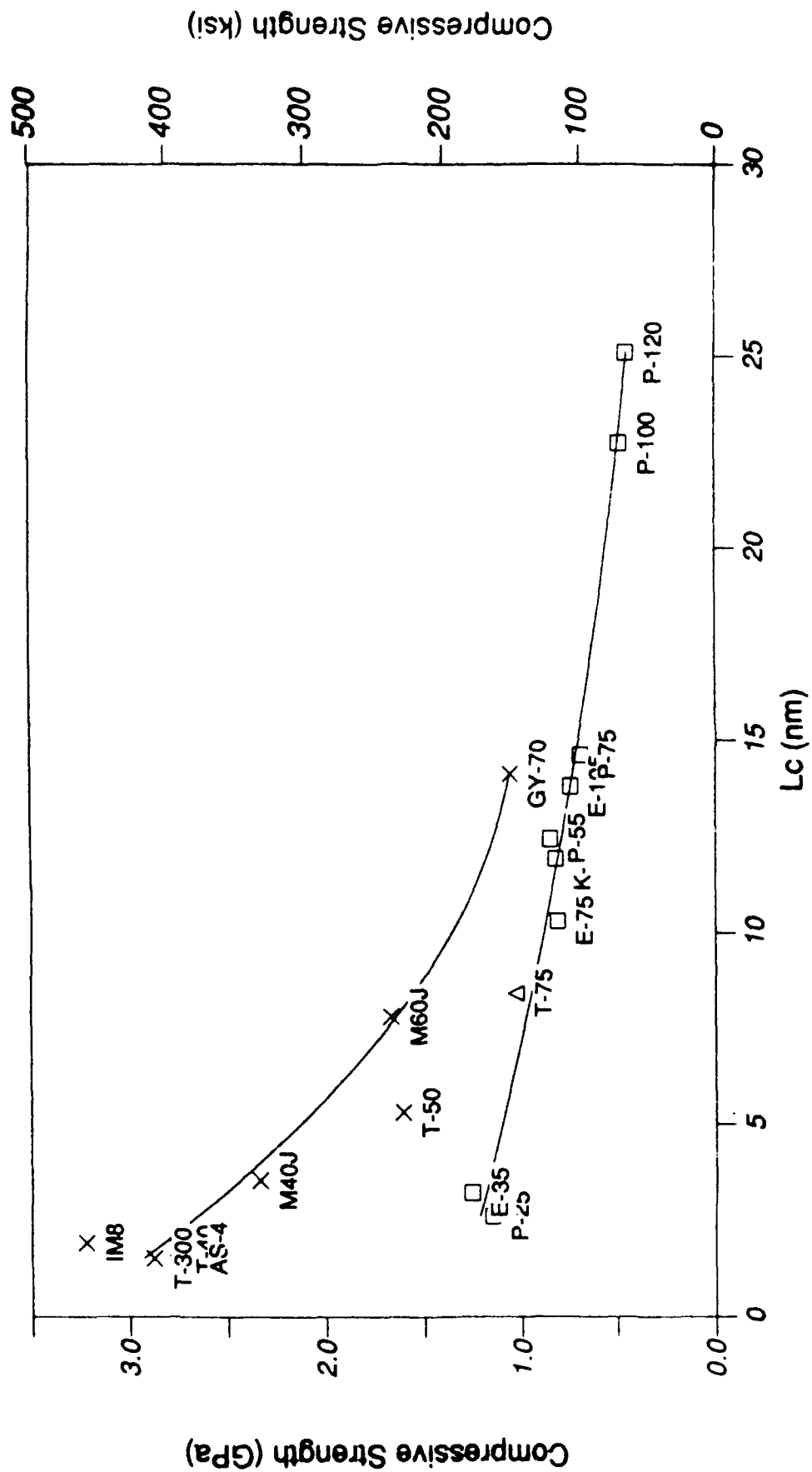
Figure 44.   Compressive Strength versus $L_c$ for Carbon Fibers.
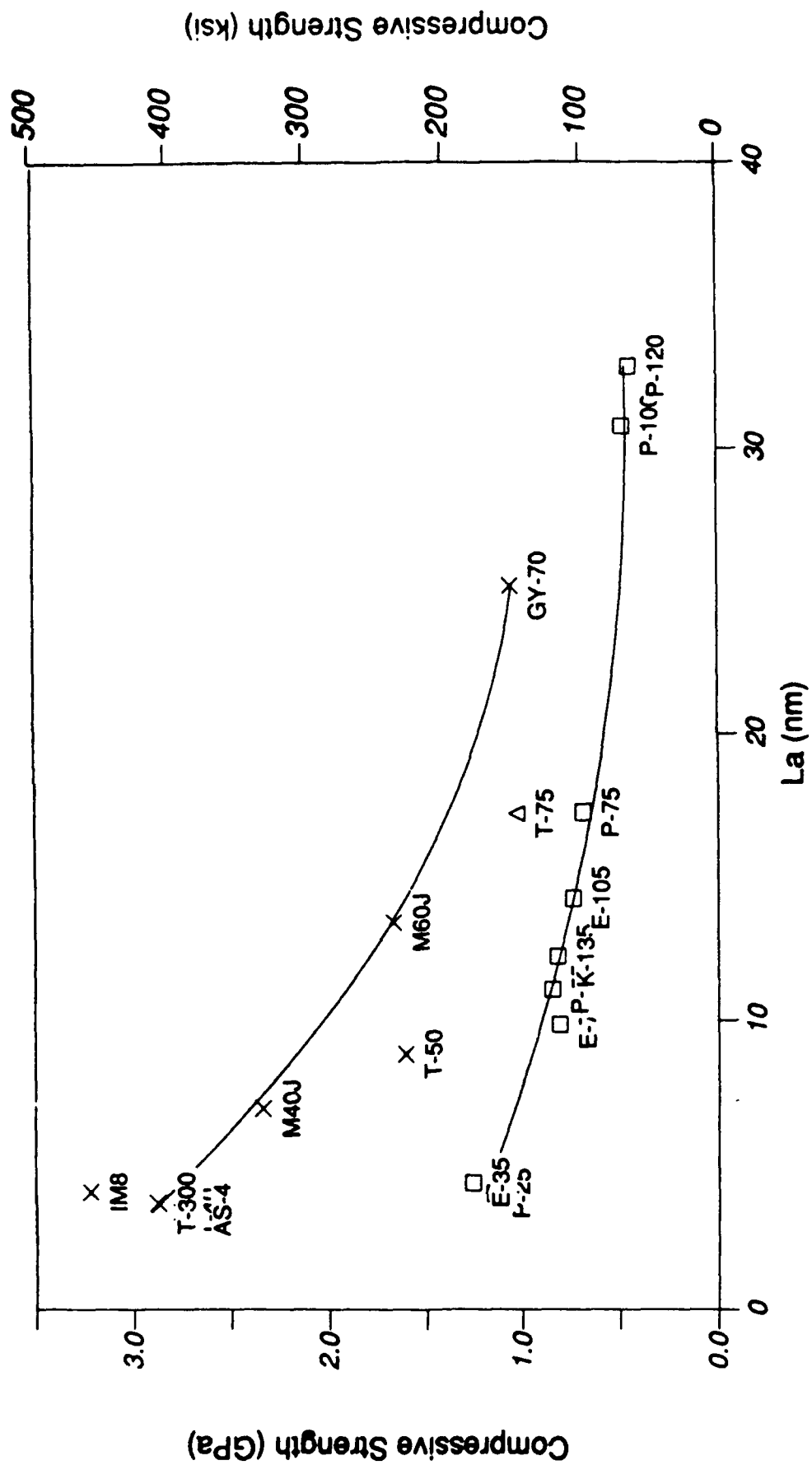
Figure 45. Compressive Strength versus $L_a$ for Carbon Fibers.
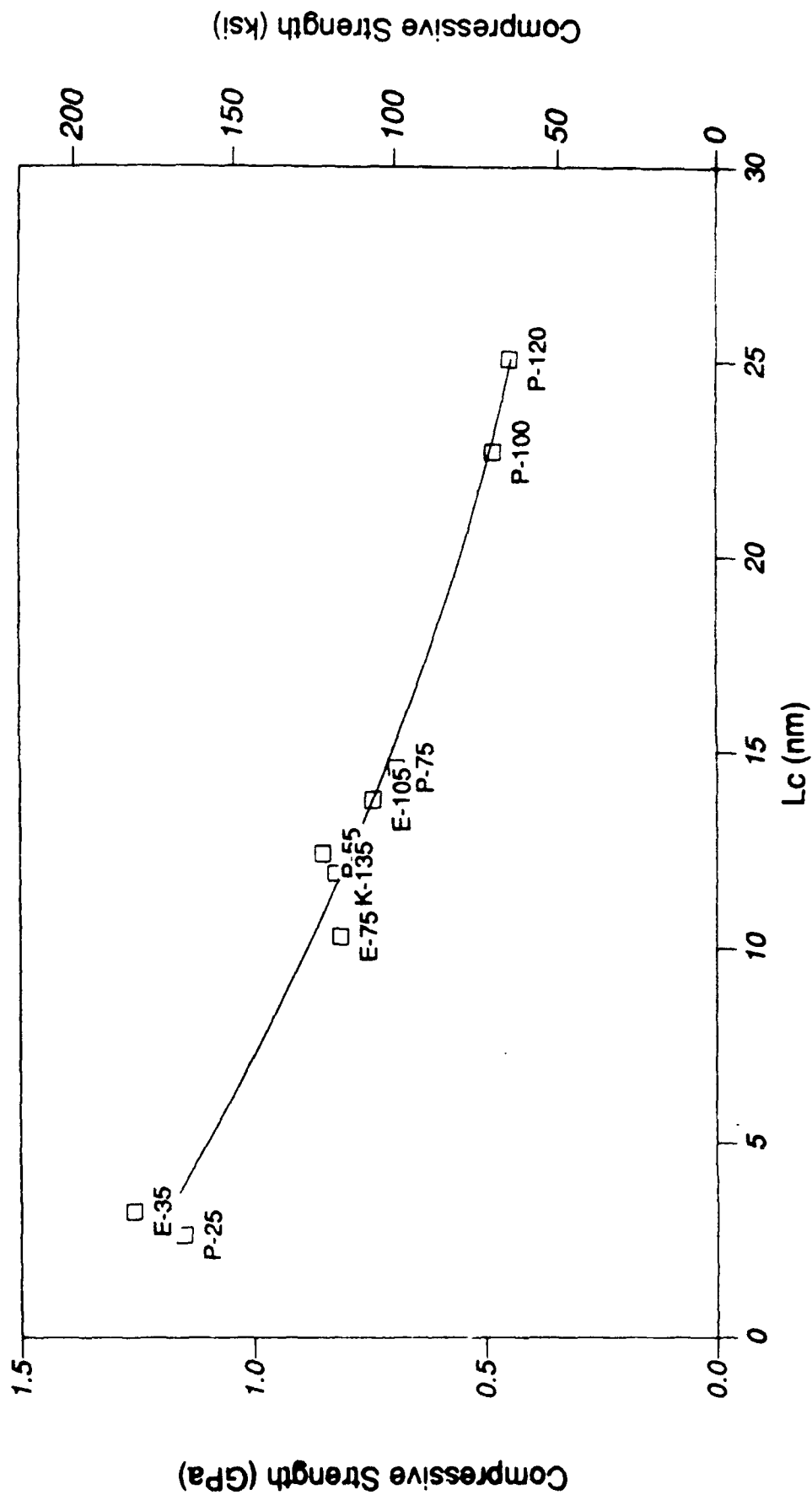
Figure 46. Compressive Strength versus $L_c$ for Pitch-Based Carbon Fibers.
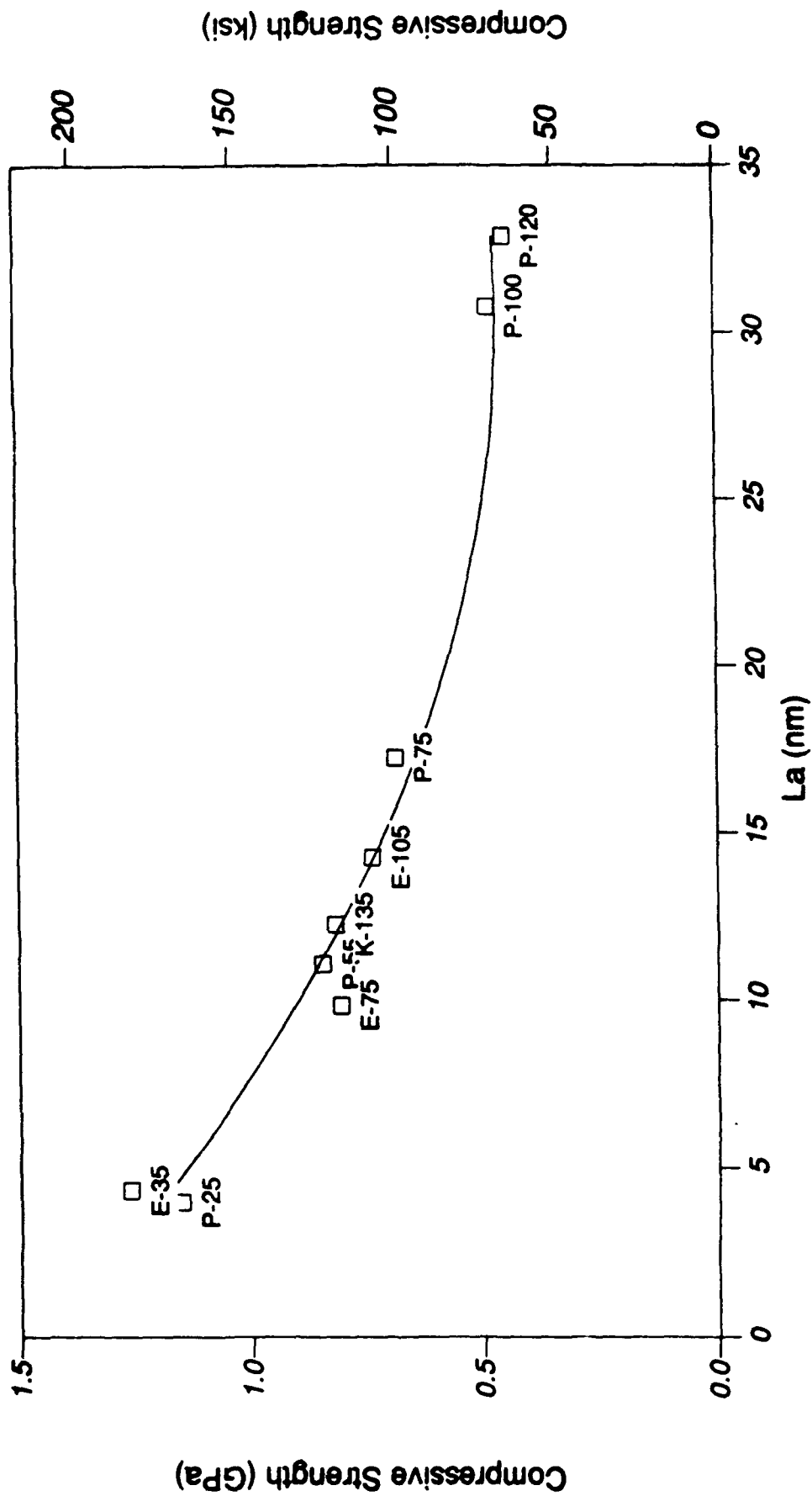
Figure 47. Compressive Strength versus $L_a$ for Pitch-Based Carbon Fibers.

Since these correlations are independent of the fiber source, they should also hold for the PAN-based fibers. On examining Figures 48 and 49, there appears to be a correlation between the CS and crystal size. The T-50 fiber falls below these curves, but there is still a correspondence between increased compression strength and smaller crystal size for a given fiber tensile modulus. This also means that the TM is not uniquely dependent on crystallite sizes, and a given TM can correspond to more than one crystallite size. Processing to obtain smaller crystallite sizes at a given TM should also produce higher strengths in compression.

One would expect the axial fiber compressive strength to be higher for fibers whose crystals were short and fat (the small aspect ratio improving the stability against buckling). This aspect ratio ($L_a/L_c$) is plotted in Figure 50, and there does not appear to be a strong correlation between the compressive strength and $L_a/L_c$. In fact the general trend is the opposite with the higher CS fibers having the largest aspect ratio.

If, however, only the fibers exhibiting 3-dimensional crystals are examined (see Table 3), the expected correlation, albeit with some flaws, can be seen for each precursor group (see Figure 51). A closer examination of the pitch-based fibers in this class (see Figure 52) shows the same trend noted above; that is for a given tensile modulus, a smaller aspect ratio gives a higher compression strength. Thus changing the ratio of $L_a/L_c$ (if possible) appears to be a useful tool to increase the compressive strength in fibers with 3-D character.

## 3.2    HEAT TREATED FIBERS

### 3.2.1    Commercial Fibers

Table 4 lists the WAXD parameters measured on the commercial fibers which had been heat treated. These fibers were all pitch-based carbon fibers: P-25, P-55, and E-35. The results in this table are also presented graphically in Figures 53-57.

Both the d-spacing and degree of graphitization remain unchanged until the heat treatment temperature exceeds 1500°C. The decrease in d-spacing (and increase in graphitization) at higher temperatures is more rapid for P-25 and E-35 than for P-55. The crystallite sizes ($L_c$ and $L_a$) follow the same trends, increasing after 1500°C, with P-55 more gradual than the other two (Figures 56 and 57).

64
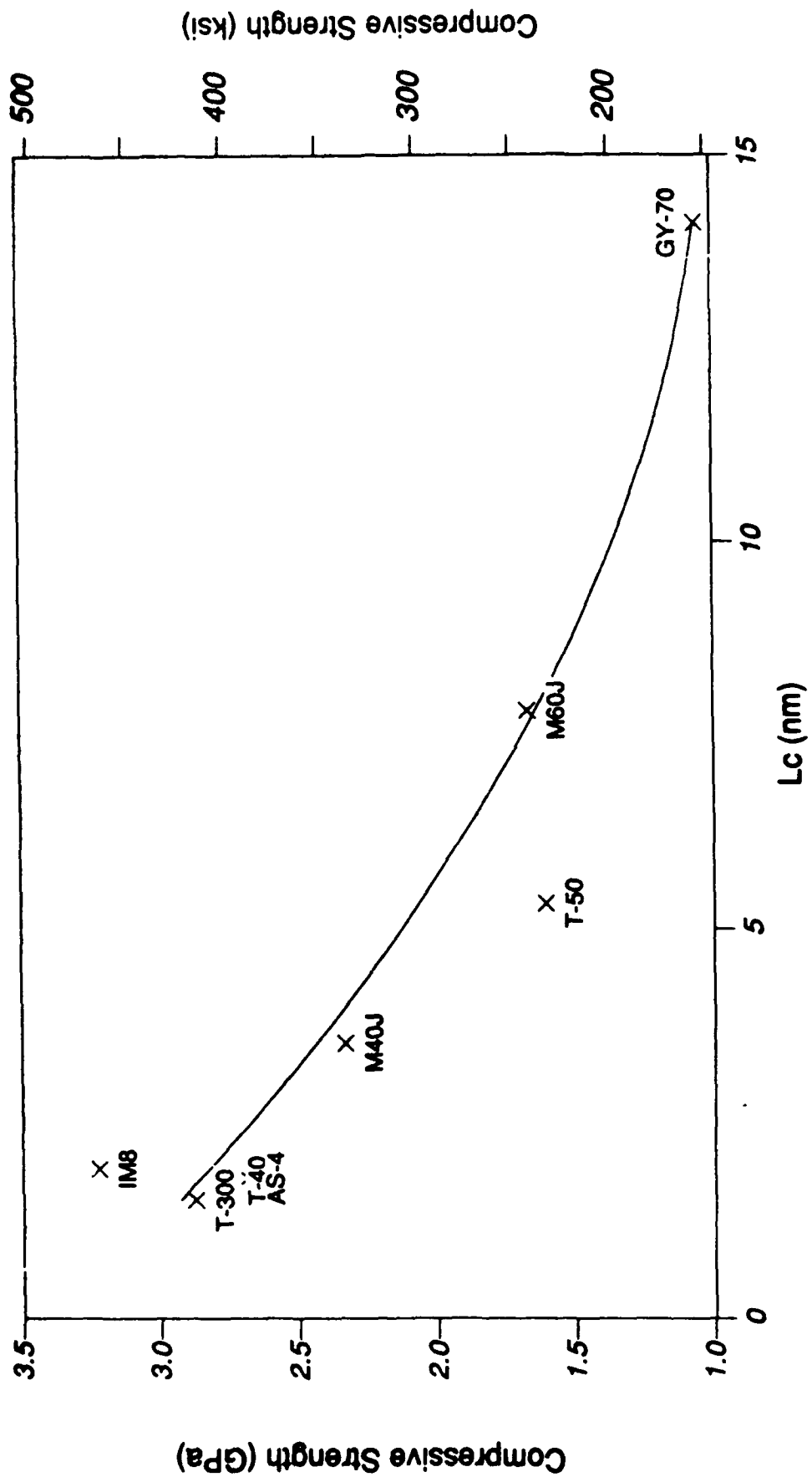
Figure 48. Compressive Strength versus $L_C$ for PAN-Based Carbon Fibers.
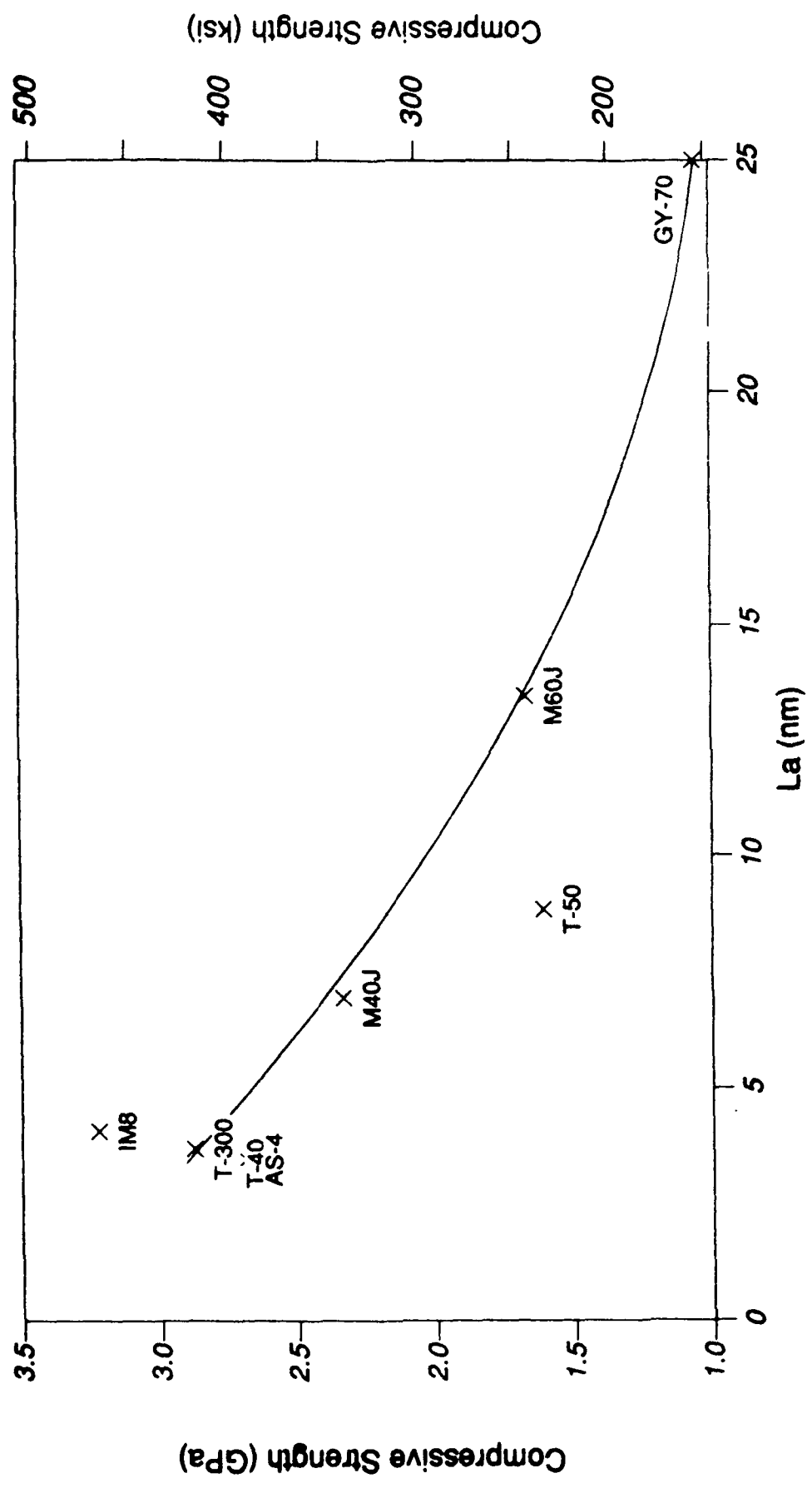
Figure 49. Compressive Strength versus $L_a$ for PAN-Based Carbon Fibers.
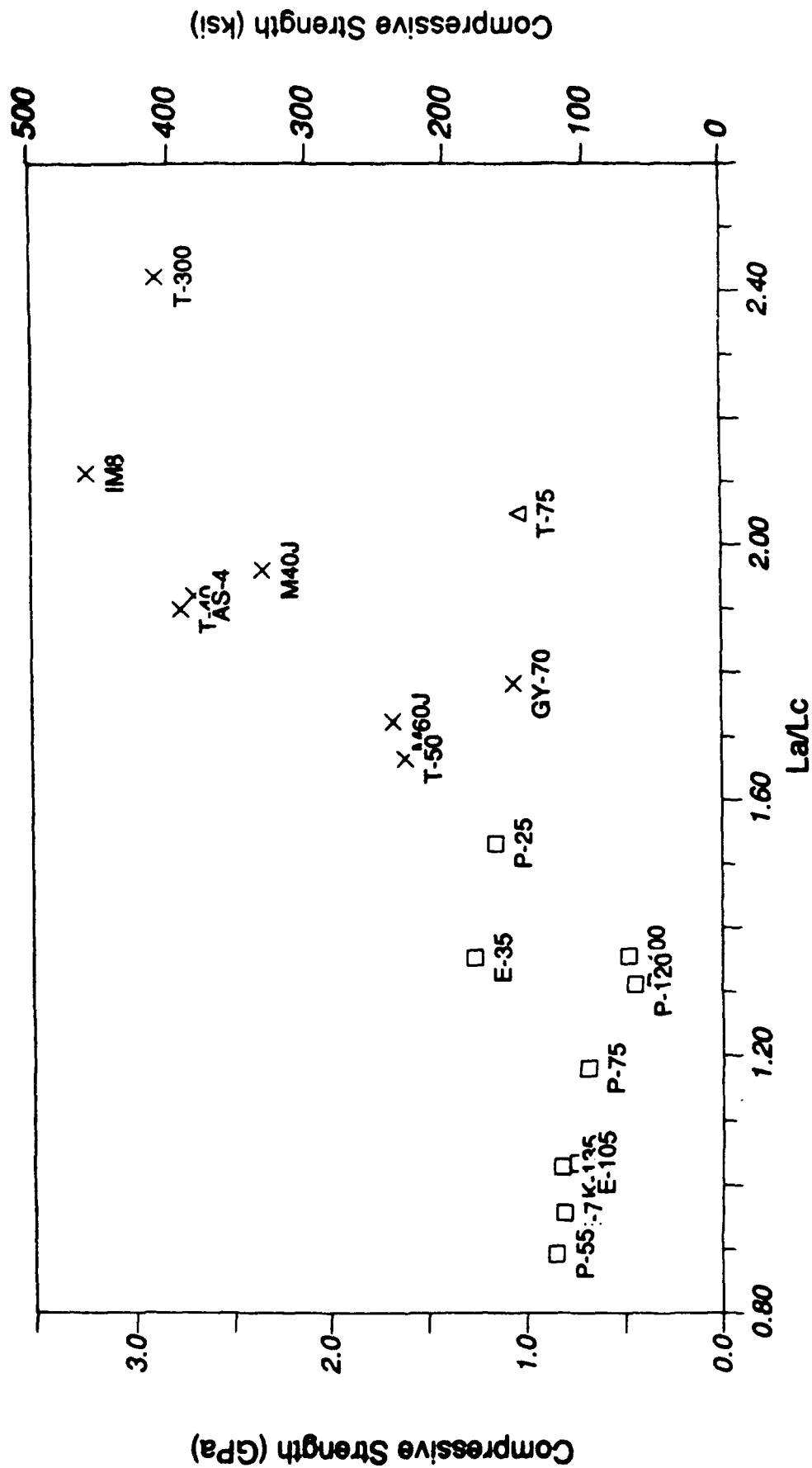
Figure 50. Compressive Strength versus $L_a/L_c$ for Carbon Fibers.
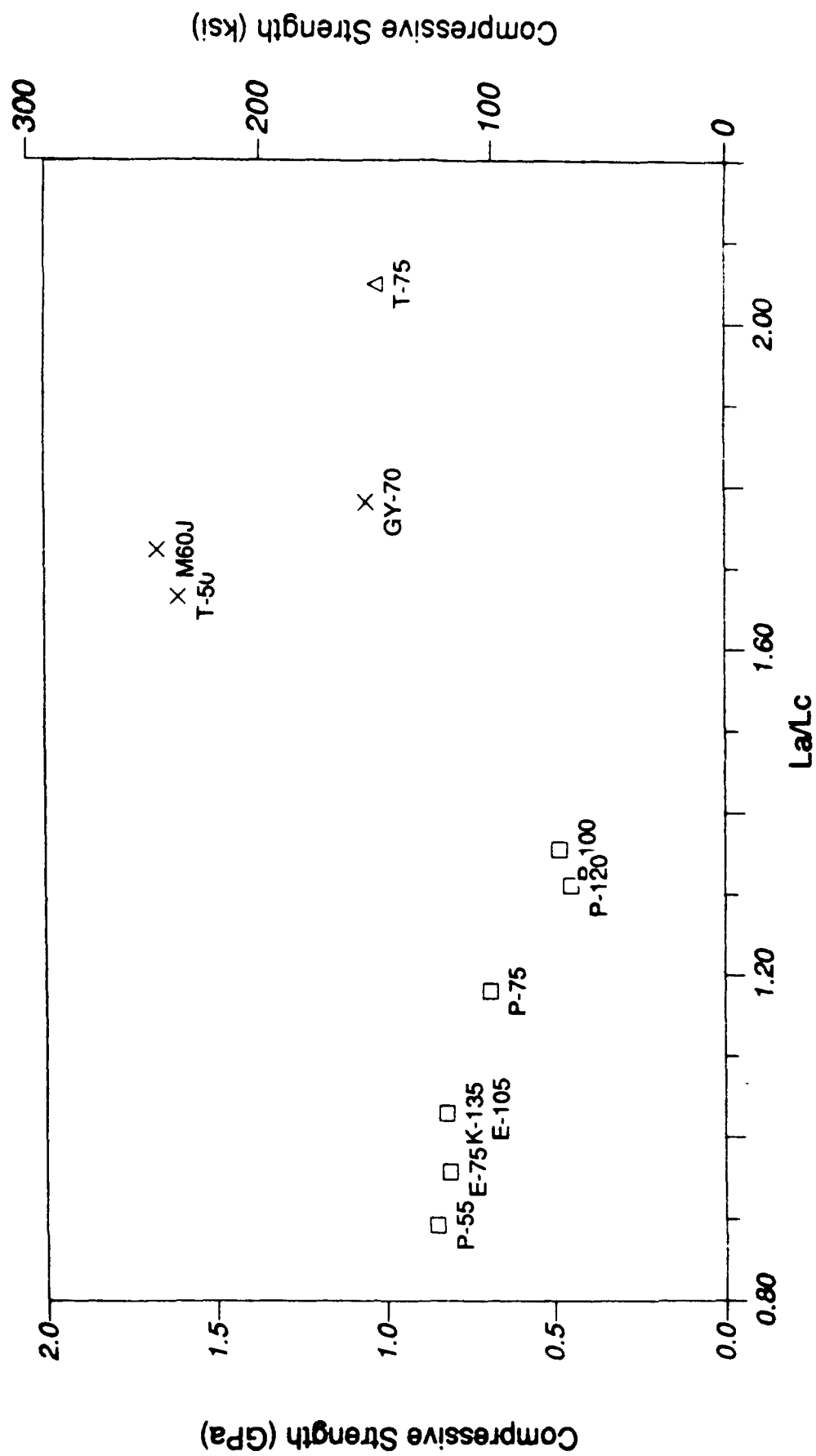
Figure 51. Compressive Strength versus $L_a/L_c$ for Carbon Fibers with 3-D Crystals.
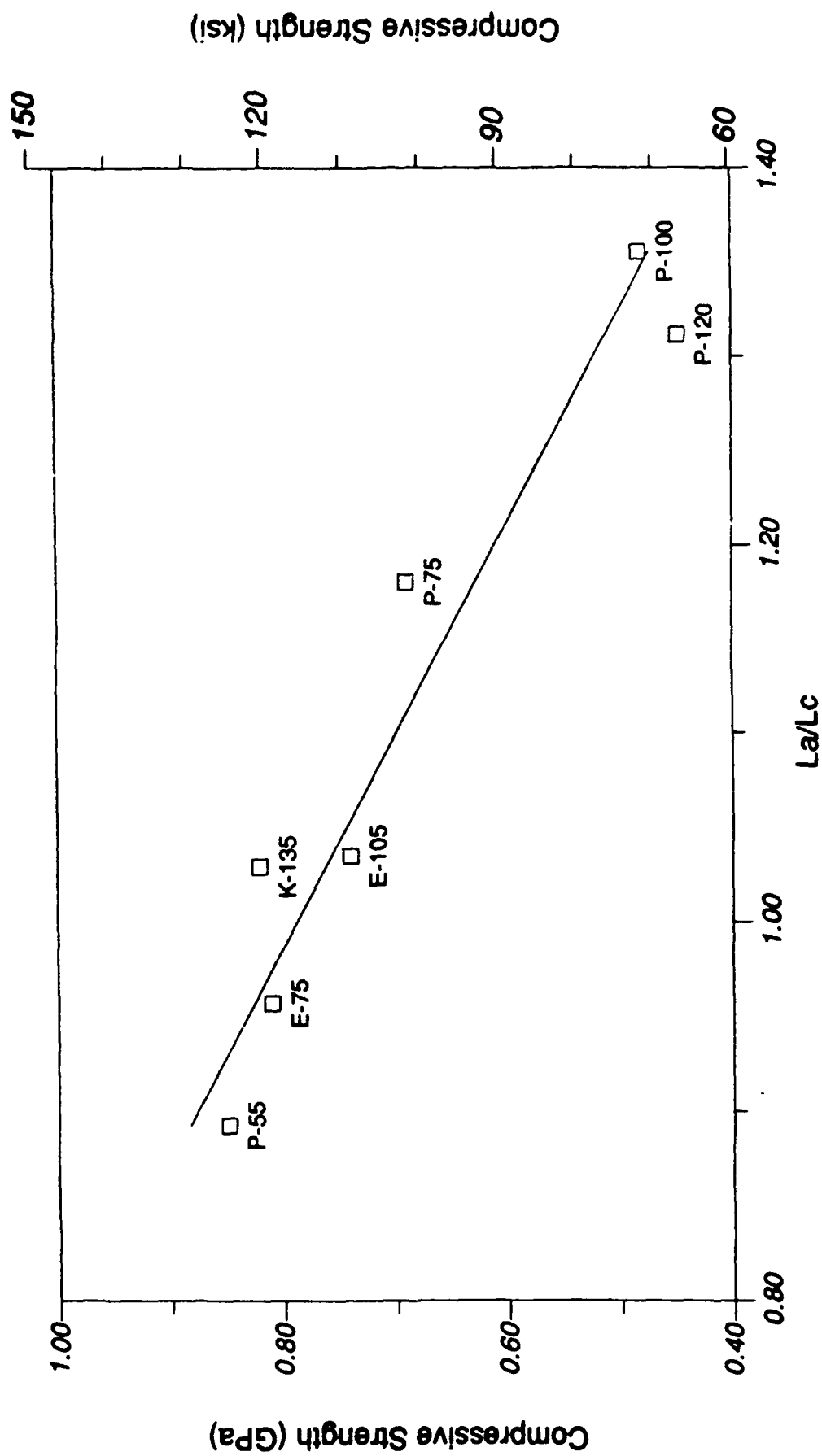
Figure 52. Compressive Strength versus $L_a/L_c$ for Pitch-Based Carbon Fibers with 3-D Crystals.

## TABLE 4

### SUMMARY OF X-RAY DIFFRACTION RESULTS ON HEAT-TREATED COMMERCIAL FIBERS

| Fiber | Heat Treatment Temp. (°C) | d-spacing (00,2) (nm) | Degree of Graphite $g_p$ | Z FW-HM (°) | $L_c$ (00.2) (nm) | $L_a$ (11) (nm) |
|---|---|---|---|---|---|---|
| **P-25** | | | | | | |
| Previous | | 0.344 | 0.02 | 31.9 | 2.6 | na |
| As Rec'd | | 0.343 | 0.11 | 30.4 | 2.7 | 3.9 |
| | 1000 | 0.3435 | 0.06 | 30.6 | 2.5 | 4.0 |
| | 1500 | 0.3434 | 0.07 | 25.8 | 3.6 | 4.8 |
| | 2000 | 0.3417 | 0.27 | 12.8 | 13.8 | 17.5 |
| | 2300 | 0.3385 | 0.64 | 10.3 | 19.5 | 41.9 |
| **P-55** | | | | | | |
| Previous | | 0.3423 | 0.20 | 14.1 | 12.4 | 16.4 |
| As Rec'd | | 0.3424 | 0.18 | 13.9 | 9.6 | 9.0 |
| | 1000 | 0.3425 | 0.18 | 14.0 | 9.6 | 8.5 |
| | 1500 | 0.3424 | 0.18 | 14.0 | 9.6 | 6.5 |
| | 2000 | 0.3419 | 0.24 | 12.5 | 12.9 | 16.6 |
| | 2300 | 0.3397 | 0.50 | 10.2 | 15.1 | 32.1 |
| **E-35** | | | | | | |
| Previous | | 0.344 | -0.03 | 21.6 | 3.2 | 4.4 |
| As Rec'd | | 0.344 | 0.02 | 22.1 | 3.5 | 4.1 |
| | 1000 | 0.3435 | 0.06 | 21.5 | 3.5 | 4.4 |
| | 1500 | 0.3432 | 0.09 | 19.5 | 4.2 | 4.4 |
| | 2000 | 0.3414 | 0.31 | 6.8 | 15.1 | 19.9 |
| | 2300 | 0.3379 | 0.71 | 6.4 | 21.1 | 45.8 |

Previous indicates the untreated fibers measured in earlier work and reported in section 3.1. Differences between "Previous" and "As Received" fibers indicate experimental error limitations.

na - value not available
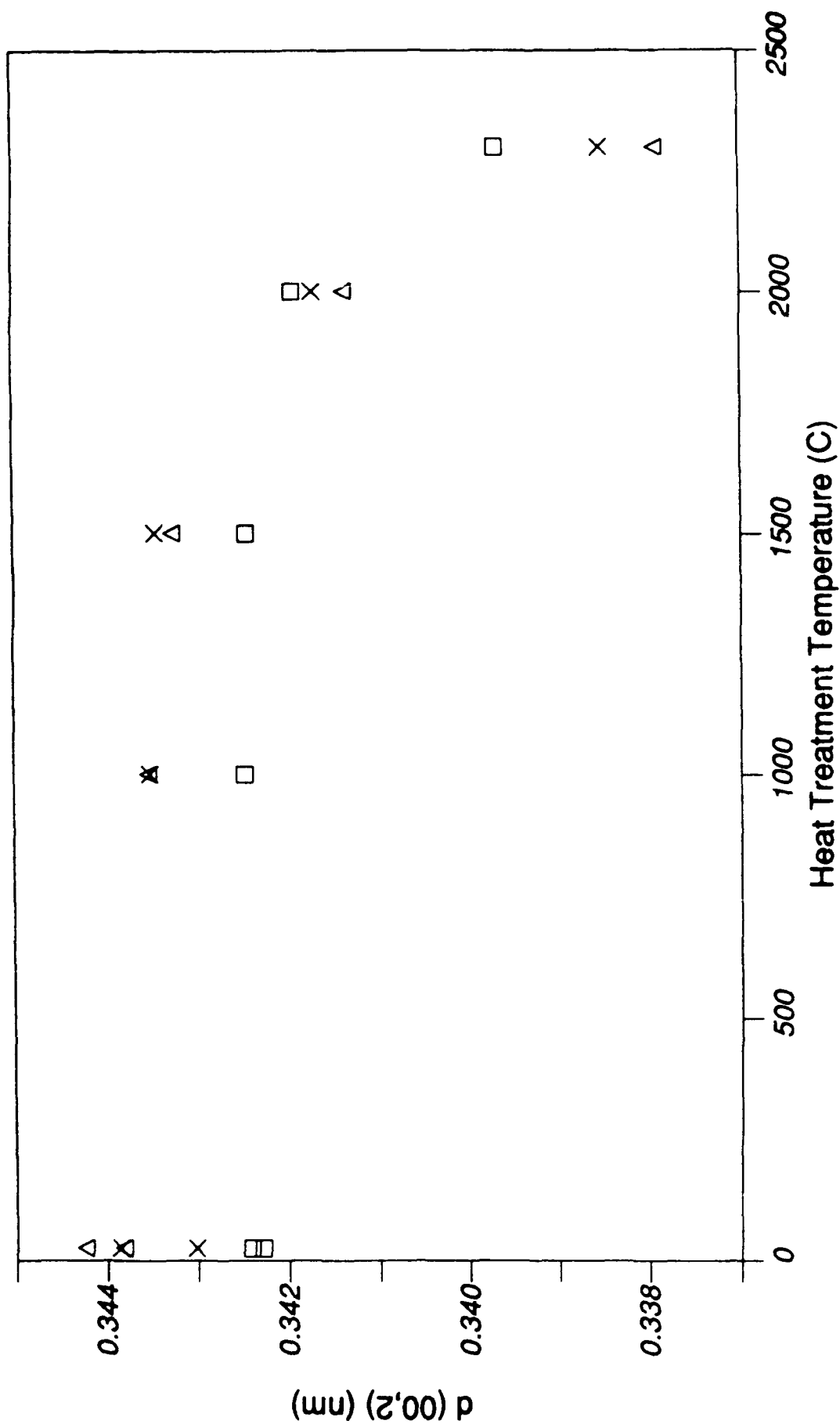
Figure 53. d$_{(00,2)}$ Spacing versus Heat Treatment Temperature for Commercial Carbon Fibers.
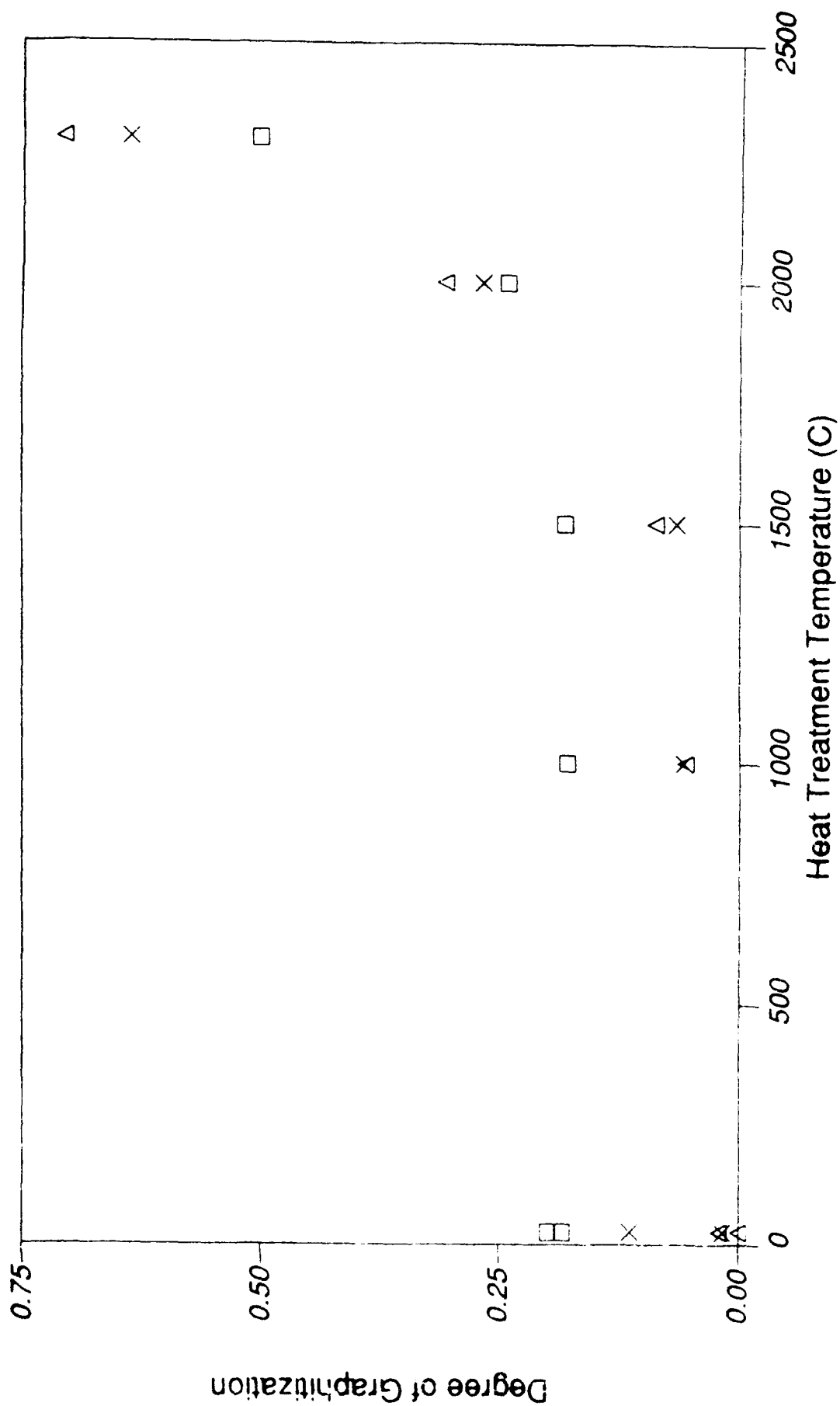
Figure 54. Degree of Graphitization versus Heat Treatment Temperature for Commercial Carbon Fibers.
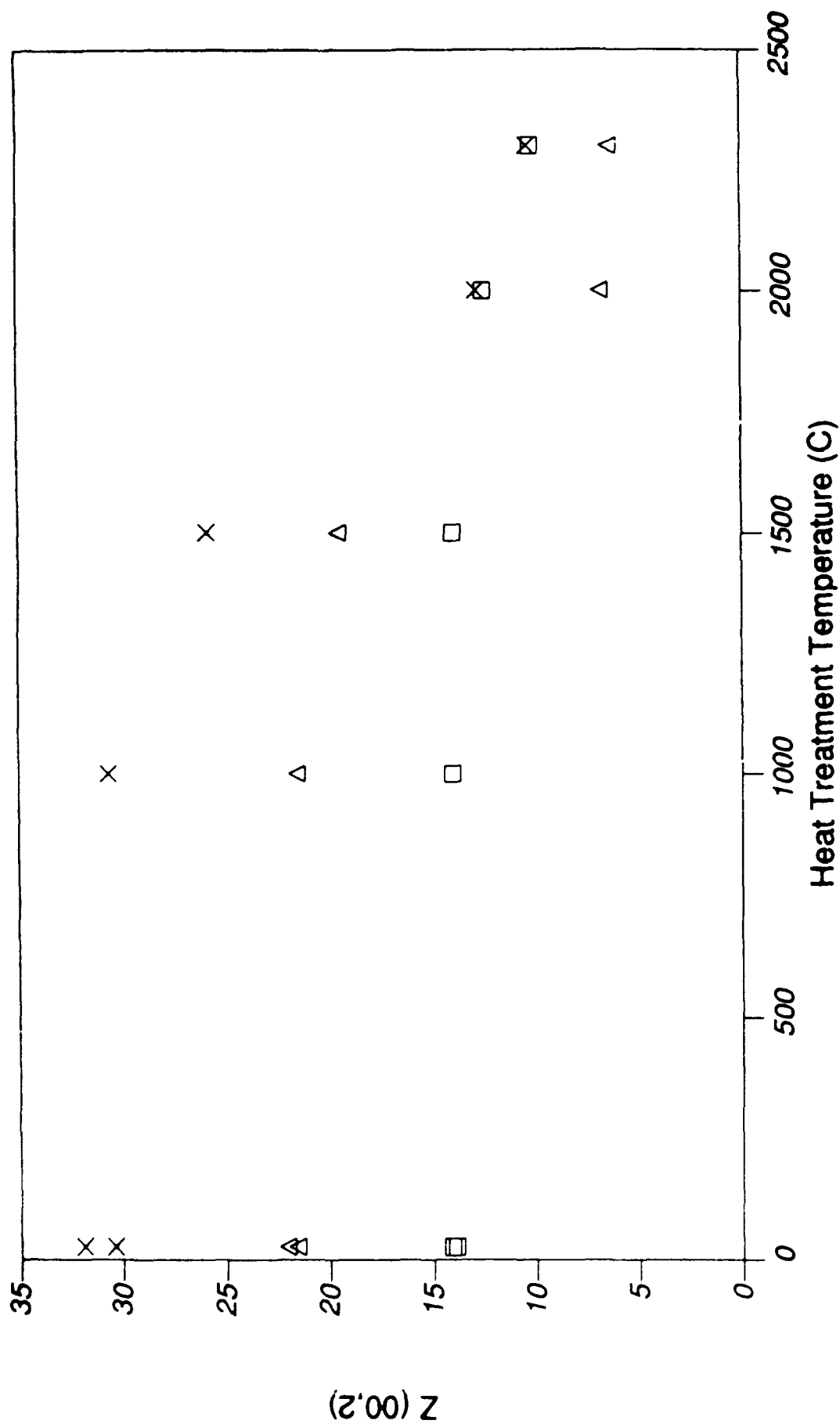
Figure 55.  $Z_{(00,2)}$  versus Heat Treatment Temperature for Commercial Carbon Fibers.
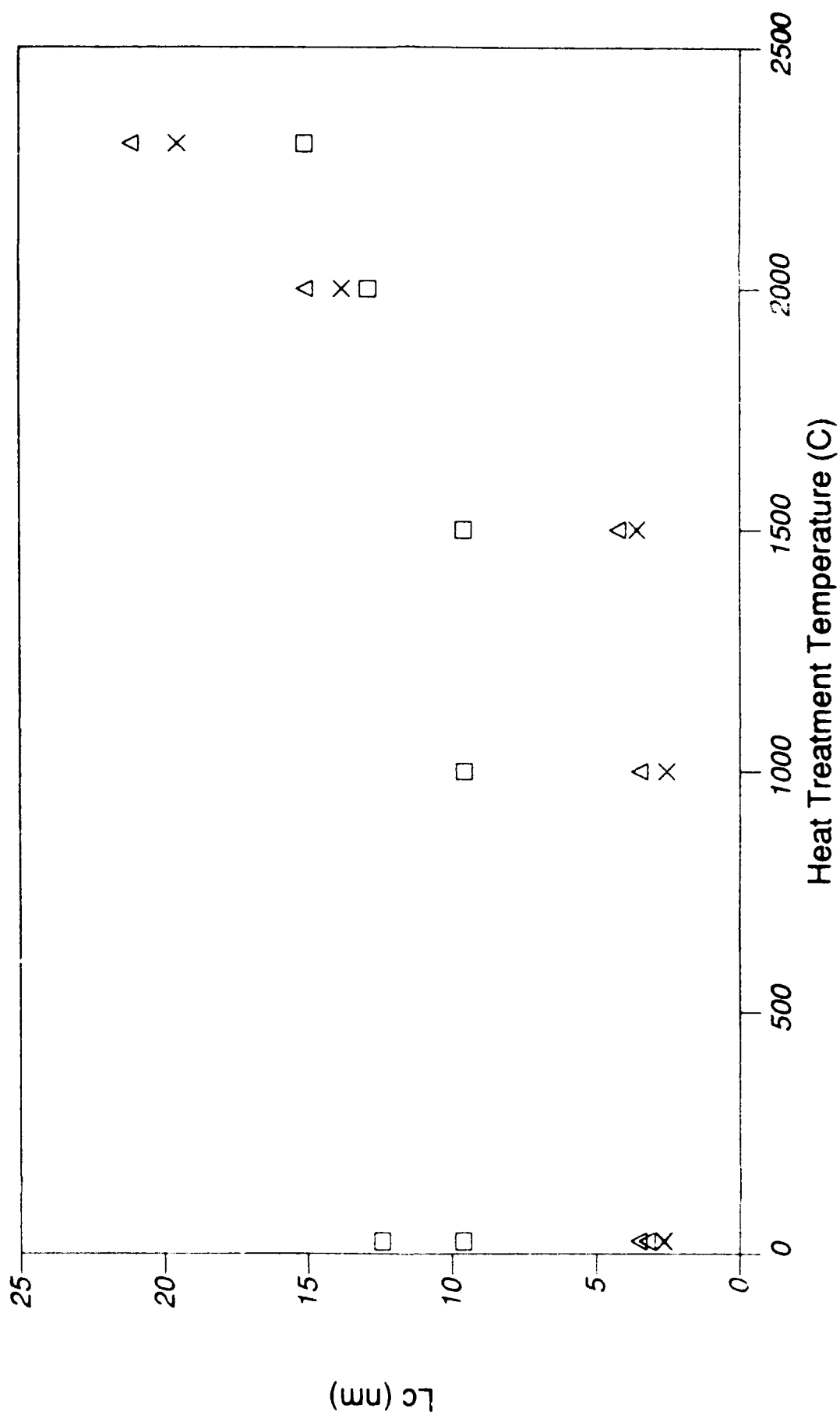
Figure 56. $L_c$ versus Heat Treatment Temperature for Commercial Carbon Fibers.
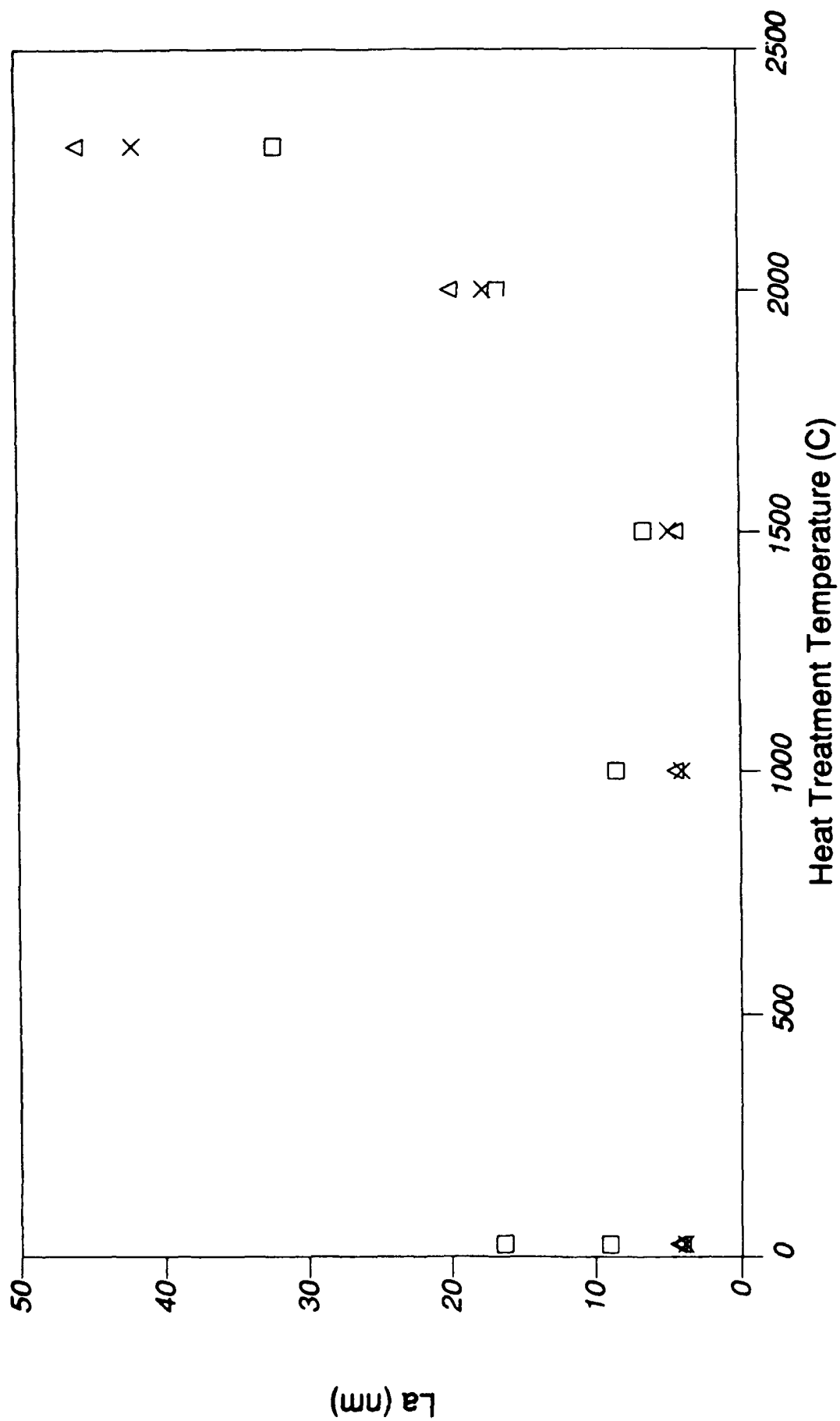
Figure 57. $L_a$ versus Heat Treatment Temperature for Commercial Carbon Fibers.

The orientation on the other hand increases for P-25 and E-35 beginning at 1000°C, while P-55's doesn't improve until above 1500°C. The final $Z_{(00,2)}$ of the P-25 and P-55 are indistinguishable at 2300°C, while E-35 has the greatest orientation (Figure 54).

### 3.2.2    Vapor Grown Carbon Fibers

Table 5 lists the WAXD parameters measured on the VGCF fibers which had been heat treated. Figures 58-62 show the results of 15-minute heat treatments.

Higher heat treatment temperatures were employed for the VGCF than for the commercial fibers. The development of 3-D crystals was very strongly evident starting at the 2500°C heat treatment. This is reflected in the d-spacing decrease (Figure 58) to the most compact fibers examined with a degree of graphitization of 0.75 at 2500°C to over 0.90 at the highest heat treatment temperature (Figure 59).

The $L_c$ values apparently increase and then decrease with a rise in the heat treatment temperature (Figure 60). This is probably not true as the crystallite sizes above 2500°C exceed the instrumental limits of the x-ray diffractometer; that is the instrumental broadening correction is on the same order of sizes as the measured breadth. $L_a$ shows a better curve even though the curves it is measured from also approach the instrumental limits (Figure 61).

The sizes of the 3-dimensional crystals $(L_{(hk,\ell)})$ are within measurable limits (not visible in the "as grown" or 2200°C heat treated fibers). There is a nice smooth increase in size as the heat treatment temperature increases.

Orientation was not measurable in the VGCFs because the branching and nonlinear growth of these fibers prevented the formation of a tight or parallel bundle for diffraction scans.

## TABLE 5

### SUMMARY OF X-RAY DIFFRACTION RESULTS ON HEAT-TREATED VAPOR GROWN CARBON FIBERS

| Heat Treatment Temp. (°C) | d-spacing (00,2) (nm) | Degree of Graphite $g_p$ | $L_c$ (00,2) (nm) | $L_a$ (11) (nm) | $L_{hk,\ell}$ (10,1) (nm) | (11,2) (nm) |
|---|---|---|---|---|---|---|
| As Grown P | 0.345 | -0.13 | 2.0 | 3.4 | NA | NA |
| 2200 | 0.3419 | 0.24 | 21.2 | 23.7 | NA | NA |
| 2500 | 0.3376 | 0.75 | 36.0 | 30.5 | 4.1 | 6.4 |
| 2700 | 0.3369 | 0.83 | 56.1 | 41.4 | 12.0 | 11.2 |
| 2800 | 0.3365 | 0.87 | 52.9 | 42.9 | 14.0 | 14.5 |
| 2900 | 0.3359 | 0.94 | 35.1 | 43.9 | 19.7 | 20.5 |
| 2800 (10 min) | 0.3365 | 0.88 | 62.8 | 37.3 | 13.5 | 13.8 |

P    - Indicates measurements taken with the Picker diffractometer (all other measurements used the Huber diffractometer)

NA  - value not applicable
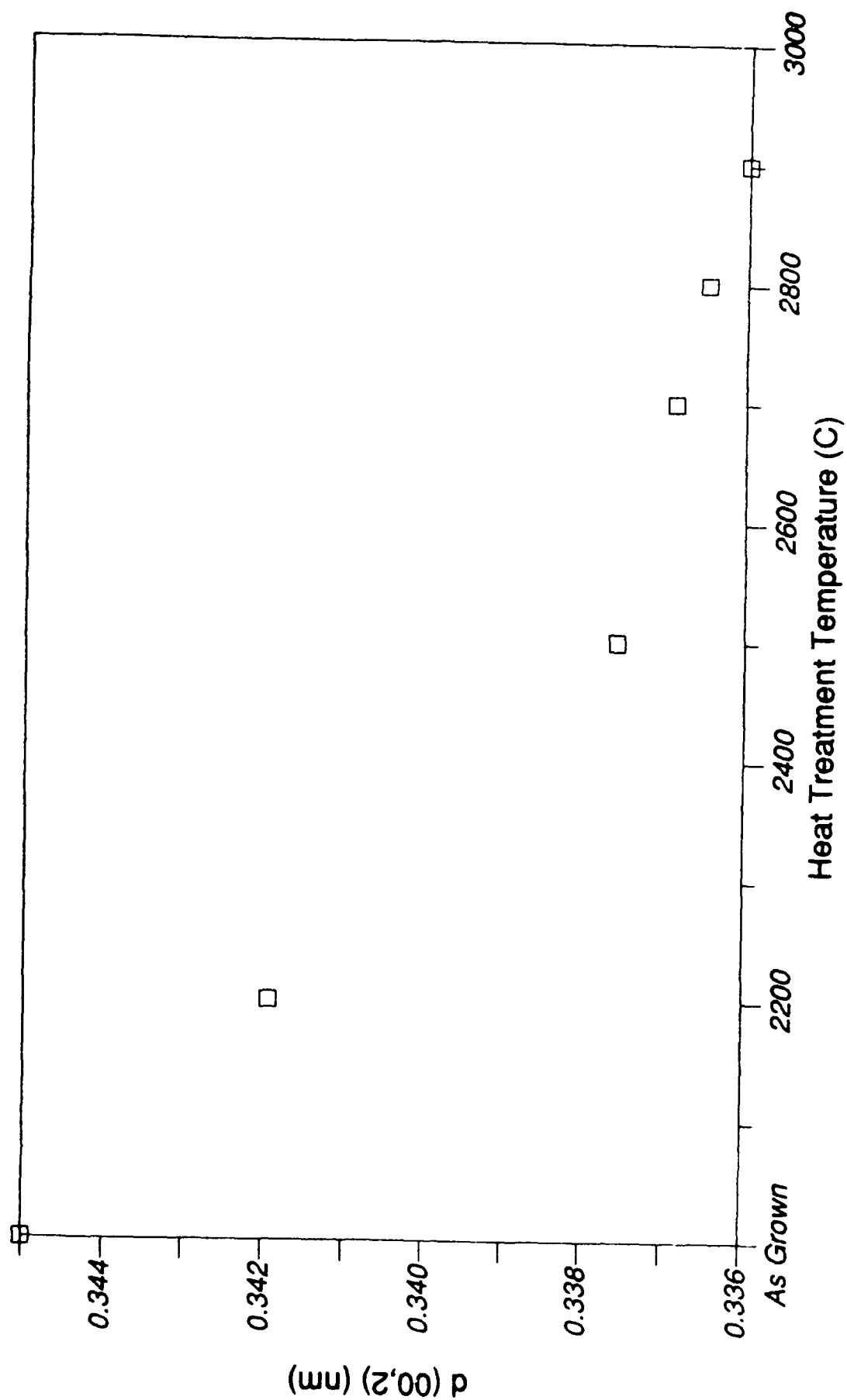
Figure 58. $d_{(00,2)}$ Spacing versus Heat Treatment Temperature for Vapor Grown Carbon Fibers.
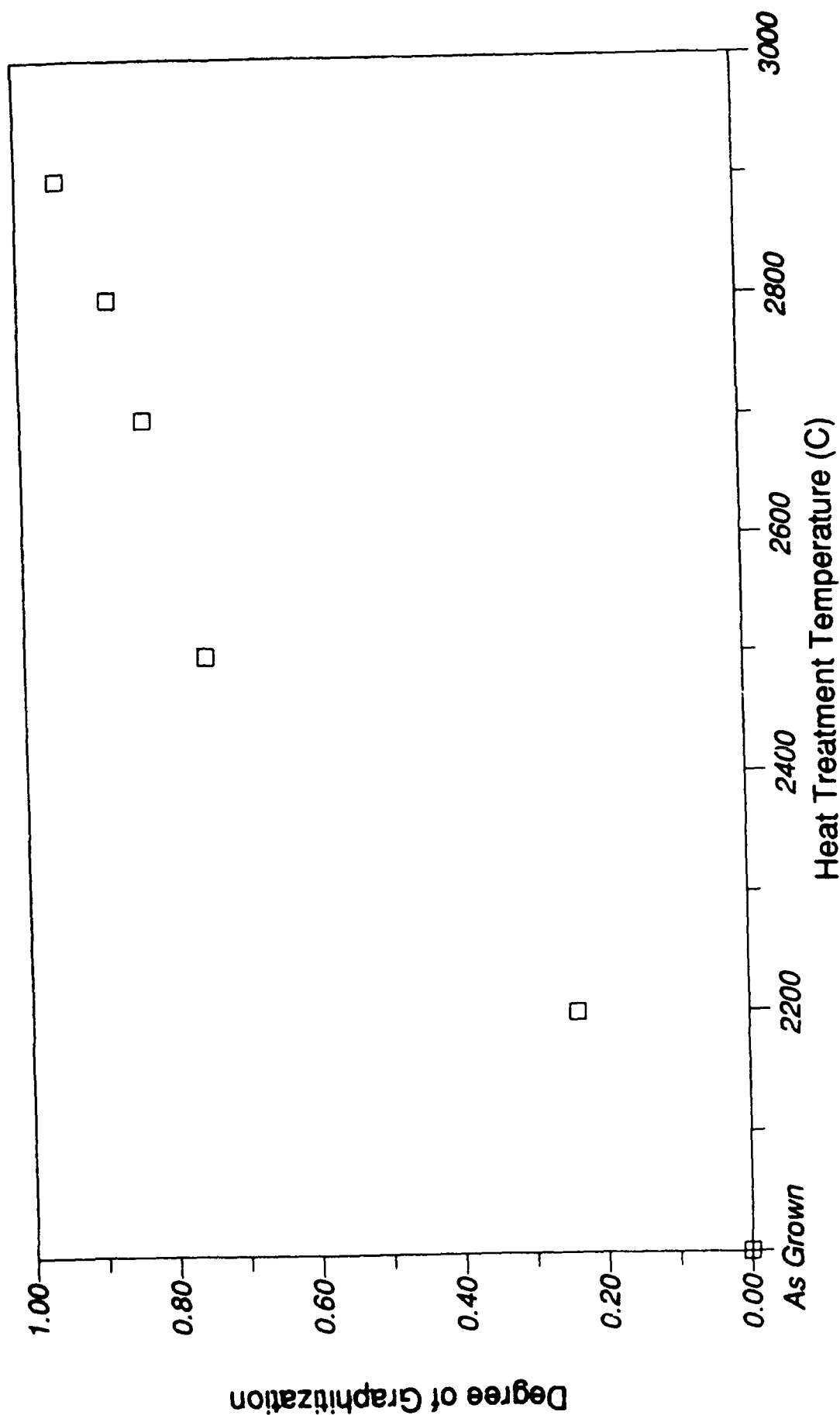
Figure 59.  Degree of Graphitization versus Heat Treatment Temperature for Vapor Grown Carbon Fibers.
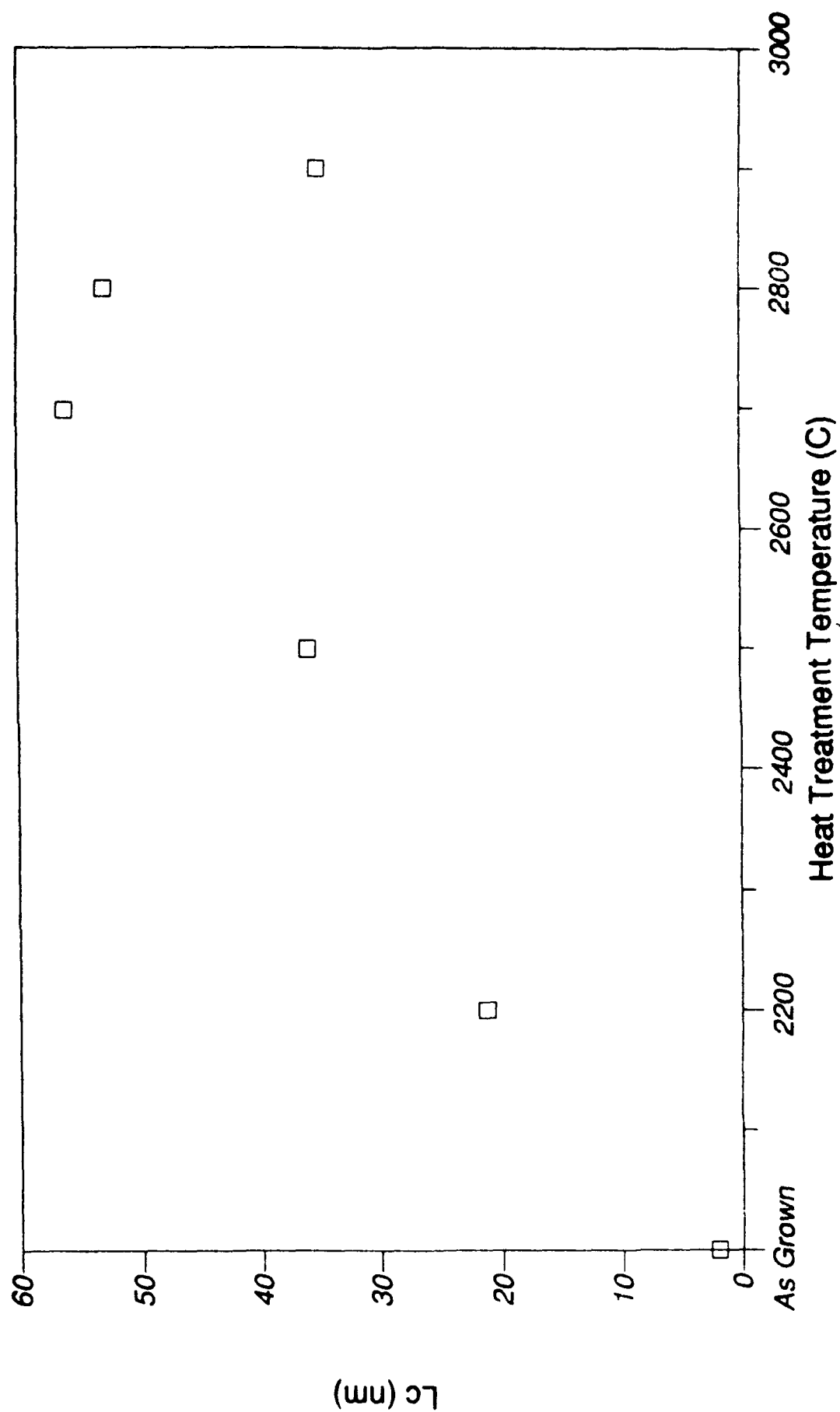
Figure 60.  $L_C$  versus Heat Treatment Temperature for Vapor Grown Carbon Fibers.
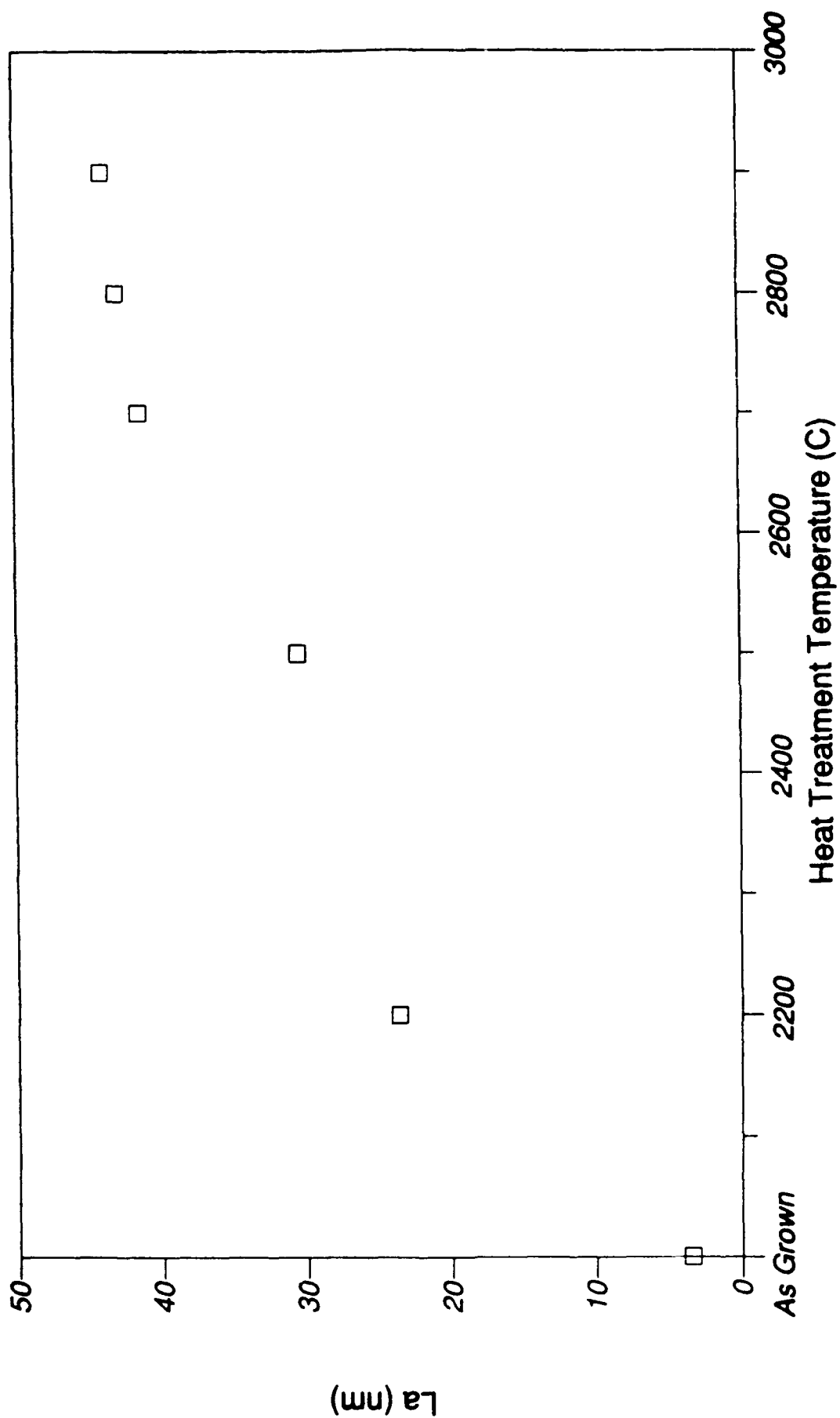
Figure 61. $L_a$ versus Heat Treatment Temperature for Vapor Grown Carbon Fibers.

81
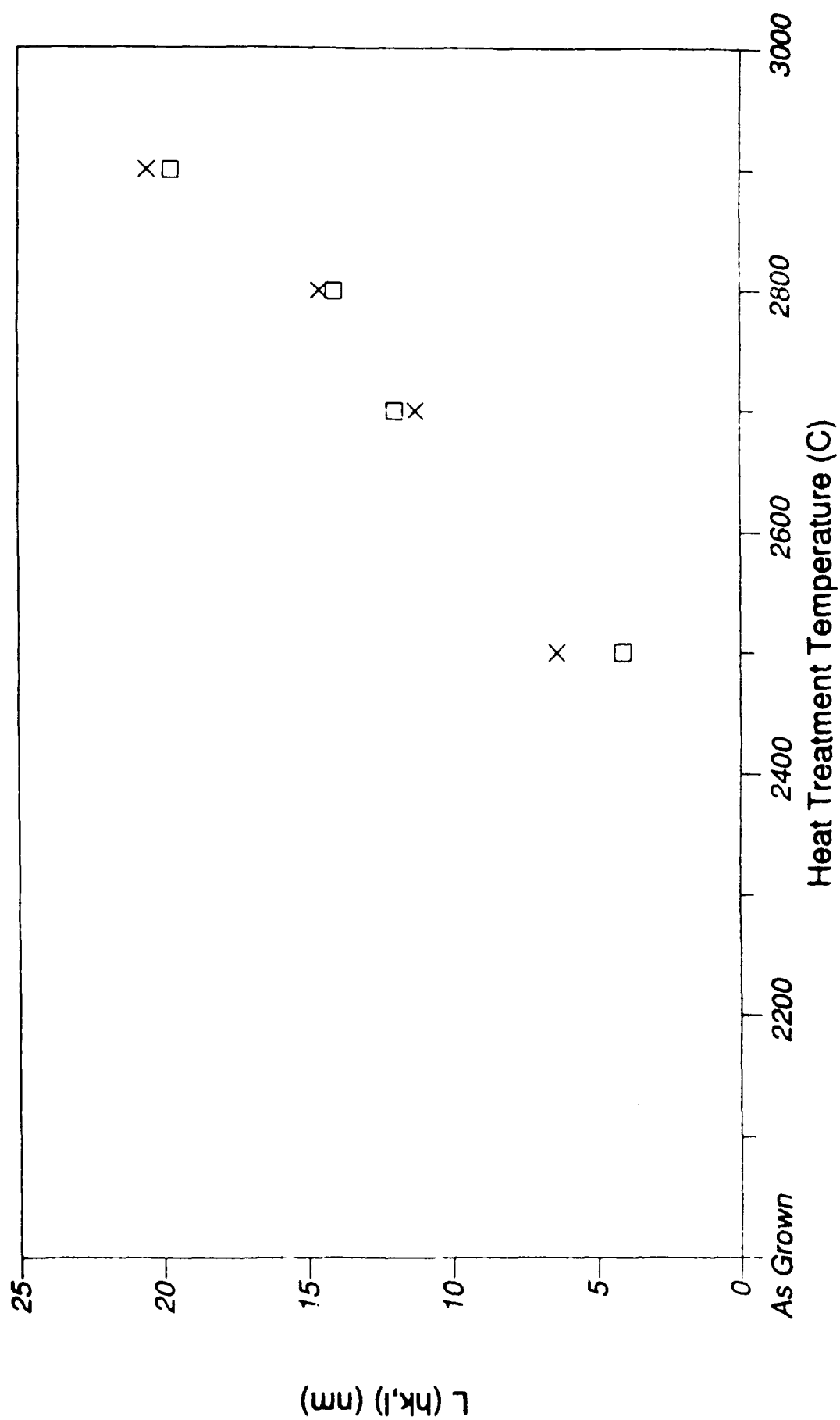
Figure 62. $L_{(hk,\ell)}$ versus Heat Treatment Temperature for Vapor Grown Carbon Fibers.

# 4. CONCLUSIONS

Tensile modulus is apparently governed by the crystallite orientation with only minor differences at low TM between pitch- and PAN-based fibers. Other correlations, such as degree of graphitization and crystallite size, are true only within a production series and not generally applicable.

Correlations of crystal structures with tensile strength are generally very poor. Within a production series, one can see correlations of TS with $d_{(00,2)}$, $Z_{(00,2)}$, void content, $L_c$, and $L_a$, but the differences among the various production runs and precursors are greater than the variations within any series.

Correlations with compression strength show that crystallite size has the most influence on fiber CS - smaller crystals producing higher CS. In fibers with 3-D crystals, short and fat crystals produce the highest CS. Since these trends are observed for the different precursor materials but fibers from each precursor make separate curves, there are other factors that influence the CS as well

The comparisons made between structure and properties here are subject to error. Several measured parameters used which need improvement are true fiber compression strength, fiber density, and absolute $L_a$ values parallel to the fiber particularly in fibers with 3-D crystals.

While little can be predicted about the effects of structure on tensile strength, tensile modulus can be improved by increasing a fiber's graphitic orientation; and its compression strength can be improved by keeping the crystallite size small.

Heat treating a carbon fiber alone will increase the graphitic crystalline orientation, degree of graphitization, and crystallite sizes. The effects on mechanical properties are not currently known, but presumably the tensile modulus will increase with the increased orientation. The change in strength cannot be predicted solely on the crystallographic information.

# REFERENCES

1. D. P. Anderson, "Carbon Fiber Morphology: Wide-Angle X-ray studies of Pitch- and PAN-Based Carbon Fibers," WRDC-TR-89-4072, US Air Force Technical Report, July 1989.

2. Karren K. Brito, David P. Anderson, and Brian P. Rice, "Graphitization of Vapor Grown Carbon Fibers," SAMPE Symposium Preprints, 34, 190 (1989).

3. D. P. Anderson and Satish Kumar "Compressive Strength and Morphology of Pitch- and PAN-Based Carbon Fibers," submitted to Proceedings of SPE ANTEC-90, Dallas, TX, May 1990.

4. A. S. Crasto and D. P. Anderson, "Correlation of Structure and Compressive Strength in Pitch-Based Graphite Fibers," Proc. of the Am. Soc. for Composites, 5th Tech. Conf. on Composite Materials, pp. (1990).

5. A. Sumida, K. Ono, and Y. Kawazu, "PAN Based High Modulus Graphitized Carbon Fiber Torayca M60J," SAMPE Symposium Preprints, 34, 2579 (1989).

6. S. Kumar, W. W. Adams, and T. E. Helminiak, "Uniaxial Compressive Strength of High Modulus Fibers for Composites," J. Reinforced Plast. and Comp., 7, 108 (1988).

7. J. H. Greenwood and P. G. Rose, J. Mater. Sci., 9, 1809 (1974).

8. H. M. Hawthorne and E. Teghtsoonian, "Axial Compression Fracture in Carbon Fibers," J. Mater. Sci., 10, 41 (1975).

9. J. D. H. Hughes, "The Evaluation of Current Carbon Fibers," Phys. D: Appl. Phys., 20, 276 (1987).

10. S. Kumar, "Structure and Properties of High Performance Polymeric and Carbon Fibers - An Overview," Fiber Prod. Conf. Proc. (1988).

11. M. S. Dresselhaus, G. Dresselhaus, K. Sugihara, I. L. Spain, and H. A. Goldberg, Graphite Fibers and Filaments, Springer-Verlag, New York, 1988, Chapt. 3.

12. Satish Kumar and T. E. Helminiak, "Compressive Strength of High Performance Fibers," in The Materials Science and Engineering of Rigid-Rod Polymers, W. W. Adams, R. K. Eby, and D. E. McLemore, eds., Materials Research Society Symposium Proceedings, Vol. 134, Pittsburgh, PA (1989).

13. "Improved Technology for Advanced Composite Materials," UDR-NM-SA-90-08, University of Dayton Research Institute Report, April 1990.

14.    D. P. Anderson, "X-ray Analysis Software: Operation and Theory Involved in Program "DIFF"," AFWAL-TR-85-4079, US Air Force Technical Report, June 1985.

15.    A. Fourdeux, R. Perret, and W. Ruland, "The Effect of Preferred Orientation on (hk) Interferences as Shown by Electron Diffraction of Carbon Fibers," J. Appl. Cryst., 1, 252 (1968).

16.    G. Northolt and H. A. Stuut, "Determination of the Crystal Density of Polymers by X-Ray Diffraction," JPS, Polym. Phys. Ed., 16, 939 (1978).

17.    Rosalind E. Franklin, "The Structure of Graphitic Carbons," Acta Cryst., 4, 253 (1951).

18.    Rosalind E. Franklin, "The Interpretation of Diffuse X-ray Diagrams of Carbon," Acta Cryst., 3, 107 (1950).

19.    K. Jain and A. S. Abhiraman, "Conversion of Acrylonitrile-Based Precursor Fibers to Carbon Fibers," J. Mater. Sci., 22, 278 (1987).

20.    P. M. de Wolff, "On the Lorentz Factor for Integrated Intensities from Azimuthal and Radial Diffractometer Records of Fiber Patterns," J. Polymer Sci., 60, S34, (1962).

21.    W. Ruland, "X-Ray Diffraction Studies on Carbon and Graphite," in Chemistry and Physics of Carbon: A Series of Advances, Vol. 4, pp 1-84 (1968), Philip L. Walker Jr., Ed., Marcel Dekker, Inc., New York.

22.    Satish Kumar and T. E. Helminiak, "Compressive Strength of High Performance Fibers," in The Materials Science and Engineering of Rigid-Rod Polymers, W. W. Adams, R. K. Eby, and D. E. McLemore, eds., Materials Research Society Symposium Proceedings, Vol. 134, Pittsburgh, PA (1989).

23.    P. Scherrer, Gottinger Nachrichten, 2, 98 (1918).

24.    R. Hosemann, Z. Physik, 128, 1 (1950).

25.    R. Hosemann, Z. Physik, 128, 464 (1950).

26.    D. R. Buchanan, R. I. McCullough and R. L. Miller, "Crystal-lite Size and Lattice Distortion Parameters from X-ray Line Broadening," Acta Cryst., 20, 922 (1966).

27.    P. Galen Lenhert, personal communications, February 1990.

28.    W. Ruland, "Fourier Transform Methods for Random-Layer Line Profiles," Acta Cryst., 22, 615 (1967).

29.    B. E. Warren and P. Bodenstein, "The Shape of Two-Dimensional Carbon Black Reflections," Acta Cryst., 20, 602 (1966).

30.  B. E. Warren, Phys. Rev., 59, 693 (1941).

31.  A. J. C. Wilson, "X-Ray Diffraction by Random Layers: Ideal Line Profiles and Determination of Structure Amplitudes from Observed Line Profiles," Acta Cryst., 2, 245 (1949).

32.  W. Ruland and H. Tompa, "The Effect of Preferred Orientation on the Intensity Distribution of (hk) Interferences," Acta Cryst., A24, 93 (1968).

33.  R. J. Diefendorf, personal communication, January 1990; he had also contacted W. Ruland who was of the same opinion on this issue.

34.  R. Perret and W. Ruland, "The Microstructure of PAN-Based Carbon Fibers," J. Appl. Cryst., 3, 525 (1970).

35.  M. M. Hall Jr., V. G. Veeraraghavan, H. Rubin, and P. G. Winchell, "The Approximation of Symmetric X-ray Peaks by Pearson Type VII Distributions," J. Appl. Cryst., 10, 66 (1977).

# APPENDIX A. HERMANS' ORIENTATION ESTIMATION

The basis for this estimation of Hermans' orientation is that the curve fit profile of the azimuthal scan of the (00,2) reflection constitutes the real contribution to the orientation, and the remainder of the scan is baseline and noise.

Pearson Type VII profiles [14,35] were generated for a series of profile breadths and exponents (see Equation 15). A table of orientation functions was then numerically generated using Equations 13 and 14 (see Table 6). Figure 63 shows the extremes of the Pearson profiles, as the Cauchy line is for $m=1$ and the Gaussian line is for $m=\infty$. The plots show only one-half of these profiles and assume $\overline{x}$ is at $\chi=0°$, and the full-width at half-maximum (FW-HM) is $20°$.

Pearson Type VII profiles:

$$I(x) = I_o[1 + (x - \overline{x})^2 / (ma^2)]^{-m} \tag{15}$$

where m is the Pearson exponent, $I_0$ is the intensity at the peak maximum, $\overline{x}$ is the position of the peak maximum, x is the azimuthal position or $\chi$ angle, and a is related to the FW-HM and exponent by:

$$FW\text{-}HM = 2\,a\,[m\,(2^{1/m} - 1)]^{1/2} \tag{16}$$

Figure 64 shows graphically the data presented in Table 6. One can easily see the how the results change very rapidly as the exponent increases from 1 (solid line below the rest).

For actual estimation of $f_{(hk,\ell)}$, one should use Table 6 and interpolate from the curve fit $Z_{(00,2)}$ (FW-HM) and exponent. Results of this type of analysis are shown in Table 7 for some of the fibers reported on in this report.

The values of Hermans' orientation functions of the fibers (00,2) reflection range from 0.76 to 0.99. This indicates that the graphene planes in fibers are oriented parallel to the fiber direction, but no additional insight is gained by using this measure as opposed to $Z_{(00,2)}$.

# TABLE 6

## HERMANS' ORIENTATION FUNCTIONS

$$f_{(hk,\ell)}$$

### Pearson VII Exponent (m)

| FW-HM (°) | (Cauchy) 1 | 2 | 3 | 4 | 5 | 6 | 8 | 10 |
|---|---|---|---|---|---|---|---|---|
| 2 | 0.760 | 0.993 | 0.998 | 0.999 | 0.999 | 0.999 | 0.999 | 0.999 |
| 3 | 0.735 | 0.987 | 0.996 | 0.997 | 0.998 | 0.998 | 0.998 | 0.998 |
| 4 | 0.715 | 0.979 | 0.993 | 0.995 | 0.996 | 0.996 | 0.997 | 0.997 |
| 5 | 0.697 | 0.970 | 0.989 | 0.993 | 0.994 | 0.994 | 0.995 | 0.995 |
| 6 | 0.681 | 0.960 | 0.985 | 0.989 | 0.991 | 0.992 | 0.992 | 0.993 |
| 7 | 0.666 | 0.949 | 0.980 | 0.985 | 0.988 | 0.989 | 0.990 | 0.990 |
| 8 | 0.652 | 0.938 | 0.974 | 0.981 | 0.984 | 0.985 | 0.987 | 0.987 |
| 9 | 0.639 | 0.927 | 0.967 | 0.976 | 0.980 | 0.981 | 0.983 | 0.984 |
| 10 | 0.626 | 0.915 | 0.960 | 0.971 | 0.975 | 0.977 | 0.979 | 0.980 |
| 11 | 0.615 | 0.903 | 0.953 | 0.965 | 0.970 | 0.972 | 0.975 | 0.976 |
| 12 | 0.603 | 0.890 | 0.944 | 0.959 | 0.964 | 0.967 | 0.970 | 0.972 |
| 13 | 0.593 | 0.878 | 0.936 | 0.952 | 0.958 | 0.962 | 0.965 | 0.967 |
| 14 | 0.582 | 0.865 | 0.927 | 0.945 | 0.952 | 0.956 | 0.960 | 0.962 |
| 15 | 0.572 | 0.852 | 0.917 | 0.937 | 0.945 | 0.950 | 0.954 | 0.957 |
| 16 | 0.562 | 0.839 | 0.908 | 0.929 | 0.938 | 0.943 | 0.948 | 0.951 |
| 17 | 0.553 | 0.827 | 0.897 | 0.920 | 0.930 | 0.936 | 0.942 | 0.945 |
| 18 | 0.544 | 0.814 | 0.887 | 0.912 | 0.923 | 0.929 | 0.935 | 0.938 |
| 19 | 0.535 | 0.801 | 0.876 | 0.903 | 0.914 | 0.921 | 0.928 | 0.931 |
| 20 | 0.526 | 0.788 | 0.866 | 0.893 | 0.906 | 0.913 | 0.921 | 0.924 |
| 22 | 0.510 | 0.763 | 0.843 | 0.874 | 0.888 | 0.896 | 0.905 | 0.909 |
| 24 | 0.494 | 0.738 | 0.821 | 0.853 | 0.869 | 0.878 | 0.888 | 0.893 |
| 26 | 0.479 | 0.714 | 0.797 | 0.832 | 0.849 | 0.860 | 0.871 | 0.876 |
| 28 | 0.465 | 0.690 | 0.774 | 0.810 | 0.829 | 0.840 | 0.852 | 0.859 |
| 30 | 0.452 | 0.667 | 0.751 | 0.788 | 0.808 | 0.820 | 0.833 | 0.840 |
| 32 | 0.439 | 0.645 | 0.727 | 0.765 | 0.786 | 0.799 | 0.813 | 0.821 |
| 34 | 0.426 | 0.623 | 0.704 | 0.743 | 0.764 | 0.777 | 0.792 | 0.801 |
| 36 | 0.414 | 0.602 | 0.681 | 0.720 | 0.742 | 0.755 | 0.771 | 0.780 |
| 38 | 0.403 | 0.582 | 0.659 | 0.697 | 0.719 | 0.733 | 0.750 | 0.759 |
| 40 | 0.391 | 0.562 | 0.637 | 0.675 | 0.697 | 0.711 | 0.728 | 0.738 |
| 42 | 0.381 | 0.543 | 0.615 | 0.653 | 0.675 | 0.689 | 0.707 | 0.716 |
| 44 | 0.371 | 0.525 | 0.594 | 0.631 | 0.653 | 0.667 | 0.685 | 0.695 |
| 46 | 0.361 | 0.507 | 0.574 | 0.610 | 0.631 | 0.645 | 0.663 | 0.673 |
| 48 | 0.351 | 0.490 | 0.554 | 0.589 | 0.610 | 0.624 | 0.641 | 0.652 |
| 50 | 0.342 | 0.474 | 0.535 | 0.568 | 0.589 | 0.603 | 0.620 | 0.630 |
| 60 | 0.300 | 0.401 | 0.448 | 0.475 | 0.492 | 0.503 | 0.519 | 0.528 |
| 70 | 0.265 | 0.341 | 0.376 | 0.396 | 0.409 | 0.418 | 0.430 | 0.438 |
| 80 | 0.235 | 0.292 | 0.318 | 0.332 | 0.342 | 0.348 | 0.357 | 0.362 |
| 90 | 0.210 | 0.251 | 0.270 | 0.280 | 0.287 | 0.292 | 0.298 | 0.302 |

# TABLE 6 (Concluded)

## HERMANS' ORIENTATION FUNCTIONS

$$f_{(hk,\ell)}$$

Pearson VII Exponent (m)

| FW-HM (°) | 15 | 20 | 30 | 50 | 100 | 200 | 500 | (Gaussian) ∞ |
|---|---|---|---|---|---|---|---|---|
| 2 | 0.999 | 0.999 | 0.999 | 0.999 | 0.999 | 0.999 | 0.999 | 0.999 |
| 3 | 0.998 | 0.998 | 0.998 | 0.998 | 0.998 | 0.999 | 0.999 | 0.999 |
| 4 | 0.997 | 0.997 | 0.997 | 0.997 | 0.997 | 0.997 | 0.997 | 0.997 |
| 5 | 0.995 | 0.996 | 0.996 | 0.996 | 0.996 | 0.996 | 0.996 | 0.996 |
| 6 | 0.993 | 0.994 | 0.994 | 0.994 | 0.994 | 0.994 | 0.994 | 0.994 |
| 7 | 0.991 | 0.991 | 0.991 | 0.992 | 0.992 | 0.992 | 0.992 | 0.992 |
| 8 | 0.988 | 0.989 | 0.989 | 0.989 | 0.989 | 0.989 | 0.989 | 0.990 |
| 9 | 0.985 | 0.986 | 0.986 | 0.986 | 0.987 | 0.987 | 0.987 | 0.987 |
| 10 | 0.982 | 0.982 | 0.983 | 0.983 | 0.983 | 0.984 | 0.984 | 0.984 |
| 11 | 0.978 | 0.979 | 0.979 | 0.980 | 0.980 | 0.980 | 0.980 | 0.980 |
| 12 | 0.974 | 0.974 | 0.975 | 0.976 | 0.976 | 0.976 | 0.977 | 0.977 |
| 13 | 0.979 | 0.970 | 0.971 | 0.972 | 0.972 | 0.972 | 0.972 | 0.973 |
| 14 | 0.964 | 0.965 | 0.966 | 0.967 | 0.968 | 0.968 | 0.968 | 0.968 |
| 15 | 0.959 | 0.965 | 0.966 | 0.967 | 0.968 | 0.968 | 0.968 | 0.968 |
| 16 | 0.954 | 0.955 | 0.956 | 0.957 | 0.958 | 0.958 | 0.959 | 0.959 |
| 17 | 0.948 | 0.950 | 0.951 | 0.952 | 0.953 | 0.953 | 0.953 | 0.954 |
| 18 | 0.942 | 0.944 | 0.945 | 0.946 | 0.947 | 0.948 | 0.948 | 0.948 |
| 19 | 0.936 | 0.937 | 0.939 | 0.941 | 0.942 | 0.942 | 0.942 | 0.942 |
| 20 | 0.929 | 0.931 | 0.933 | 0.934 | 0.935 | 0.936 | 0.936 | 0.936 |
| 22 | 0.915 | 0.917 | 0.920 | 0.921 | 0.922 | 0.923 | 0.923 | 0.924 |
| 24 | 0.900 | 0.902 | 0.905 | 0.907 | 0.909 | 0.909 | 0.910 | 0.910 |
| 26 | 0.883 | 0.887 | 0.890 | 0.892 | 0.894 | 0.894 | 0.895 | 0.895 |
| 28 | 0.866 | 0.870 | 0.873 | 0.876 | 0.878 | 0.879 | 0.879 | 0.880 |
| 30 | 0.849 | 0.853 | 0.856 | 0.859 | 0.861 | 0.862 | 0.863 | 0.863 |
| 32 | 0.830 | 0.834 | 0.838 | 0.842 | 0.844 | 0.845 | 0.846 | 0.846 |
| 34 | 0.811 | 0.815 | 0.820 | 0.823 | 0.826 | 0.827 | 0.828 | 0.828 |
| 36 | 0.791 | 0.796 | 0.801 | 0.804 | 0.807 | 0.808 | 0.809 | 0.810 |
| 38 | 0.771 | 0.776 | 0.781 | 0.785 | 0.788 | 0.789 | 0.790 | 0.791 |
| 40 | 0.750 | 0.756 | 0.761 | 0.765 | 0.768 | 0.770 | 0.771 | 0.771 |
| 42 | 0.729 | 0.735 | 0.741 | 0.745 | 0.748 | 0.750 | 0.751 | 0.751 |
| 44 | 0.708 | 0.714 | 0.720 | 0.724 | 0.728 | 0.729 | 0.730 | 0.731 |
| 46 | 0.686 | 0.693 | 0.699 | 0.704 | 0.707 | 0.709 | 0.710 | 0.710 |
| 48 | 0.665 | 0.671 | 0.678 | 0.683 | 0.686 | 0.688 | 0.689 | 0.690 |
| 50 | 0.644 | 0.650 | 0.656 | 0.661 | 0.665 | 0.667 | 0.668 | 0.669 |
| 60 | 0.540 | 0.546 | 0.552 | 0.557 | 0.561 | 0.563 | 0.564 | 0.565 |
| 70 | 0.448 | 0.453 | 0.458 | 0.462 | 0.465 | 0.467 | 0.468 | 0.468 |
| 80 | 0.370 | 0.374 | 0.378 | 0.381 | 0.383 | 0.384 | 0.385 | 0.386 |
| 90 | 0.307 | 0.310 | 0.312 | 0.315 | 0.316 | 0.317 | 0.318 | 0.318 |
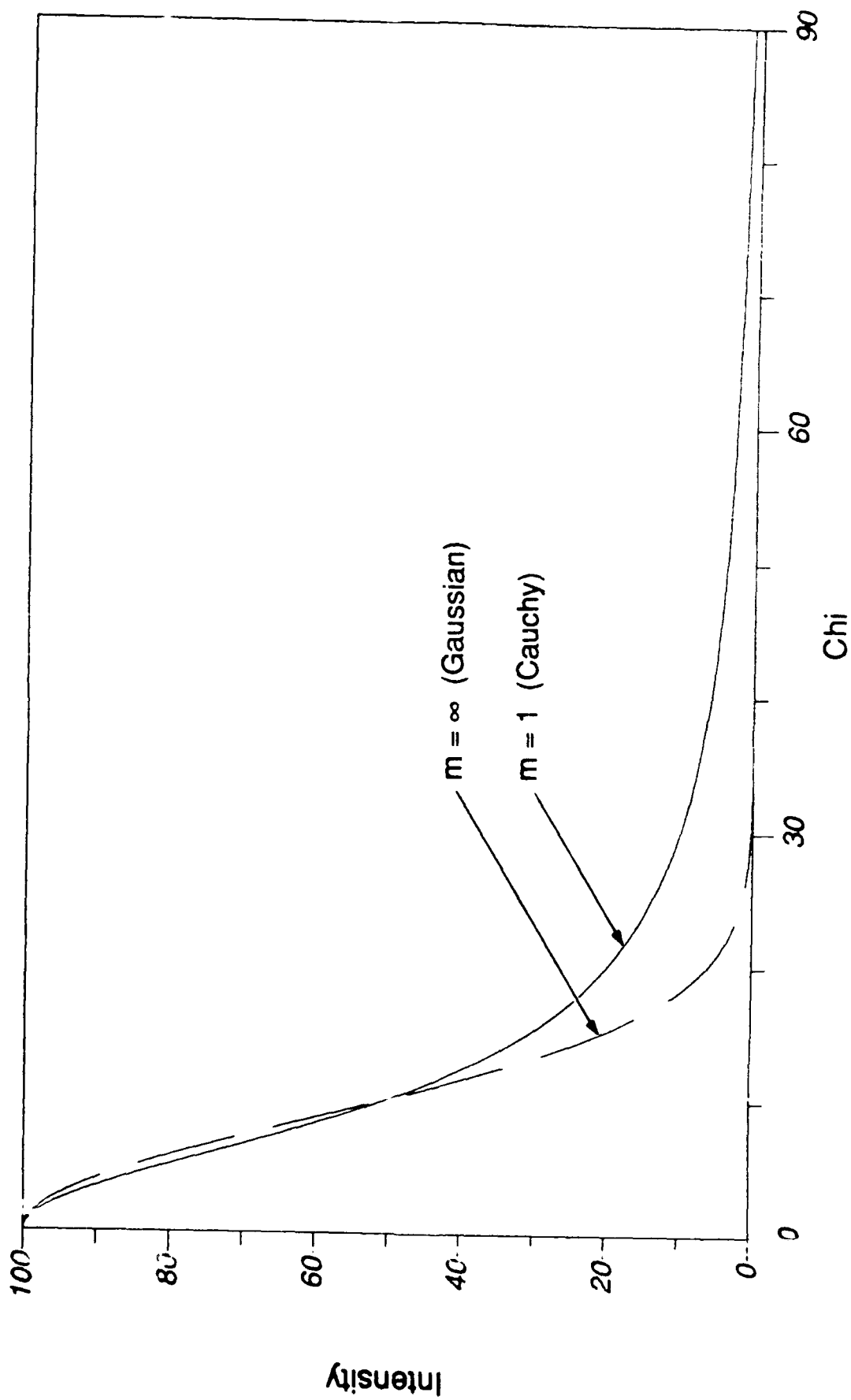
Figure 63. Azimuthal Intensity Profiles for Pearson Exponents.

90
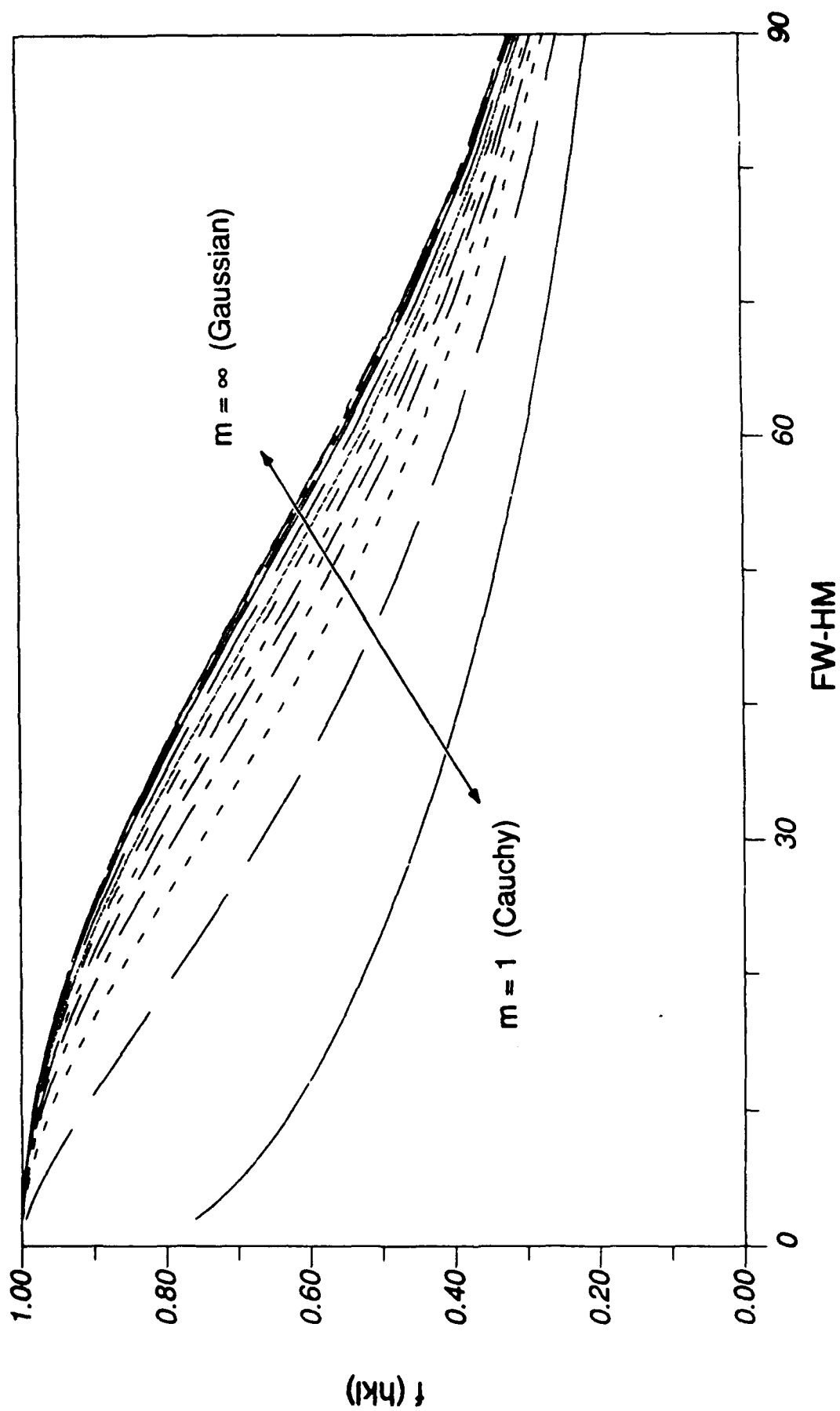
Figure 64. Hermans' Orientation Functions as Function of Azimuthal Full-Width at Half Maximum for a Family of Pearson Exponents.

## TABLE 7

## HERMANS' ORIENTATION FUNCTIONS ESTIMATED FOR SEVERAL FIBERS

### Curve Fit Results

| Fiber | $Z_{(00,2)}$ (°) | Exponent (m) | $f_{(hk,\ell)}$ |
|---|---|---|---|
| *Pitch-Based* | | | |
| P-25 | 31.9 | 5.7 | 0.79 |
| P-55 | 14.1 | 2.4 | 0.89 |
| P-75 | 11.0 | 2.6 | 0.93 |
| P-100 | 5.6 | 2.6 | 0.98 |
| P-120 | 5.6 | 3.6 | 0.99 |
| E-35 | 21.6 | 5.8 | 0.89 |
| E-75 | 10.9 | 3.6 | 0.96 |
| E-105 | 7.2 | 3.8 | 0.98 |
| K-135 | 10.4 | | 0.96 |
| *PAN-Based* | | | |
| T-2 | 35.5 | 7.4 | 0.76 |
| T-300 | 35.1 | 9.3 | 0.79 |
| AS-4 | 36.8 | 9.8 | 0.77 |
| T-40 | 30.2 | 6.9 | 0.83 |
| G40-700 | 29.1 | 6.8 | 0.84 |
| IM6 | 33.7 | 11.9 | 0.81 |
| G45-700 | 26.7 | 5.6 | 0.85 |
| HMS | 19.7 | 3.5 | 0.88 |
| M40J | 21.4 | 3.6 | 0.86 |
| T-50 | 16.4 | 2.7 | 0.88 |
| GY-70 | 9.6 | 2.2 | 0.93 |
| M60J | 9.9 | 3.8 | 0.97 |
| *Rayon-Based* | | | |
| T-75 | 8.7 | 4.6 | 0.98 |

92

Another argument for using $Z_{(00,2)}$ is that it represents the approximate mid-point of the graphene planes misorientation relative to the fiber axis. That is a $Z_{(00,2)}$ of $20^c$ means that the number of crystals misoriented beyond this angular spread ($\pm 10^\circ$ from the fiber axis) is less than one-half the number of crystals oriented perfectly parallel to the fiber axis.

# APPENDIX B.  COMPLETE CALCULATED $L_a$ VALUES FOR CARBON FIBERS

The commercially-available fiber results are listed in the first two tables.  Table 8 has the $L_a$ values calculated using Ruland's method and Equation 14.  Table 9 has the $L_a$ values calculated using the Scherrer equation (Equation 9).

Since the same curves were used to calculate the $L_a$ values for each entry in each of the tables and the formulas are very similar, any and all trends in one table will be essentially the same in the other (although the absolute values will be different).

Table 10 has the $L_a$ values calculated for the commercial fibers which were heat treated using Ruland's method, while Table 11 has the $L_a$ values calculated for these fibers using the Scherrer equation.

The heat-treated vapor grown fiber results are listed in Table 12.  These fibers achieved a high degree of graphitization such that, where (hk,$\ell$) reflections were visible, the dimensions were calculated using the Scherrer equation for both $L_a$ and $L_{hk,\ell}$.  Ruland's method of calculating $L_a$ was used only on the "as grown" and 2200°C heat-treated fibers.

# TABLE 8

## COMPLETE $L_a$ VALUES BASED ON RULAND'S CALCULATIONS FOR THE COMMERCIALLY-AVAILABLE FIBERS

$L_a$ (nm)

| | $\chi=0$ | | $\chi=70$ | | $\chi=90$ | |
|---|---|---|---|---|---|---|
| | (10) | (11) | (10) | (11) | (10) | (11) |
| **Pitch-Based** | | | | | | |
| P-25 | 4.5 | 2.8 | 5.1 | 4.0 | 6.7 | 4.9 |
| P-55 | 11.1 | 12.0 | 12.2 | 16.4 | 31.0 | 28.2 |
| P-75 | 10.1 | 17.4 | 3.5 | 17.3 | 26.5 | 27.8 |
| P-100 | na | 48.8 | na | 56.1 | 85.2 | 74.7 |
| P-120 | na | 64.1 | na | 69.8 | 78.3 | 96.9 |
| | | | | | | |
| E-35 | 4.8 | na | 6.2 | 4.4 | 7.9 | 5.9 |
| E-75 | 13.4 | 14.1 | 8.6 | 9.9 | 23.8 | 19.7 |
| E-105 | 13.0 | 11.4 | na | 14.3 | 34.0 | 30.3 |
| | | | | | | |
| K-135 | 13.8 | 13.4 | na | 12.3 | 27.8 | 24.2 |
| | | | | | | |
| Gr P-55 | 11.7 | 14.9 | | | | |
| Gr P-75 | 9.9 | 20.5 | $\chi$ not meaningful for ground fibers | | | |
| Gr P-100 | na | 44.2 | | | | |
| | | | | | | |
| **PAN-Based** | | | | | | |
| T-2 | na | 2.7 | | | 4.7 | 3.5 |
| T-300 | na | 2.2 | 4.3 | 3.7 | 4.6 | 3.6 |
| AS-4 | 3.7 | 2.3 | 4.8 | 3.5 | 4.4 | 3.6 |
| T-40 | 3.7 | 2.3 | 4.4 | 3.4 | 5.4 | 3.8 |
| | | | | | | |
| G40-700 | 5.5 | 4.3 | 6.4 | 4.9 | 7.5 | 6.2 |
| IM6 | na | 2.5 | | | 5.8 | 5.2 |
| G45-700 | 4.4 | 3.7 | 6.1 | 4.5 | 7.7 | 6.1 |
| IM8 | 3.5 | 2.7 | 5.7 | 4.1 | 5.6 | 4.6 |
| | | | | | | |
| HMS | 6.0 | 5.4 | | | 18.1 | 17.1 |
| M40J | 6.6 | 4.5 | 9.3 | 7.0 | 13.7 | 11.0 |
| T-50 | 7.9 | 4.9 | 9.1 | 8.9 | 17.8 | 16.6 |
| GY-70 | 8.6 | 15.1 | na | 25.2 | 37.3 | 43.0 |
| | | | | | | |
| M60J | 7.8 | 6.4 | na | 13.5 | 29.0 | 28.3 |
| | | | | | | |
| **Rayon-Based** | | | | | | |
| WCA | 6.2 | 4.7 | 7.3 | 6.1 | 7.4 | 6.2 |
| T-75 | 9.9 | 9.4 | na | 17.2 | 37.4 | 35.3 |

na - readable peak was not available from scan

# TABLE 9

## COMPLETE $L_a$ VALUES BASED ON SCHERRER'S CALCULATIONS
## FOR THE COMMERCIALLY-AVAILABLE FIBERS

| | $\chi=0$ | | $\chi=70$ | | $\chi=90$ | |
| | (10) | (11) | (10) | (11) | (10) | (11) |
|---|---|---|---|---|---|---|
| **Pitch-Based** | | | | | | |
| P-25 | 2.2 | 1.4 | 2.5 | 1.9 | 3.2 | 2.3 |
| P-55 | 5.3 | 5.8 | 5.9 | 7.9 | 14.9 | 13.6 |
| P-75 | 4.9 | 8.4 | 3.1 | 8.3 | 12.8 | 13.4 |
| P-100 | na | 23.5 | na | 27.0 | 41.0 | 36.0 |
| P-120 | na | 30.9 | na | 33.6 | 37.7 | 46.7 |
| | | | | | | |
| E-35 | 2.3 | na | 3.0 | 2.1 | 3.8 | 2.8 |
| E-75 | 6.4 | 6.8 | 4.1 | 4.8 | 11.5 | 9.5 |
| E-105 | 6.3 | 5.5 | na | 6.9 | 16.4 | 14.6 |
| | | | | | | |
| K-135 | 6.6 | 6.4 | na | 5.9 | 13.4 | 11.7 |
| | | | | | | |
| Gr P-55 | 5.6 | 7.2 | | | | |
| Gr P-75 | 4.7 | 9.9 | $\chi$ not meaningful for ground fibers | | | |
| Gr P-100 | na | 21.3 | | | | |
| | | | | | | |
| **PAN-Based** | | | | | | |
| T-2 | na | 1.3 | | | 2.3 | 1.7 |
| T-300 | na | 1.1 | 2.1 | 1.8 | 2.2 | 1.8 |
| AS-4 | 1.8 | 1.1 | 2.3 | 1.7 | 2.1 | 1.7 |
| T-40 | 1.8 | 1.1 | 2.1 | 1.6 | 2.6 | 1.8 |
| | | | | | | |
| G40-700 | 2.6 | 2.1 | 3.1 | 2.4 | 3.6 | 3.0 |
| IM6 | na | 1.2 | | | 2.8 | 2.5 |
| G45-700 | 2.1 | 1.8 | 3.0 | 2.2 | 3.7 | 3.0 |
| IM8 | 1.7 | 1.3 | 2.7 | 2.0 | 2.7 | 2.2 |
| | | | | | | |
| HMS | 2.9 | 2.6 | | | 8.7 | 8.3 |
| M40J | 3.2 | 2.2 | 4.5 | 3.4 | 6.6 | 5.3 |
| T-50 | 3.8 | 2.4 | 4.4 | 4.3 | 8.6 | 8.0 |
| GY-70 | 4.2 | 7.3 | na | 12.1 | 18.0 | 20.7 |
| | | | | | | |
| M60J | 3.8 | 3.1 | na | 6.5 | 13.9 | 13.6 |
| | | | | | | |
| **Rayon-Based** | | | | | | |
| WCA | 3.0 | 2.3 | 3.5 | 2.9 | 3.5 | 3.0 |
| T-75 | 4.8 | 4.5 | na | 8.3 | 18.0 | 17.0 |

na - readable peak was not available from scan

96

TABLE 10

## COMPLETE $L_a$ VALUES BASED ON RULAND'S CALCULATIONS
## FOR THE HEAT-TREATED COMMERCIAL FIBERS

| | | $L_a$ (nm) | | | | | |
|---|---|---|---|---|---|---|---|
| | | $\chi=0$ | | $\chi=70$ | | $\chi=90$ | |
| Fiber | Temp. (°C) | (10) | (11) | (10) | (11) | (10) | (11) |
| *P-25* | | | | | | | |
| Previous | | 4.5 | 2.8 | na | na | na | na |
| As Rec'd | | 5.0 | na | 6.0 | 3.9 | 6.6 | 4.9 |
| | 1000 | 5.1 | na | 6.0 | 4.0 | 6.6 | 5.0 |
| | 1500 | 4.6 | na | 6.4 | 4.8 | 6.4 | 7.8 |
| | 2000 | 11.2 | 14.5 | na | 17.5 | 29.9 | 30.0 |
| | 2300 | na | 35.7 | na | 41.9 | 41.8 | 50.1 |
| *P-55* | | | | | | | |
| Previous | | 11.1 | 12.0 | 12.2 | 16.4 | 31.0 | 28.2 |
| As Rec'd | | 10.5 | 8.3 | 9.1 | 9.0 | 21.2 | 18.1 |
| | 1000 | 8.8 | 8.9 | 8.9 | 8.5 | 21.1 | 18.7 |
| | 1500 | 8.5 | 11.7 | 8.3 | 6.5 | 21.2 | 16.6 |
| | 2000 | 10.7 | 12.3 | na | 16.6 | 30.1 | 28.4 |
| | 2300 | 7.3 | 23.3 | na | 32.1 | 40.1 | 46.3 |
| *E-35* | | | | | | | |
| Previous | | 4.8 | na | 6.2 | 4.4 | 7.9 | 5.9 |
| As Rec'd | | 5.8 | na | 6.0 | 4.1 | 7.9 | 6.6 |
| | 1000 | na | na | 6.1 | 4.4 | 7.9 | 6.0 |
| | 1500 | 5.7 | na | 6.3 | 4.4 | 8.8 | 6.8 |
| | 2000 | 14.2 | 16.4 | na | 19.9 | 35.8 | 34.4 |
| | 2300 | na | 36.8 | na | 45.8 | 59.1 | 63.7 |

na - readable peak was not available from scan

## TABLE 11

### COMPLETE $L_a$ VALUES BASED ON SCHERRER'S CALCULATIONS FOR THE HEAT-TREATED COMMERCIAL FIBERS

| | | $L_a$ (nm) | | | | | |
| | | $\chi=0$ | | $\chi=70$ | | $\chi=90$ | |
| Fiber | Temp. (°C) | (10) | (11) | (10) | (11) | (10) | (11) |
|---|---|---|---|---|---|---|---|
| *P-25* | | | | | | | |
| Previous | | 2.2 | 1.4 | na | na | na | na |
| As Rec'd | | 2.4 | na | 2.9 | 1.9 | 3.2 | 2.4 |
| | 1000 | 2.5 | na | 2.9 | 1.9 | 3.2 | 2.4 |
| | 1500 | 2.2 | na | 3.1 | 2.3 | 3.1 | 3.8 |
| | 2000 | 5.4 | 7.0 | na | 8.4 | 14.4 | 14.5 |
| | 2300 | na | 17.2 | na | 20.2 | 20.2 | 24.1 |
| *P-55* | | | | | | | |
| Previous | | 5.3 | 5.8 | 5.9 | 7.9 | 14.9 | 13.6 |
| As Rec'd | | 5.1 | 4.0 | 4.4 | 4.4 | 10.2 | 8.7 |
| | 1000 | 4.2 | 4.3 | 4.3 | 4.1 | 10.2 | 9.0 |
| | 1500 | 4.1 | 5.7 | 4.0 | 3.1 | 10.2 | 8.0 |
| | 2000 | 5.2 | 5.9 | na | 8.0 | 14.5 | 13.7 |
| | 2300 | 3.5 | 11.2 | na | 15.4 | 19.3 | 22.3 |
| *E-35* | | | | | | | |
| Previous | | 2.3 | na | 3.0 | 2.1 | 3.8 | 2.8 |
| As Rec'd | | 2.8 | na | 2.9 | 2.0 | 3.8 | 3.2 |
| | 1000 | na | na | 3.0 | 2.1 | 3.8 | 2.9 |
| | 1500 | 2.8 | na | 3.0 | 2.1 | 4.2 | 3.3 |
| | 2000 | 6.8 | 7.9 | na | 9.6 | 17.2 | 16.6 |
| | 2300 | na | 17.7 | na | 22.1 | 28.5 | 30.7 |

na - readable peak was not available from scan

TABLE 12

## SUMMARY OF $L_a$ AND $L_{hk,\ell}$ VALUES FOR HEAT-TREATED VAPOR GROWN CARBON FIBERS

| Heat Treatment Temperature (°C) | $L_a$ (nm) | | | | $L_{hk,\ell}$ (nm) | | | |
|---|---|---|---|---|---|---|---|---|
| | Meridional | | Off-Axis | | Meridional | | Off-Axis | |
| | $(10,0)^a$ | $(11,0)^b$ | $(10,0)$ | $(11,0)$ | $(10,1)$ | $(11,2)$ | $(10,1)$ | $(11,2)$ |
| As Grown P | 5.1 | 4.5 | 4.8 | 3.4 | | | | |
| 2200 | 23.7 | 26.9 | 15.3 | 23.7 | | | | |
| 2500 | 33.9 | 30.5 | 20.0 | 30.5 | 4.1 | 6.8 | 4.1 | 6.4 |
| 2700 | 30.3 | 43.1 | 28.4 | 41.4 | 11.7 | 11.2 | 12.0 | 11.2 |
| 2800 | 38.1 | 45.7 | 38.0 | 42.9 | 14.9 | 15.0 | 14.0 | 14.5 |
| 2900 | 39.9 | 42.6 | 39.0 | 43.9 | 15.7 | 20.5 | 19.7 | 20.5 |
| 2800 (10 min) | 32.6 | 36.2 | 30.2 | 37.3 | 14.9 | 14.8 | 13.5 | 13.8 |

a - (10) for the as-grown and 2200°C heat-treated fibers.
b - (11) for the as-grown and 2200°C heat-treated fibers.